

**Liquid Xenon Scintillation Detector
for the New $\mu \rightarrow e\gamma$ Search Experiment**

PH. D. THESIS

Kenji Ozone

March 2005

Department of Physics,
Faculty of Science, University of Tokyo

Abstract

A liquid xenon scintillation detector was constructed as a prototype γ -ray detector for the MEG experiment, which will start in 2006 at PSI, Switzerland. The prototype has an active volume of 68.8 liter viewed by 228 PMTs immersed in liquid xenon to detect γ -rays with precision. The detector performance strongly depends on the purity of liquid xenon. The purification system to remove contaminations in liquid xenon was established to enable the large-sized liquid xenon detector with a long absorption length over 1 m (90% C.L.). In 2003 a beam test with laser Compton scattering γ rays up to 40 MeV was performed at AIST. In this test we evaluated the performance of the prototype detector and verified the performance expected for the 1000-liter liquid xenon scintillation detector in the MEG experiment. The energy resolution of 5.2% (FWHM) and the position resolution of 9.9 mm–11 mm (FWHM) are expected for 52.8 MeV γ -rays. It allows a sensitivity to reach two order below the current upper limit of $\text{Br}(\mu \rightarrow e\gamma)$.

Acknowledgments

First, I would like to express my great appreciation to my adviser Prof. Toshinori Mori, the spokesperson of the MEG experiment, for providing me with this work. I am glad to have learned many things from his insights and deep knowledge of physics and his enthusiasm for physics experiment. Without his generous help and support this thesis could not be completed.

I would like to express my gratitude to Dr. Satoshi Mihara for his continuous encouragement. I have learned a lot of things from his prominent talent and insight since I joined the MEG experiment.

I would like to thank Dr. Wataru Ootani for his suitable advice and generous support. I am glad to feel his great store of knowledge on physics, it stimulated me greatly.

I would like to especially thank Prof. Tadayoshi Doke and Prof. Satoshi Suzuki for their useful suggestions and information on liquid xenon.

I gratefully acknowledge Prof. Akihiro Maki, Prof. Tomiyoshi Haruyama, and Katsuyu Kasami for supporting us, especially, when we stayed at KEK to perform the purification test.

I would like to acknowledge Prof. Satoru Yamashita for his continuous encouragement and useful advice.

I would like to thank MEG collaborator, especially Dr. Giovanni Signorelli and Dr. Donato Nicolò for great help all over the prototype R&D, Stefan Ritt for quickly establishing the data acquisition system and support us in every respect, and Yu. Yuri, A. A. Grebenuk and D. N. Grigoriev for helping the installation of the prototype detector at the early stage of the R&D.

I greatly appreciate Dr. Toshiyuki Iwamoto, Dr. Shuei Yamada, Dr. Toshio Nanba, Hajime Nishiguchi, Ryu Sawada, Yasuko Hisamatsu, Atsuhiko Yamaguchi, Toshiya Mitsuhashi, and Takefumi Yoshimura for many discussions and joyful research life. I sincerely admire their attitude and enthusiasm for MEG experiment. I am glad to have studied with them in my graduate school life.

I would like to express sincere gratitude to Hiroyuki Toyokawa, Dr. Hideaki Oogaki for supporting us all over the beam test at TERAS. Without their generous help and support, we could not successfully complete the beam test of the LXe detector.

I wish to express my sincere thanks to Prof. Sachio Komamiya for his encouragement and Prof. Tetsuro Mashimo for useful advice on MC simulation.

I would like to thank the member of ICEPP, University of Tokyo, especially Hajime Nanjo for discussing many things at midnight.

Thanks to the people who are now working in another place, Dr. Yasuchika Yamamoto and Dr. Daisuke Toya for joyful research life.

Special thanks go to the people who performed small prototype tests at Waseda university together, Dr. Kazuhiro Terasawa, Toshiyuki Miyazawa, Sunao Takenaka, Dr. Jun Yashima, Dr. Masaki Yamashita, Go Tejima. I never forget those days at Ookubo.

Finally, I would like to thank my parents, Masataka and Chieko Ozone for their understanding, help, and encouragement on my research.

Contents

Introduction	1
1 Physics in $\mu \rightarrow e\gamma$ Decay Search Experiment	3
1.1 Lepton Flavor Violation	3
1.2 Supersymmetric Grand Unified Theory	3
1.3 Connection with Neutrino Oscillations	5
1.4 $\mu \rightarrow e\gamma$ Decay Search Experiments	7
2 MEG Detector	10
2.1 Liquid Xenon Scintillation Detector	10
2.2 Beam and Target	14
2.2.1 Beam	15
2.2.2 Target	16
2.3 The COBRA Positron Spectrometer	18
2.3.1 Concept of the Spectrometer	18
2.3.2 Thin-wall Superconducting Magnet	20
2.3.3 Chamber System	24
2.3.4 Timing Counter	25
3 Liquid Xenon Scintillation Detector	28
3.1 Liquid Xenon Scintillator	28
3.1.1 Why Liquid Xenon?	28
3.1.2 Properties of Xenon	29
3.1.3 Scintillation of LXe	31
3.2 Strategy of Development of LXe Detector	33
3.3 100-liter Prototype of LXe Scintillation Detector	35
3.4 Photomultiplier	38
3.5 Cryogenics	40
3.5.1 Operation	42
3.6 Monte Carlo Simulation	44
4 Purification and Absorption Length	45
4.1 Optical Properties of LXe	45
4.2 Xenon Purification	47
4.3 Absorption Length Estimate	47

5	Performance of the 100-liter Prototype	53
5.1	Motivation	53
5.2	Laser Compton Scattering beam test at AIST	54
5.3	Trigger and Data Acquisition	58
5.4	PMT Calibration	61
5.4.1	Gain Adjustment	61
5.4.2	QE Measurement	64
5.4.3	Long-term Stability	67
5.4.4	Noise Estimate	67
5.5	Incident Beam	68
5.6	Position Resolution	70
5.6.1	Position Reconstruction in Simulation	70
5.6.2	Depth Reconstruction in Simulation	73
5.6.3	Position Reconstruction	74
5.6.4	Depth Dependence	74
5.6.5	Energy Dependence	79
5.6.6	Difference between the Data and the Simulation	81
5.6.7	Intrinsic Position Resolution	81
5.6.8	Systematic Error	82
5.6.9	Position Resolution	83
5.7	Energy Resolution	83
5.7.1	Compton Edge	83
5.7.2	Fitting Function	84
5.7.3	Fitting Procedure	85
5.7.4	Depth Dependence	86
5.7.5	Energy Dependence	90
5.7.6	Intrinsic Resolution	90
5.7.7	Systematic Error	91
5.7.8	Energy Resolution	93
5.7.9	Energy linearity	95
6	Expected Performance	96
6.1	Expected Resolution	96
6.1.1	Effect of Absorption Length	96
6.1.2	Energy Resolution	98
6.1.3	Position Resolution	101
6.1.4	Timing Resolution	101
6.1.5	Efficiency	101
6.2	Backgrounds and Sensitivity	102
6.2.1	Prompt Background	103
6.2.2	Accidental Background	103
6.2.3	90% C.L. Sensitivity	107
6.3	Decay Angular Measurement	107
6.4	Prospects for Further Improvements of Performance	109
6.4.1	New PMT	109
6.4.2	Waveform Analysis	110
6.5	Calibration Method	112

<i>CONTENTS</i>	iii
7 Conclusion	114
A 10-liter prototype of Liquid Xenon Scintillation Detector	115

List of Figures

1.1	Diagrams of $\mu^+ \rightarrow e^+\gamma$ in SU(5) SUSY models.	4
1.2	Predictions of $\mu^+ \rightarrow e^+\gamma$ branching ratio in SU(5) SUSY models.	4
1.3	Possible solutions for solar neutrino oscillations in the $\tan^2\theta$ vs Δm^2 parameter space after the recent SNO measurements.	6
1.4	$\mu \rightarrow e\gamma$ branching ratios as a function of the mass of the right-handed gauge singlet ν_{R_2} for the different (LMA and LOW) solutions allowed by the solar neutrino experiments.	6
2.1	Schematic view of the MEG detector.	11
2.2	Principles of the MEG detector.	12
2.3	A schematic view of the liquid xenon scintillation detector for the MEG experiment.	13
2.4	PSI accelerator facility and ring cyclotron.	14
2.5	Schematic of the MEG beam line layout up to the injection into the COBRA spectrometer magnet.	16
2.6	Schematic view of the COBRA positron spectrometer.	18
2.7	Problems with an uniform solenoidal magnetic field and advantages of a graded magnetic field.	19
2.8	Rate of Michel positrons per cm^2 per second.	20
2.9	Design view of the coil and cryostat of the COBRA magnet.	21
2.10	Contour plot of the magnetic field produced by the COBRA magnet and magnetic field along the magnet axis measured with a coil current of 200 A.	22
2.11	Stray magnetic field measured in the photon detector region in the excitation test.	23
2.12	Cross-sectional view of a part of a chamber sector. It consists of two layers of drift cells staggered by half-cell.	24
2.13	Structure of the cathode vernier strips.	25
2.14	A sector of the drift chamber and an assembly of 16 sectors.	26
2.15	Configuration of the timing counter.	27
2.16	Geometry of the timing counter hodoscope with PMTs.	27
3.1	Xe phase diagram.	30
3.2	Photon cross section of Xe atoms and mean free path in LXe.	32
3.3	Xe and NaI(Tl) pulse form.	33
3.4	Decay curves of scintillation signals from LXe measured for electrons, α particles, and fission fragments.	34
3.5	Schematic view of the 100-liter prototype of the LXe scintillation detector.	36

3.6	Schematic view of the PMT holder and picture of the PMT holder in the 100-liter prototype detector.	37
3.7	Charge multiplication process in the metal channel dynode PMT.	39
3.8	Voltage divider circuit of R6041Q.	39
3.9	Tolerance of R6041Q against magnetic field.	40
3.10	Pulse tube refrigerator for LXe detector.	41
3.11	Control software of the cryogenic system of the 100-liter prototype developed with LabVIEW.	43
3.12	An example of MC simulation for 40-MeV γ ray.	44
4.1	Absorption coefficient and light absorption.	48
4.2	Mass spectrum obtained in the residual gas analysis.	49
4.3	Setup for circulation and purification of xenon.	49
4.4	A number of photoelectrons when the purification had just begun and when the purification was finishing and light yield transition for cosmic-ray muon events.	50
4.5	Light yield transition for α particle events.	51
4.6	Comparison of α data in the LXe to simulation data.	51
5.1	Schematic view of TERAS.	54
5.2	Setup for LCS beam.	56
5.3	Experimental setup in TERAS beam test.	56
5.4	Energy spectra depending on the diameter size of the 2nd collimator.	57
5.5	The clusters for generating trigger.	59
5.6	Data flow diagram in LCS beam test.	60
5.7	ADC spectra and the relation between σ^2 s and the mean channels in gain adjustment.	62
5.8	Gain distribution of 228 PMTs.	63
5.9	The relation between ADC mean and variance for 4 pairs of LEDs.	63
5.10	Short-term and long-term stability.	64
5.11	The spectra for α particle in the experiment and in the simulation.	65
5.12	QE estimated from gas and liquid data.	66
5.13	Long-term stability in α runs over the beam test.	67
5.14	Typical pedestal distribution of 1 channel and the sum of all channels.	68
5.15	Impinging points of γ rays in this test.	69
5.16	Schematic histograms of charge distribution on the front face.	71
5.17	Difference between true and reconstructed positions in simulation.	72
5.18	Difference between the local weighted mean and simple weighted mean.	72
5.19	The relation between $N_f(0.5)$ and local weighted mean in MC simulation.	73
5.20	The relation between $N_f(0.5)$ and the first conversion depth.	73
5.21	Scatter plot of reconstructed and the true first conversion depths and residual distribution after reconstruction.	74
5.22	The relation between the depth parameter N_f and the local weighted mean.	75
5.23	Examples of the fitting result with a 2-dimensional double Gaussian.	75
5.24	Position resolution as a function of $N_f(0.5)$ for $E_C = 10$ MeV, impinged at P0 and P9.	76

5.25	Position resolution as a function of $N_f(0.5)$ for $E_C = 20$ MeV, impinged at P0 and P9.	77
5.26	Position resolution as a function of $N_f(0.5)$ for $E_C = 40$ MeV, impinged at P0 and P9.	78
5.27	The resolution of the local weighted mean in σ as a function of γ -ray energy.	80
5.28	LCS beam spectra in this test.	84
5.29	Pile-up events in high beam current ($E_C=10$ MeV).	84
5.30	Measured energy spectrum for LCS beam.	85
5.31	The relation between χ^2/ndf as a function of the lower limit of the fitting range, and an example of the fitting.	86
5.32	Energy resolution as a function of $N_f(0.5)$ for $E_C = 10$ MeV, impinged at P0 and P9.	87
5.33	Energy resolution as a function of $N_f(0.5)$ for $E_C = 20$ MeV, impinged at P0 and P9.	88
5.34	Energy resolution as a function of $N_f(0.5)$ for $E_C = 40$ MeV, impinged at P0 and P9.	89
5.35	LCS beam spectra with various horizontal electron bunch size in TERAS.	91
5.36	LCS beam spectra for collimator displacement of 0 mm to 4 mm.	92
5.37	The energy resolution σ_u as a function of γ -ray energy.	94
5.38	Incident LCS beam energy vs measured energy in N_{pe} and energy linearity for data.	95
6.1	A reconstructed energy spectrum for 52.8-MeV γ rays by the linear fit.	97
6.2	The expected energy resolutions for 52.8 MeV γ rays as a function of the absorption length.	98
6.3	The energy resolution vs. absorption length in the final detector by MC simulation.	99
6.4	Energy resolution by mask analysis.	100
6.5	Selection efficiency as a function of $N_f(0.5)$	102
6.6	Integrated photon yield per muon decay $f_\gamma(y)$	106
6.7	Integrated pile-up photon yield per muon decay $f_{\gamma\gamma}(y)$	106
6.8	The relation between the muon stop rate and the 90% C.L. sensitivity.	107
6.9	The sensitive region for the decay angular measurement with an assumption of SU(5) SUSY-GUT and $\text{Br}(\mu^+ \rightarrow e^+ \gamma) > 10^{-12}$	109
6.10	Two types of PMTs.	110
6.11	The principle of the operation of the DRS chip.	111
6.12	Typical waveform of PMT signal from about 50-MeV γ rays taken with the prototype of the DRS.	111
6.13	Schematic view of calibration with CEX beam.	113
A.1	Cross-sectional view of 10-liter prototype of LXe scintillation detector and its vessel.	115
A.2	The position resolution with the 10-liter prototype detector.	116
A.3	The energy resolution with 10-liter prototype detector.	117
A.4	The timing resolution with the 10-liter prototype detector. The resolution is expected to be about 50 psec for over 20,000 photoelectrons.	117

List of Tables

1.1	Upper limits of $\text{Br}(\mu \rightarrow e\gamma)$ in the last 30 years.	7
1.2	LFV search experiments in the near future.	9
2.1	Characteristics of the Ring Cyclotron.	15
2.2	Main properties of $\pi E5$	15
2.3	Comparison of material for the target.	17
2.4	Parameters of the COBRA magnet.	22
3.1	Properties of various scintillators.	29
3.2	Main properties of liquid Xe.	29
3.3	Scintillation photon of LXe.	31
3.4	Three versions of LXe scintillation detectors.	33
3.5	The properties of the PMT (R6041Q).	38
3.6	Refrigerator performance.	42
3.7	Heat load in the cryostat of the 100-liter prototype.	42
3.8	Parameters and values in the MC simulation for the 100-liter prototype detector.	44
4.1	Optical properties of LXe.	45
5.1	Ring parameter and laser properties for LCS beam.	55
5.2	Typical overall noise results.	68
5.3	Energy and position of impinging beam in this test.	69
5.4	Position resolution from measured data.	79
5.5	Position resolution from MC simulation.	79
5.6	Deterioration of position resolution by electronics noise.	81
5.7	The effect by fluctuation of LCS beam energy.	82
5.8	Difference of the position resolution by changing parameters in the MC simulation for QE estimate.	83
5.9	Energy resolution measured in LCS beam test.	90
5.10	Energy resolution in MC simulation.	90
5.11	Deterioration of energy resolution by electronics noise.	90
5.12	Difference in position resolution between collimator displacement of 0 mm and one of 3 mm.	92
5.13	Deterioration of the energy resolution by changing parameters in QE estimate.	93
5.14	Combined systematic errors for energy resolution.	93
6.1	Energy resolution by mask analysis.	101

6.2 Expected detector performances. Every values are in FWHM. 103

Introduction

Now that the neutrino oscillation phenomena have been established, any new physics scenario beyond the Standard Model (SM) necessarily involves lepton flavor violation (LFV) also in the charged lepton sector. There is no way to prevent it in principle.

Particularly, TeV supersymmetry, the most expected among various new physics scenarios, predicts large branching ratios for some of the LFV processes that are already constrained by the current experimental limits. These large LFVs may be induced by ultra heavy right-handed neutrinos that cause seesaw mechanism and/or by grand unification of quarks and leptons at the GUT energy scale. Thus an experiment capable to detect these LFV processes should be able to explore new physics at extremely high energies beyond the SM and even beyond the supersymmetric (SUSY) SM.

The most promising LFV process is the rare muon decay $\mu^+ \rightarrow e^+\gamma$. The past experimental searches for this process were limited by accidental background events, where positrons from the standard Michel decays of muons coincide with gamma rays coming from either radiative muon decays or annihilations of positrons. In order to go beyond the limitations of these past experiments, it is essential to devise innovative detectors of higher performance.

A $\mu \rightarrow e\gamma$ event is characterized by the clear 2-body final state where the decay positron and the gamma ray are emitted in opposite directions with energies equal to half the muon mass ($E = M_\mu/2 = 52.8$ MeV). While positrons with the signal energies are abundant from the Michel decays, gamma rays with such high energies are very rare: the gamma ray spectrum falls off rapidly near the signal energy region. If we improve the energy resolution for gamma rays δE_γ , the accidental background rate decreases, at least, as $(\delta E_\gamma)^2$. Thus a gamma ray detector with a very good energy resolution is a key to any new $\mu \rightarrow e\gamma$ experiments.

A novel liquid xenon scintillation detector, which we are presenting in this thesis, was proposed and has been developed to fulfill the requirements of a new $\mu \rightarrow e\gamma$ experiment MEG [1–3] that is planned to start physics runs at Paul Scherrer Institute in 2006 with an initial sensitivity of 10^{-13} . In this thesis, ideas, preparations, various examinations, and performance of this newly devised detector are described in detail.

The structure of this thesis is as follows. The physics motivation of the MEG experiment is described in Chapter 1. In Chapter 2 the detectors of the MEG experiment are summarized. Logistics and technical details of the liquid xenon scintillation detector are given in Chapter 3. The most important issue of this detector, absorption of scintillation light inside the detector, is fully discussed in Chapter 4. Chapter 5 deals with the main subject of this thesis, i.e. evaluation of the performance of the liquid xenon scintillation detector, where a beam test using gamma rays from laser Compton scattering and its re-

sults are presented in detail. After we discuss the evaluated detector performance and the prospects for the MEG experiment in Chapter 6, a brief conclusion is given in Chapter 7.

Chapter 1

Physics in $\mu \rightarrow e\gamma$ Decay Search Experiment

1.1 Lepton Flavor Violation

In the Standard Model, lepton flavor conservation is built in by hand with assumed vanishing neutrino masses. The introduction of neutrino masses and mixing into the Standard Model also predicts immeasurably small lepton flavor violation (LFV). On the other hand, fundamental theories such as Supersymmetry (SUSY) generically predict LFV at a measurable level. Lepton-flavor-violating processes such as $\mu^+ \rightarrow e^+\gamma$ are therefore very clean (i.e. not contaminated by the background of the Standard Model) and at the same time present a promising area to hunt for signals of profound new physics.

Taking the case of the recent ($g_\mu - 2$) results. Despite the improvement of a factor of two in the experimental uncertainty [4] the measured value lies between $1.6\sigma - 2.6\sigma$ Standard Model prediction, depending on the way the theoretical value is computed. We just note here that a real discrepancy between the measured and the Standard Model predicted $(g_\mu - 2)/2 \sim 10^{-9}$ could imply $\mu^+ \rightarrow e^+\gamma$ rates close to 10^{-11} in the framework of supersymmetric theories [5].

In the following two sections we briefly discuss the predicted rates for the $\mu^+ \rightarrow e^+\gamma$ decay in grand unified supersymmetric theories caused by slepton mixing due to radiative corrections and by the inclusion of a see-saw mechanism for the neutrino masses. We observe that these two sources of LFV are independent and always present in all supersymmetric grand unified models.

LFV has recently been examined also in the framework of theories with extra spatial dimensions (see for instance [6]). Rates above 10^{-14} are again expected and the experiment proposed here would therefore be crucial even in testing these new ideas.

1.2 Supersymmetric Grand Unified Theory

LFV processes are especially sensitive to the supersymmetric extensions of the Standard Model, in particular supersymmetric grand unified theories (SUSY-GUT). In SUSY-GUT, finite slepton mixing appears through radiative corrections in the renormalization group evolution from the GUT to the weak energy scale, even if the slepton mass matrix is assumed to be diagonal at the Plank scale [7]. It has been pointed out that the slepton

mixing thus generated can be very large owing to the heavy top-quark mass [8], thereby enhancing $\mu^+ \rightarrow e^+\gamma$ decay through the loop diagrams shown in Fig. 1.1.

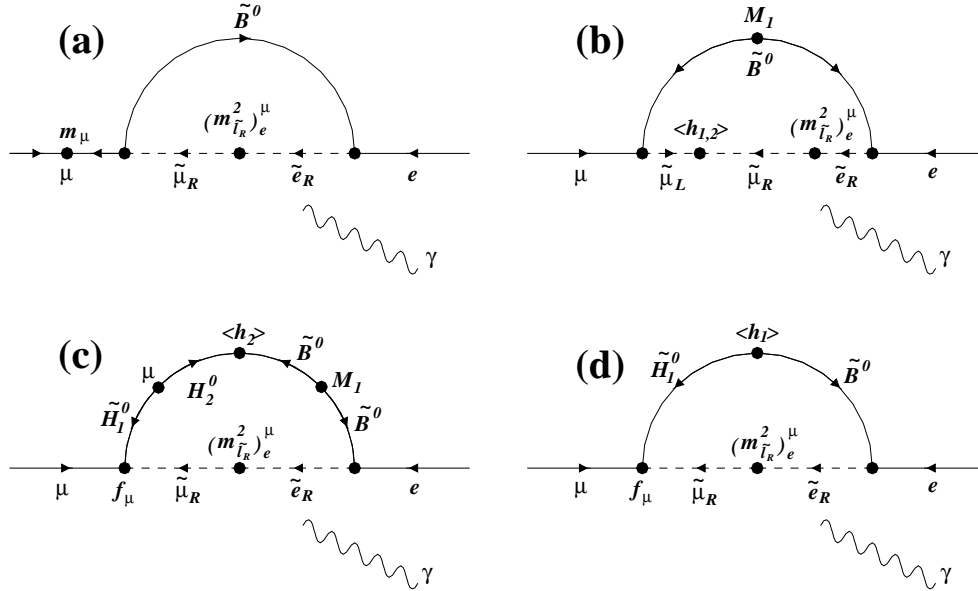


Figure 1.1: Diagrams of $\mu^+ \rightarrow e^+\gamma$ in SU(5) SUSY models.

The predicted branching ratio of $\mu^+ \rightarrow e^+\gamma$ in SUSY SU(5) models [9] is shown in Fig. 1.2. It ranges from 10^{-15} to 10^{-13} for the singlet smuon mass $m_{\tilde{\mu}_R}$ of 100 to 300 GeV.

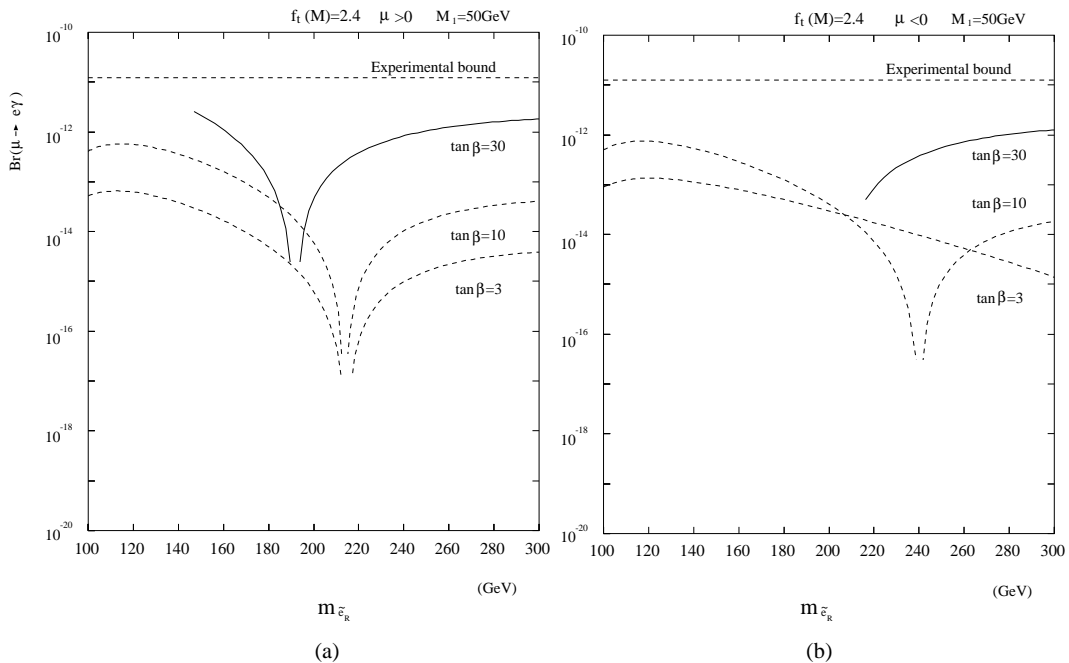


Figure 1.2: Predictions of $\mu^+ \rightarrow e^+\gamma$ branching ratio in SU(5) SUSY models [7].

Recent combined analyses of the four LEP experiments have excluded most of the SUSY parameter space with $\tan\beta < 10$ [10]. The predicted $\mu \rightarrow e\gamma$ rates for higher $\tan\beta$ values should be measurable by the experiment proposed here.

The SO(10) SUSY-GUT models predict an even larger rate than for SU(5) (10^{-13} to 10^{-11}) due to an enhancement factor of $(m_\tau^2/m_\mu^2) \sim 100$ [8], induced by the loop diagrams whose magnitude is proportional to the tau-lepton mass.

1.3 Connection with Neutrino Oscillations

The phenomenon of neutrino oscillations which has been established by experimental observation of atmospheric [11–13] and solar [14–20] neutrinos implies both non-zero neutrino masses and LFV.

In SUSY models, neutrino mixing is expected to enhance the rate of LFV processes such as $\mu^+ \rightarrow e^+\gamma$ [21–23]. A possible contribution to the slepton mixing between $\tilde{\mu}$ and \tilde{e} is from V_{21} (between ν_1 and ν_2), corresponding to the mixing needed to explain the solar neutrino deficit.

The recent SNO solar neutrino observations [15], when combined with all the previous measurements, confine the mixing parameters to two allowed regions, namely the MSW large mixing angle solution (LMA) and the MSW large angle–low Δm^2 (LOW) solution, as shown in Fig. 1.3. The plot in Fig. 1.4 shows the predictions for $\mu^+ \rightarrow e^+\gamma$ decay corresponding to the two solutions as a function of the mass of the right-handed gauge singlet ν_{R2} . The vacuum solution is also shown for completeness though it is excluded by the SNO analysis. The width of the predicted bands is associated with the possible $\tan\beta$ parameter values. We observe again (see the previous section) that the lowest $\tan\beta$ values, corresponding to lower $\mu \rightarrow e\gamma$ rates, are highly disfavored by the recent analyses of the LEP data [10].

In conclusion, the $\mu^+ \rightarrow e^+\gamma$ branching ratio, when combined with Δm^2 and mixing angle measurements by solar neutrino experiments, will determine or severely constrain the mass scale of the right-handed gauge singlet, postulated to exist at ultra high energies ($10^{12} - 10^{15}$ GeV).

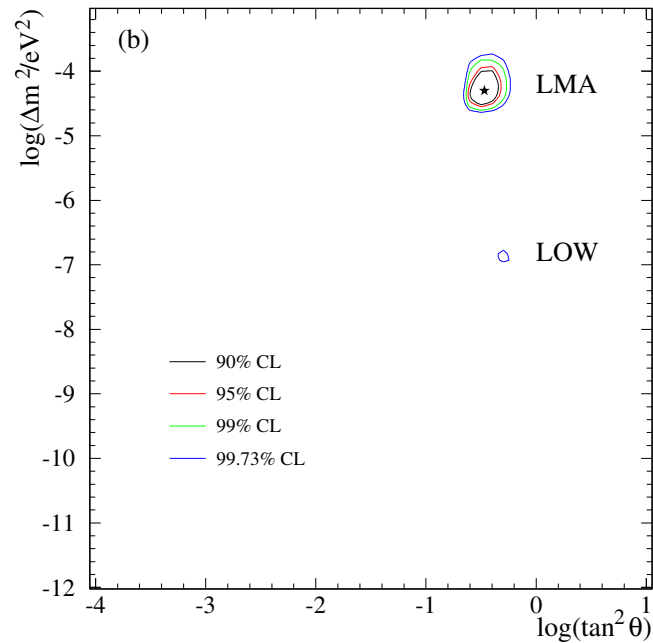


Figure 1.3: Possible solutions for solar neutrino oscillations in the $\tan^2 \theta$ vs Δm^2 parameter space after the recent SNO [15] measurements.

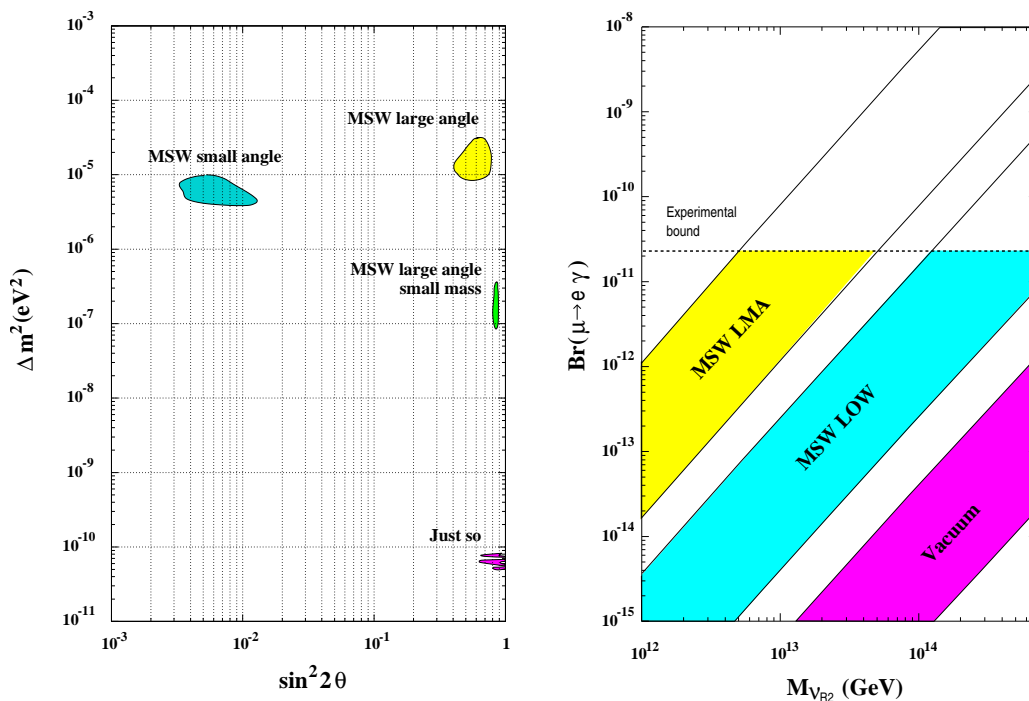


Figure 1.4: $\mu \rightarrow e\gamma$ branching ratios as a function of the mass of the right-handed gauge singlet ν_{R2} for the different (LMA and LOW) solutions allowed by the solar neutrino experiments. The vacuum solution case is shown for completeness though excluded by the SNO experiment (from ref. [23]).

1.4 $\mu \rightarrow e\gamma$ Decay Search Experiments

A history of $\mu \rightarrow e\gamma$ search experiments and their obtained upper limits of the $\mu \rightarrow e\gamma$ branching ratio are listed in Table 1.1

Year	Experiment	Site	Upper Limit	Reference
1977	–	SIN (presently PSI)	1.0×10^{-9}	[24, 25]
1977	TRIUMF	–	3.6×10^{-9}	[26]
1979	–	LANL	1.7×10^{-10}	[27, 28]
1986	Crystal Box	LANL	4.9×10^{-11}	[29]
1999	MEGA	LANL	1.2×10^{-11}	[30]

Table 1.1: Upper limits of $\text{Br}(\mu \rightarrow e\gamma)$ in the last 30 years.

A $\mu \rightarrow e\gamma$ event is characterized by the clear 2-body final state. The decay electron and the gamma ray are emitted in opposite directions with the same energy equal to half the muon mass. To utilize this simple kinematics in the search, muons are stopped in a material (a stopping target). Positive muons are used to avoid capture by the target nuclei.

So-called “surface muons” are abundantly produced by bombarding primary protons into a thick production target. The surface muons come from the decays of pions that stop near the surface of the production target and have a sharp momentum spectrum around 29 MeV/c. Because of this narrow momentum spread, they are easily stopped by a thin target ($\approx 100 \mu\text{m}$). This is important for achieving good resolutions in measuring positrons and reducing background of annihilation gamma rays. With the naturally 100% spin polarized surface muons, angular distribution of $\mu \rightarrow e\gamma$ can be measured after the discovery. This measurement could eventually pin down the right GUT model.

The major background in a $\mu \rightarrow e\gamma$ search is accidental coincidence of a positron, coming from standard Michel decays, and a gamma ray, coming from radiative muon decays or annihilation of positrons. Since the accidental background increases quadratically as the muon rate, a continuous, DC muon beam, that has the lowest instantaneous rate, is best suited for a $\mu \rightarrow e\gamma$ search, rather than a pulsed beam. To achieve a sensitivity of 10^{-14} with a detection efficiency $\epsilon \approx 10\%$ within one year’s time $T \approx 10^7$ sec, a muon rate of $10^{14}/\epsilon/T = 10^{14}/0.1/10^7 \approx 10^8/\text{sec}$ is necessary.

Requirements on detectors, particularly gamma ray detectors, are very severe. They must have very good resolutions in energy, position and time, both for positrons and gamma rays, to distinguish $\mu \rightarrow e\gamma$ from the accidental background. In short, very good detectors are most demanding in a $\mu \rightarrow e\gamma$ search.

Another LFV process, a so-called $\mu^- \rightarrow e^-$ conversion ($\mu\text{N} \rightarrow e\text{N}$), has a similar physics sensitivity as $\mu \rightarrow e\gamma$ in terms of possible experimental reach for generic SUSY LFV vertices.

In a $\mu^- \rightarrow e^-$ conversion a muon converts into an electron by exchanging a virtual photon (or something more exotic) with the capture nucleus. The electron has a monochromatic energy of $E_{\mu \rightarrow e} = M_\mu - \delta$, where M_μ is the muon mass and δ is a sum of the binding energy of the muonic atom and the nuclear recoil energy. So the experimental signature is simple: a single monochromatic electron with $E_{\mu \rightarrow e}$ (105.1 MeV for Al target). Negative muons must be used to form muonic atoms with the target nuclei.

For generic photonic LFV vertices, physics sensitivity of $\mu \rightarrow e$ conversion is two orders of magnitude lower than $\mu \rightarrow e\gamma$: $(\mu \rightarrow e \text{ conversion})/(\mu \rightarrow e\gamma) = 1/390$ for Al target, $1/249$ for Ti, and $1/340$ for Pb in terms of branching ratios. Thus, a $\mu \rightarrow e\gamma$ branching ratio of 1×10^{-14} corresponds to 3×10^{-17} for $\mu \rightarrow e$ conversion. To achieve this sensitivity, a negative muon beam of an intensity of $10^{10} - 10^{11}$ /sec is necessary.

Getting such a high muon rate is a big issue. Because there is no “surface muon beam” for negative muons, such a high intensity beam tends to have a much broader spectrum and is usually contaminated by various other particles, particularly pions.

Major backgrounds in a $\mu \rightarrow e$ conversion search are (a) electrons from muon decays in orbit and (b) beam-related background.

The energy E_e of the “decay in orbit” electron has a spectrum falling off rapidly as $(E_{\mu \rightarrow e} - E_e)^5$. By improving the electron energy resolution σ_{E_e} , this background decreases as $\sigma_{E_e}^5$. Since the energy resolution is dominated by energy loss in the stopping target, a thinner target is required. However, stopping efficiently a broad spectrum of muons in a thin target is quite difficult.

There are various beam-related background caused by beam contaminants such as pions. For example, pions may be radiatively captured by the target nuclei, emitting gamma rays which subsequently convert into electrons. Thus, in short, a very good muon beam is most demanding in a $\mu \rightarrow e$ conversion search.

The MECO (Muon Electron CONversion) experiment [31], the first of the planned $\mu^- \rightarrow e^-$ experiments, was proposed to search for $\mu \rightarrow e$ conversion at a sensitivity below 10^{-16} . For $\mu \rightarrow e$ conversion events occurring at 1×10^{-16} , 5 signal events may be detected with 0.5 background events in one year running according to their proposal. It was scientifically approved in 1997 by Brookhaven National Laboratory and its construction was recently approved for the fiscal year of 2005. It will take at least 5 years for construction.

The use of a graded-field solenoid to collect pions leads to a 1000 fold increase in muon intensity (to 10^{11} /sec) over the previous experiment. This idea was originally proposed for a Russian experiment [32].

A 30 nsec pulsed proton beam is extracted every 1.35 μ sec during a 0.5 sec beam spill from the Alternating Gradient Synchrotron (AGS). To avoid beam-related background, the MECO experiment only operates 0.6 μ sec after the beam pulse, when all the backgrounds have fallen off.

To stop a broad spectrum of muons, 17 layers of 0.2 mm thick Al targets are used. Aluminum is chosen as target material, because its muon capture lifetime (0.9 μ sec) matches the measurement cycle while heavier elements have much shorter lifetimes.

PRISM (Phase-Rotated Intense Slow Muons) [33] is an ambitious project to produce high intensity muon beam with narrow energy spread and less contamination, proposed to be built at the J-Parc 50 GeV proton ring, currently under construction at Tokai, Japan. A Fixed-Field Alternating Gradient synchrotron (FFAG) is used to carry out “phase rotation,” i.e. a conversion of an original short pulse beam with wide momentum spread ($\pm 30\%$) into a long pulse beam with narrow momentum spread ($\pm 3\%$) by strong RF field. After 5 turns in the FFAG ring for the phase rotation, pions in the beam all decay out. Given 10^{14} protons /sec from the J-Parc ring, the PRISM facility should be able to provide $10^{11} - 10^{12}$ muons/sec.

There are still several R&D items to study: for example, low energy pion production and capture system, and injection/extraction of muons into/from the FFAG ring. A real-size FFAG ring, which may be used for PRISM later, is being constructed at Osaka

University for R&D studies.

PRIME (PRISM Mu E) [33] is a proposed experiment to search for $\mu \rightarrow e$ conversion at the future PRISM facility. Because of a very low duty factor of the PRISM beam, the experiment has to handle an extremely high instantaneous rate of 10^{10} - 10^{11} muons per beam bunch. In the PRIME experiment a curved solenoid spectrometer is used to transport only electrons with desired momenta from the stopping target to the detector. Thanks to PRISM's good quality muon beam, with a higher efficiency and a better momentum resolution, a sensitivity of the level of 10^{-18} may be expected according to their Letter of Intent, although a detailed design of the experiment still does not exist.

Table 1.2 summarizes these coming LFV experiments.

Experiment	MEG	MECO	PRISM/PRIME
Site (Country)	PSI (Switzerland)	BNL (U.S.A.)	J-Parc (Japan)
Search for	$\mu \rightarrow e\gamma$	$\mu N \rightarrow eN$	$\mu N \rightarrow eN$
Sensitivity in BR	$10^{-13} - 10^{-14}$	3×10^{-17}	10^{-18}
Beam Intensity (μ/s)	up to 1×10^8	10^{11}	$10^{11} \sim 10^{12}$
Start in/at	2006	>2010	unknown (LoI only)

Table 1.2: LFV search experiments in the near future. Note that physics sensitivity of a $\mu N \rightarrow eN$ experiment with the same sensitivity in branching ratio is 1/300 - 1/400 worse than a $\mu \rightarrow e\gamma$ experiment.

Chapter 2

MEG Detector

A schematic view of the MEG detector is shown in Fig. 2.1. The MEG detector consists of two characteristic detector components: a liquid xenon (LXe) scintillation detector and a COBRA positron spectrometer.

Principles of the MEG detector are illustrated in Fig. 2.2. A positive muon beam with an intensity of 10^8 /sec extracted from the $\pi E5$ beam channel at the PSI is brought to stop in a thin target placed at the center of the superconducting magnet. The γ -rays from the target traverse the thin superconducting magnet of the COBRA spectrometer and are detected by the LXe scintillation detector. The momentum and the emission angle of the positrons from the target are precisely measured by the drift chamber system placed inside the superconducting magnet and the timing of the positrons are also measured by the timing counters.

In this chapter we will give a brief description of each detector component.

2.1 Liquid Xenon Scintillation Detector

Xenon has been widely used as a detector material in different fields. It can be used as either scintillation detector or ionization detector. Xenon scintillator has high light yield (75% of NaI(Tl)) and fast signals as shown in Table 3.3 and Fig. 3.3. These properties enable very precise energy and time measurements of γ -rays. Scintillation signal from liquid xenon has a short tail which serves to minimize pile-up of accidental γ -rays under high-rate background. The properties of xenon are described in detail in Sec. 3.1.

The design of the γ -ray detector in MEG experiment is shown in Fig. 2.3. We use only scintillation photons from the LXe and do not attempt to collect ionizations. This makes the design of the detector quite simple. Scintillation photons from the LXe are collected by ~ 800 photomultiplier tubes (PMTs) from all sides which are immersed in 800-liter LXe.

All the PMTs will be read with high-precision waveform digitizers with a sampling speed of 2.5 GHz or higher. The precise measurements of the total charge and the arrival time of each pulse result in accurate determination of the energy and the timing of the γ -ray. Furthermore, the waveform analysis allows us to avoid pile-up of accidental γ -rays which is quite important in searching for rare event under high-rate background. The output distribution over the 800 PMTs also provide us detailed information on the interaction positions of the γ -rays and the pile-up of accidental γ -rays.

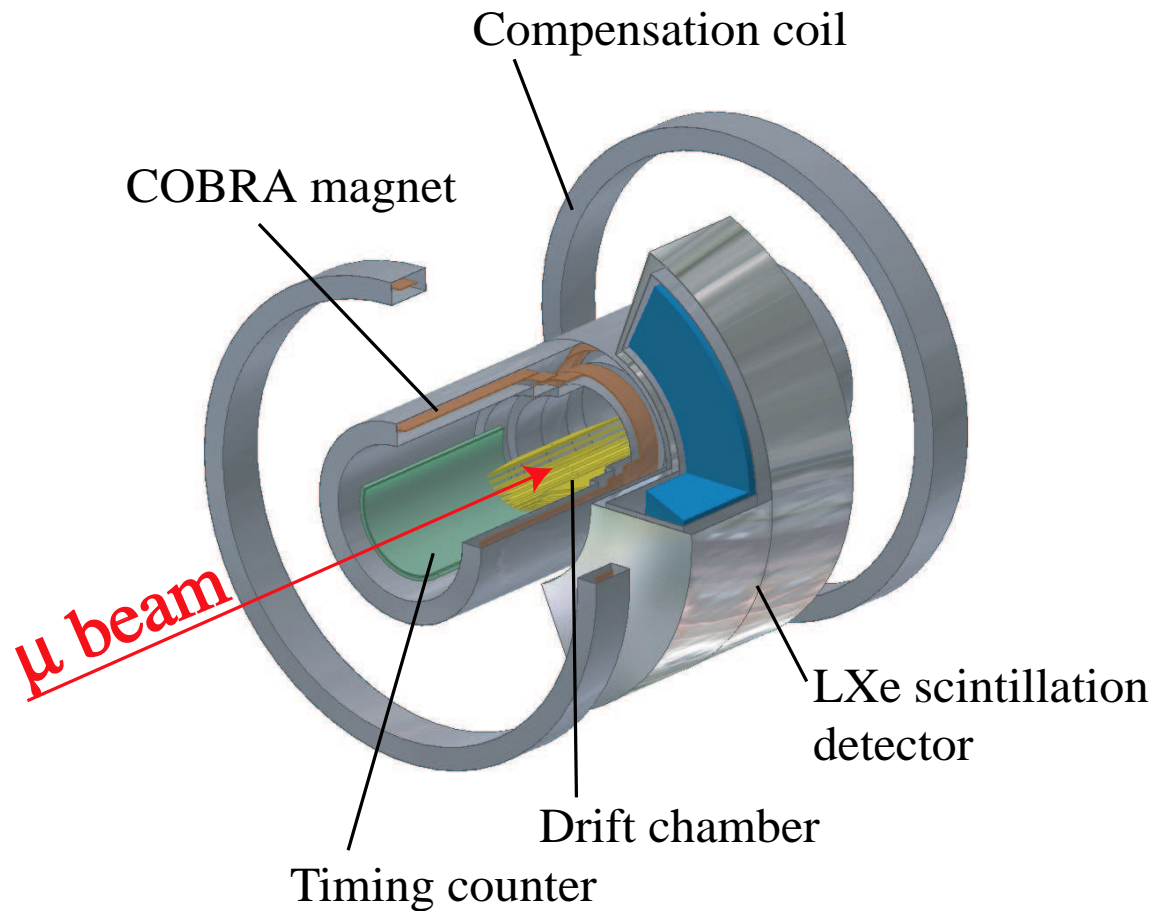


Figure 2.1: Schematic view of the MEG detector.

The design goal of the LXe detector to enable search for $\mu \rightarrow e\gamma$ with a sensitivity of $\text{Br} \sim 10^{-13}$ is the following:

- Time resolution: $\Delta t = 100$ psec (FWHM).
- Position resolution: $\Delta x = \Delta y = 2$ mm, $\Delta r = 7$ mm (FWHM).
- Energy resolution: $\Delta E = 1.4\%$ (FWHM).
- No deterioration even under high rate background.

This design is quite challenging because LXe scintillation detector with this scale has never been built before as far as we know. We therefore built two smaller prototypes before starting the construction of the full-scale detector to gain experiences in detector operation and to prove the excellent performance of this novel detector.

The first prototype was a 10-liter LXe detector. After some feasibility study with the 10-liter prototype we built the second prototype with 100-liter LXe in order to verify the performance of the final detector with more realistic conditions. In this thesis, we will mainly discuss the expected performance of the final detector on the basis of the results from the various tests carried out with the 100-liter prototype. The details will be described in later chapters.

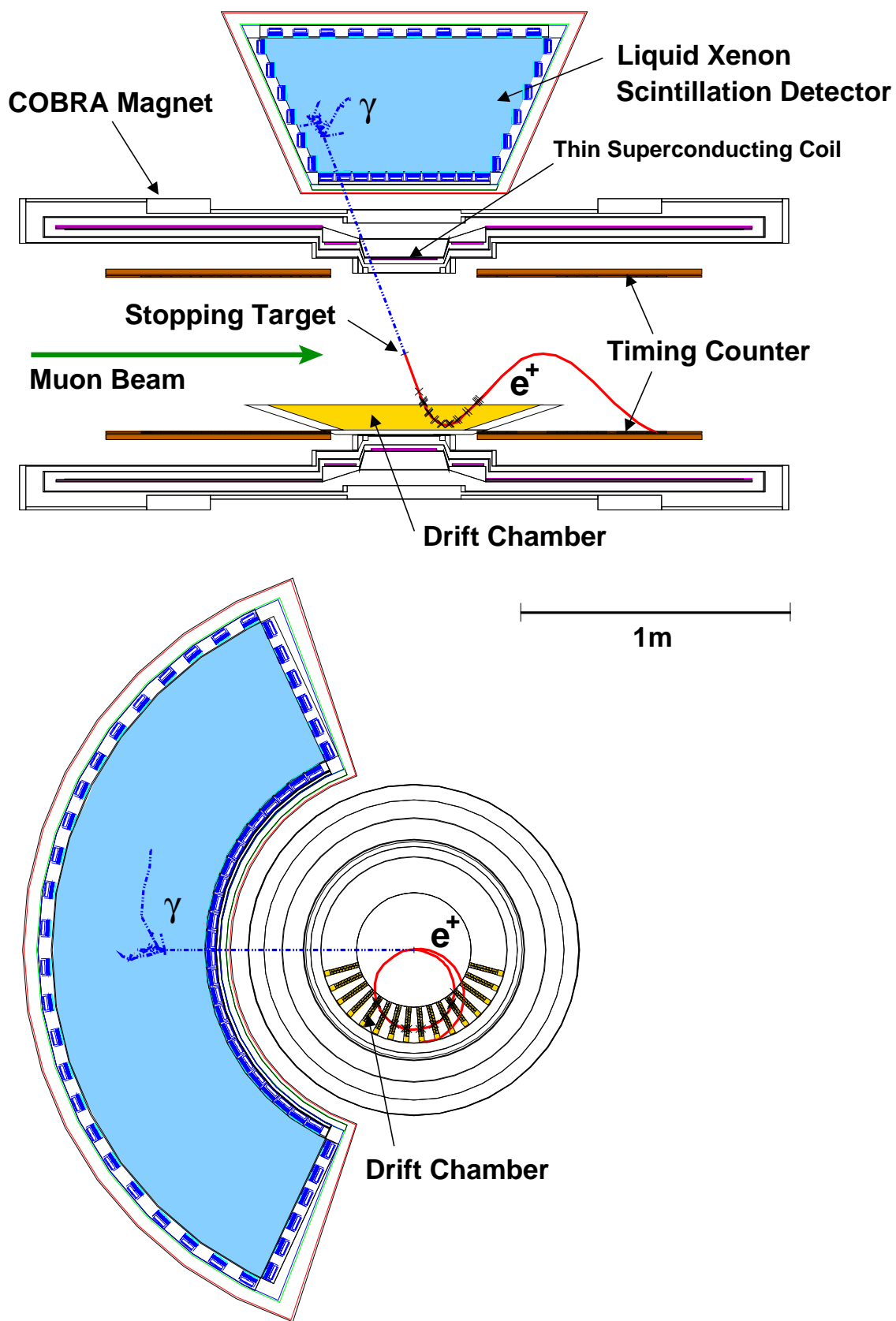


Figure 2.2: Principles of the MEG detector.

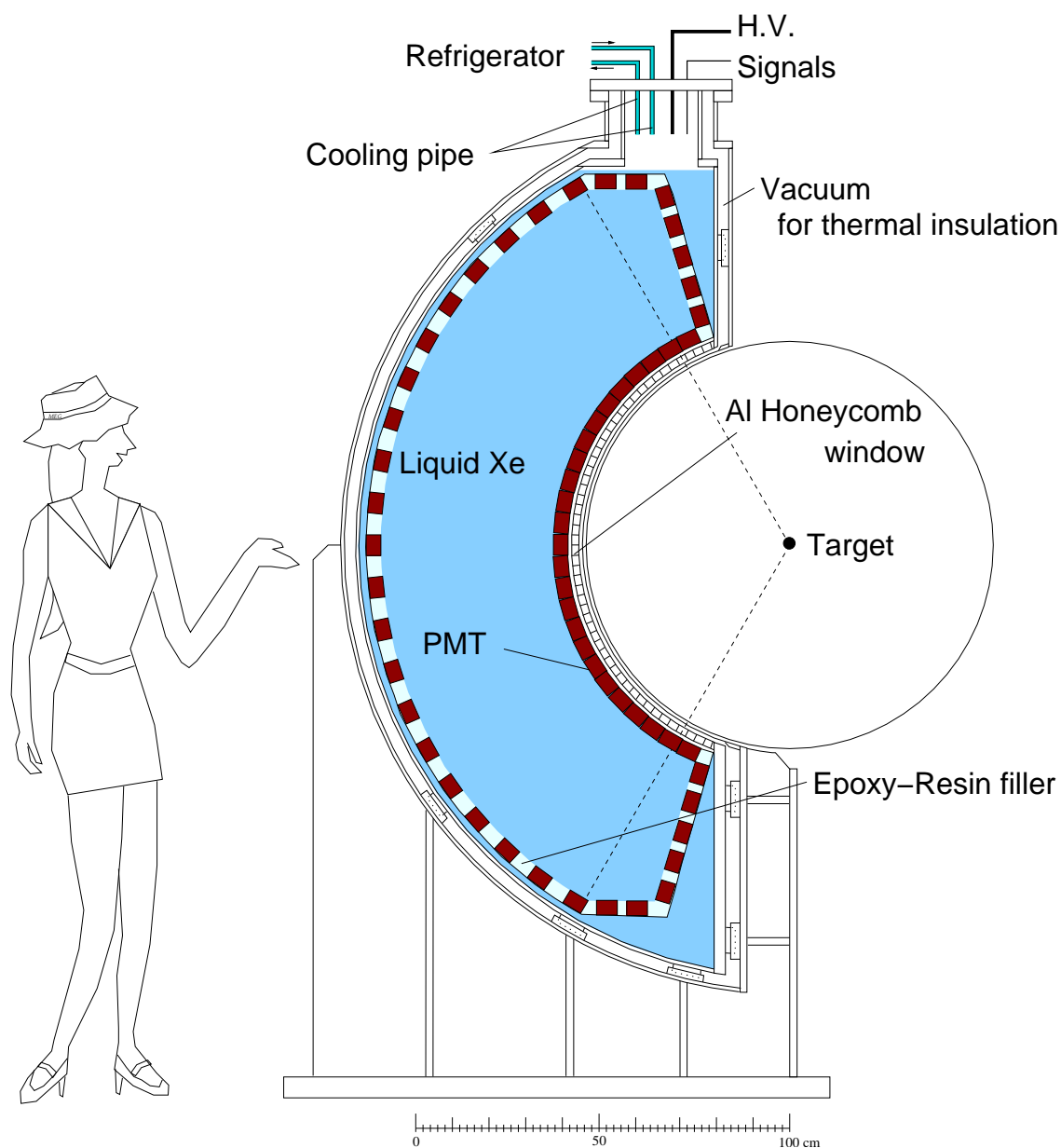


Figure 2.3: A schematic view of the liquid xenon scintillation detector for the MEG experiment.

2.2 Beam and Target

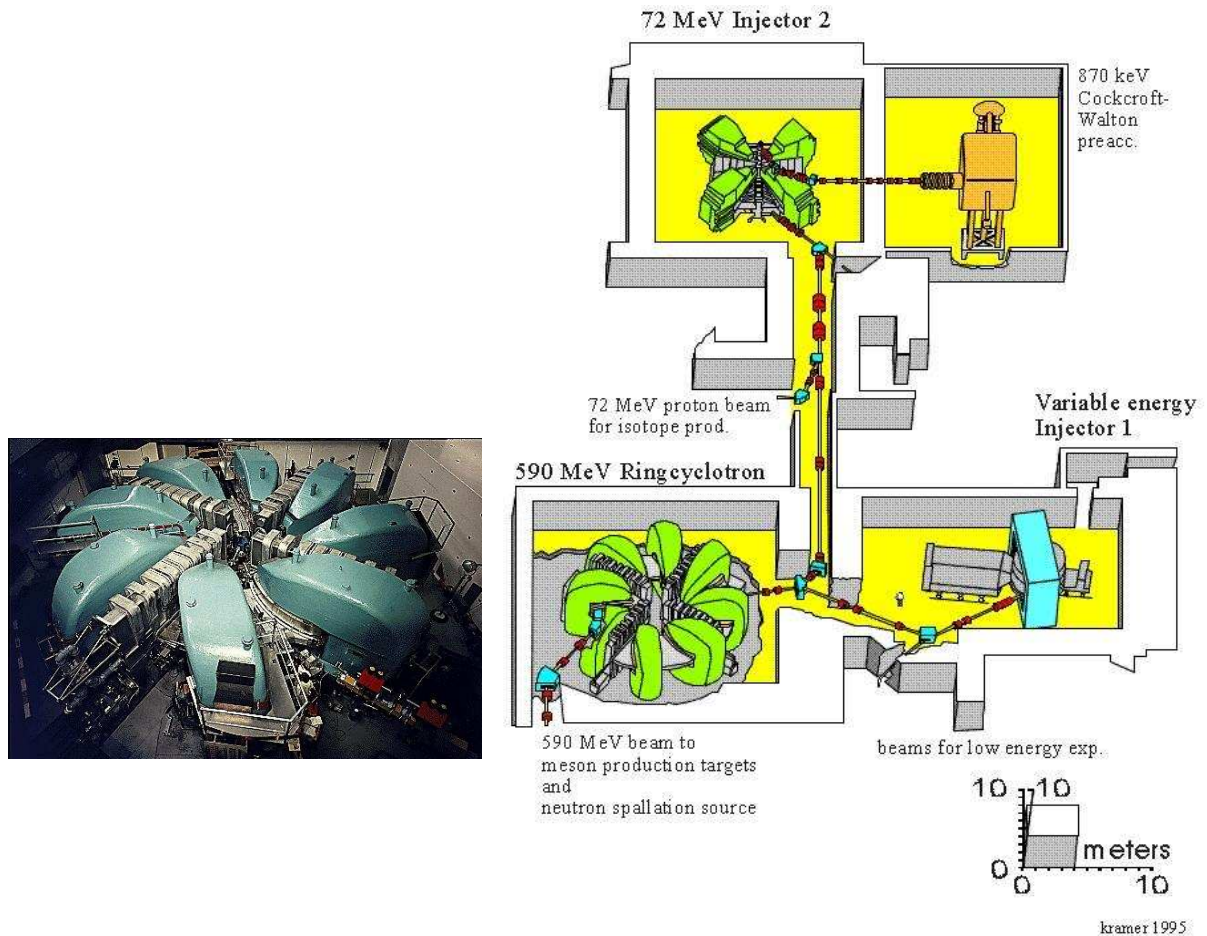


Figure 2.4: PSI accelerator facility (right) and ring cyclotron (left).

The PSI accelerator facility is one of the most prominent in the world. The facility and the ring cyclotron are shown in Fig. 2.4. This accelerator can create a proton beam of the highest power of the world.

The protons are accelerated to a fixed energy of 590 MeV in the ring cyclotron. Its principal components are eight sector magnets and four accelerator cavities (50.63 MHz frequency) with a peak voltage each of 730 kV.

The 72 MeV beam from either one of two injector cyclotron (Injector 1 or Injector 2) enters from the back of the cyclotron, is injected into an orbit in the center of the ring, accelerated over about 220 revolutions and extracted at the full energy as shown in 2.4. The design is based on criteria that allow operation at very high beam intensities: an open structure of four large and powerful RF-cavities providing a high acceleration voltage, and a flat-top cavity operating at the third harmonic of the accelerating RF-voltage. The resulting strong, phase-independent energy gain per revolution gives good turn separation and hence beam extraction with low beam losses. This is a mandatory condition for high current operation in a cyclotron. The properties of the ring cyclotron is summarized in Table 2.2.

Injection Energy	72 MeV
Extraction Energy	590 MeV
Extraction Momentum	1.2 GeV/c
Energy spread (FWHM)	$\sim 0.2\%$
Beam Emittance	$\sim 2\pi$ mm·mrad
Beam Current	1.6 mA DC
Accelerator Frequency	50.63 MHz
Time Between Pulses	19.75 ns
Bunch Width	~ 0.3 ns
Extraction Losses	~ 0.03

Table 2.1: Characteristics of the Ring Cyclotron.

2.2.1 Beam

The π E5 channel in the PSI facility extracts low-energy pion and muon beams from the thick production target at an angle of 175° with respect to the primary proton beam. The main characteristics of the beam are listed in Table 2.2. For the MEG experiment the beam channel will be tuned to ≈ 28 MeV/c to collect surface muons (muons coming from the decay at rest of pions on the production target surface). Measurements, performed before starting the MEG experiment, indicate that we can expect a beam intensity up to $(8 - 10) \times 10^8 \mu^+/\text{s}$ for the primary proton current of 1.5 mA [34].

solid angle acceptance	150 msr
momentum range	20 – 120 MeV/c
length	10.4 m
momentum band (FWHM)	10%
momentum resolution (FWHM)	2%
horizontal emittance	15.3 cm·rad
vertical emittance	3.6 cm·rad
spot size	4×4 cm ²

Table 2.2: Main properties of π E5.

In order to be able to reach the best sensitivity to the $\mu \rightarrow e\gamma$ decay it is necessary to have a well understood beam transport system delivering a high intensity surface muon beam (up to $1 - 2 \times 10^8 \mu^+/\text{s}$) with a minimum spot-size and a small momentum spread, that must be stopped in a thin target, with a minimum of contaminant particles (positrons) entering the detectors.

For examining these issues extensive studies have been performed at the π E5 channel [35] and the final design of the transport system from the exit of the beam line up to the injection into the COBRA spectrometer magnet has been made recently. This will be comprised of a 'two-stage' arrangement, as shown schematically Fig. 2.5.

There are four main components in the system: (i) The extraction element, Triplet I , a quadrupole triplet which couples to the present 'Z'-branch ¹ of the π E5 channel. (ii)

¹There are two branches in the PSI π E5 channel, called 'U' and 'Z'. The MEG experiment will be

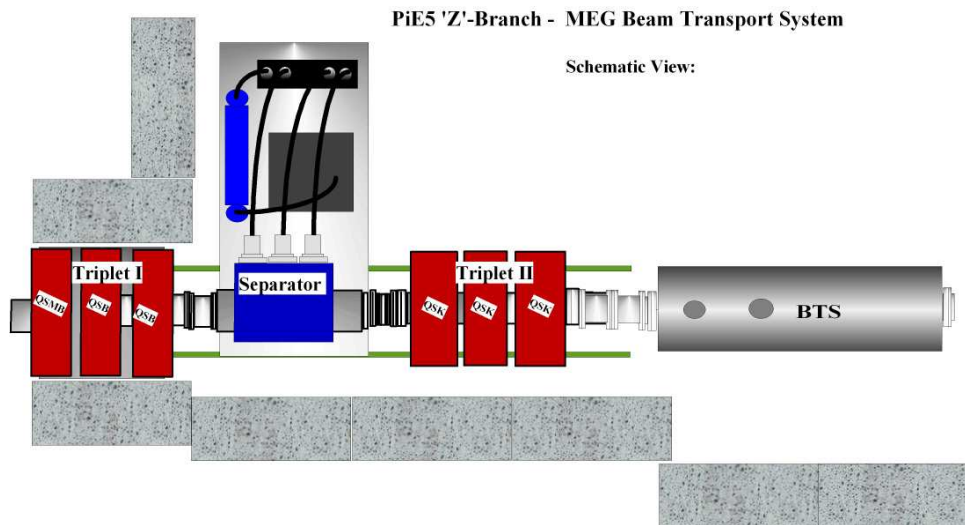


Figure 2.5: Schematic of the MEG beam line layout up to the injection into the COBRA spectrometer magnet.

The WIEN-filter, an (E \wedge B) crossed-field, vertically deflecting separator, necessary for good beam positron suppression. (iii) Triplet II, necessary for good optical focusing at the collimator system placed behind this triplet. (iv) BTS or beam transport solenoid, which is used as a coupling element to the final COBRA spectrometer, as well as housing the momentum degrader/ collimator system.

It has been proved, in these consecutive studies, that a good separation quality between the muons and background positrons can be achieved with a vertical spot-separation of approximately 12 cm, corresponding to a 7.2σ separation and that a stop rate on the target can reach close to $1 \times 10^8 \mu/s$ at a beam current of 1.8mA and a 6cm production target for secondary beam [35].

Setup of the beam line is in progress and will be finished in the year 2005 together with construction of the beam line elements such as the WIEN-filter, BTS, and collimator system.

2.2.2 Target

The target will be placed at a slant angle of 22° (corresponding to a slant ratio of 1 : 2.5) at the center of the COBRA spectrometer magnet. Three kinds of material, Mylar, Polyethylene, and Kapton, have been investigated for the target material from view points of multiple scattering and radiation length. The result is summarized in Table 2.3. Assuming a central beam momentum of 28MeV/c, with a momentum bite of 6.4%, the mean range is calculated to be $\sim 1100\mu m$ for Polyethylene and $\sim 870\mu m$ for both the other material. Supposing that we use a $100\mu m$ Mylar or equivalent thickness Polyethylene/Kapton, necessary thickness for the degrader will be as summarized in Table 2.3. Note that the target will be placed with a slant angle, resulting in total thickness of the target and degrader smaller than the mean range.

performed at the 'Z'-branch.

Material	Density	Radiation Length	Mean Range (28 MeV/c muon)	Target	Degrader
Mylar (C ₅ H ₄ O ₂) _n	1.39 g/cm ³	28.7cm	~870μm	100μm	600μm
Polyethylene (CH ₂) _n	0.95 g/cm ³	47.9cm	~1100μm	150μm	700μm
Kapton (C ₂₂ H ₁₀ N ₂ O ₅) _n	1.42 g/cm ³	28.6cm	~1100μm	150μm	700μm

Table 2.3: Comparison of material for the target.

Thus, overall, it seems that Polyethylene is the best material from both a background suppression (radiation length) and a beam quality (multiple scattering, or material amount) point of view. Design work of the mechanical structure to fix the target, with a "zero-material" target suspension system, is underway. It is quite important to take into account the experience and knowledge obtained by the previous experiments, mainly MEGA and the Crystal Box Collaborations. In addition the use of special calibration targets, like a liquid-hydrogen target for producing π^0 s through the charge exchange process, has been duly noted and will also be taken into account carefully.

2.3 The COBRA Positron Spectrometer

The COBRA (COnstant Bending RAdius) positron spectrometer consists of a magnet specially designed to form a graded magnetic field, a drift chamber system to measure the positron momentum, and scintillation counters to measure the positron timing. Its schematic view with a typical trajectory of a 52.8-MeV positron is shown in Fig. 2.6.

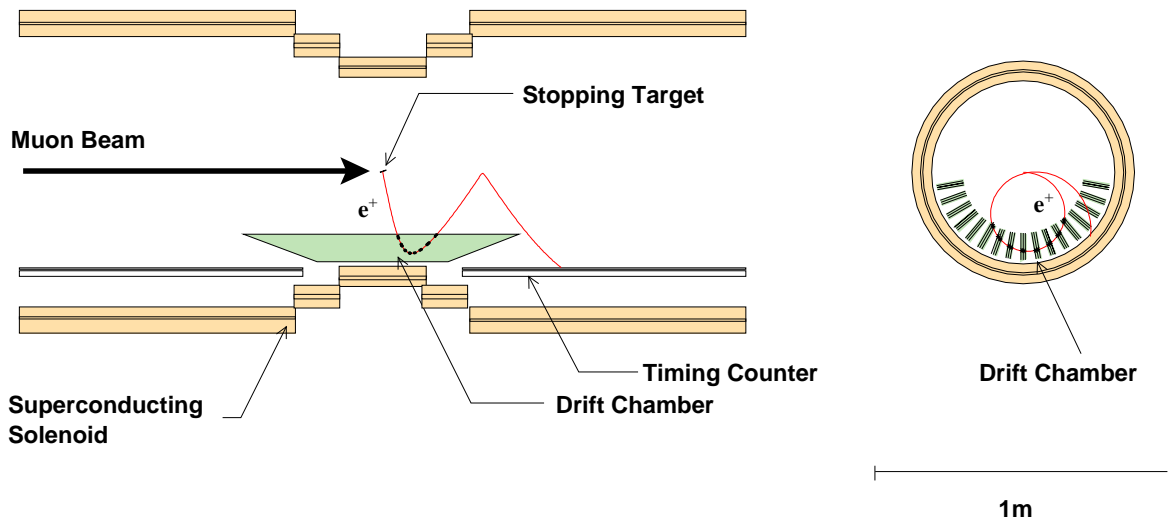


Figure 2.6: Schematic view of the COBRA positron spectrometer.

2.3.1 Concept of the Spectrometer

Most of spectrometers makes use of solenoidal magnetic field to select charged particles' momentum. In case of muon decay it can confine low momentum tracks within a certain radius so that a large fraction of Michel positrons do not reach the track-detectors located at large radii. However, as shown in Fig. 2.7(a), in a simple uniform solenoidal field such as the one adopted in the MEGA experiment, positrons emitted close to 90° make many turns in the tracking chamber, therefore causing problems in pattern recognition or even disturbing a stable operation of the chambers. Also, the bending radius of positrons of a given absolute momentum depends on the production angle, which makes it difficult to select high momentum tracks, as shown in Fig. 2.7(b).

In order to avoid these problems, we have adopted a solenoid with a graded magnetic field, which provides the central field of 1.27 Tesla at $z = 0$ and slowly decreasing field as $|z|$ increases. As shown in Fig. 2.7(c), the positrons emitted close to 90° are swept away by this graded magnetic field much more quickly than in the case of the uniform magnetic field.

The graded magnetic field is arranged such that monochromatic positrons from the target follow trajectories with a constant projected bending radius independent of the emission angle, as shown in Fig. 2.7(d): the bending radius is determined by the absolute momentum and not by its transverse component. This allows us to define the absolute momentum window of positrons to be detected by the drift chamber cells.

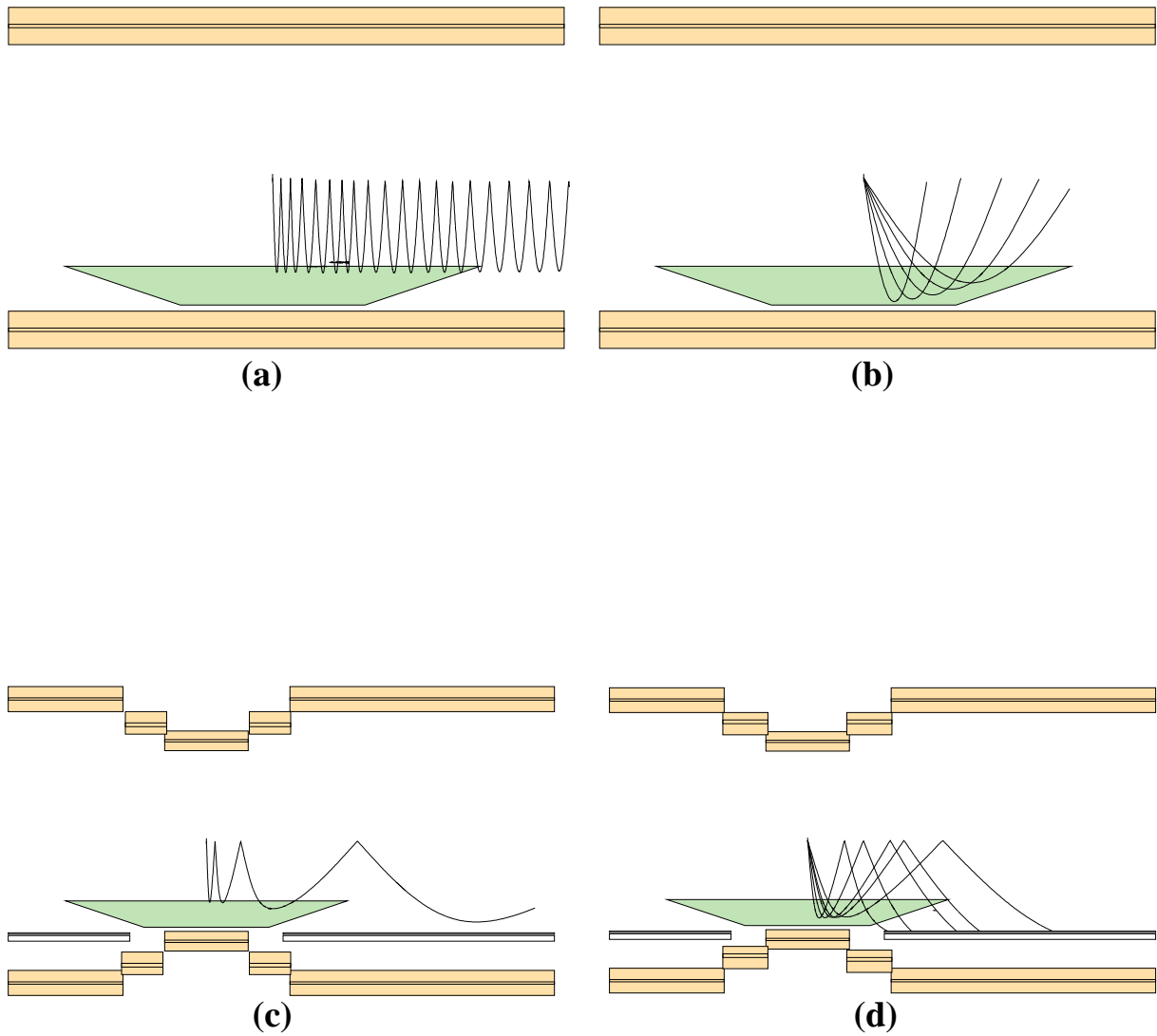


Figure 2.7: Problems with an uniform solenoidal magnetic field and advantages of a graded magnetic field: (a) $r - z$ view of the solenoid shown with the trajectory of a particle emitted at 88° making many turns inside the detector. (b) Trajectories of monochromatic particles emitted at various angles. The bending radius depends on the emission angle. (c) $r - z$ view of the COBRA spectrometer shown with the trajectory of a particle emitted at 88° . The particle is swept away much more quickly than one in (a). (d) Trajectories of monochromatic particles emitted at various angles. The bending radius is independent of the emission angle.

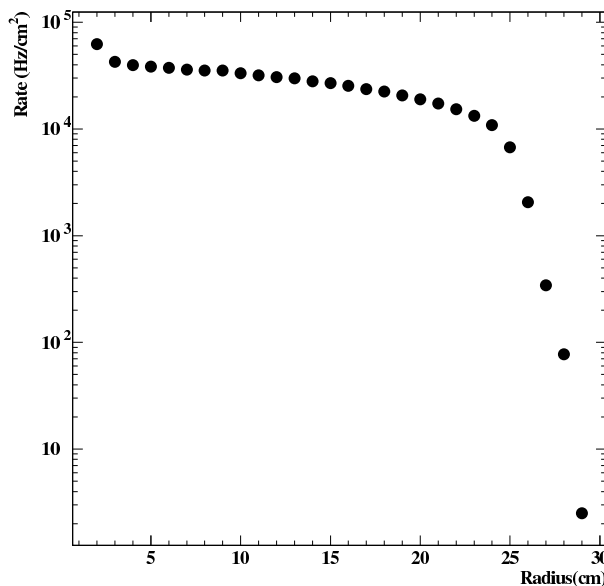


Figure 2.8: Rate of Michel positrons per cm^2 per second as a function of radius assuming a muon decay rate of $1 \times 10^8/\text{s}$.

Fig. 2.8 shows the rate of Michel positrons estimated by Monte Carlo simulation. It is shown in a unit of the rate per cm^2 per second as a function of radius for a muon decay rate of $1 \times 10^8/\text{s}$. By placing the chamber at a radius larger than 20 cm the counting rate can be contained to a level below the limit of stable chamber operation. It is important to remark that the rates at the outermost radii are especially low, which facilitates reduction of the background in the signal region.

2.3.2 Thin-wall Superconducting Magnet

The COBRA magnet consists of a main superconducting magnet and a pair of compensation coils which is adopted to reduce the stray magnetic field around the photon detector. The superconducting magnet consists of five coils with three different radii; one central coil, two gradient coils, and two end coils. A resistive (i.e. non superconducting) cable will be used for the compensation coil. Fig. 2.9 shows the layout of the magnet coils.

The magnet is designed to form a graded magnetic field so as to achieve the good features of the positron spectrometer as explained in the previous section.

The parameters of the COBRA magnet are listed in Table 2.4, whereas Fig. 2.10(a) shows the contour plot of the calculated magnetic field distribution produced by the COBRA magnet. The field intensity along the magnet axis is shown in Fig. 2.10 (b) superimposed with measured values. The performance of the spectrometer and the stray field around the photon detector were optimized by adjusting the diameter, length, and current density of the coils. The five superconducting coils are connected in series and the current density of the coil is controlled by changing the density of the cable winding and operating current, as summarized in Table 2.4. A detailed description of the COBRA magnet can be found in [35–37].

Within the acceptance of the photon detector ($|\theta| \geq 70^\circ$), the thickness of the magnet is reduced to $0.197X_0$ so that the photons from the target, placed at the center of the mag-

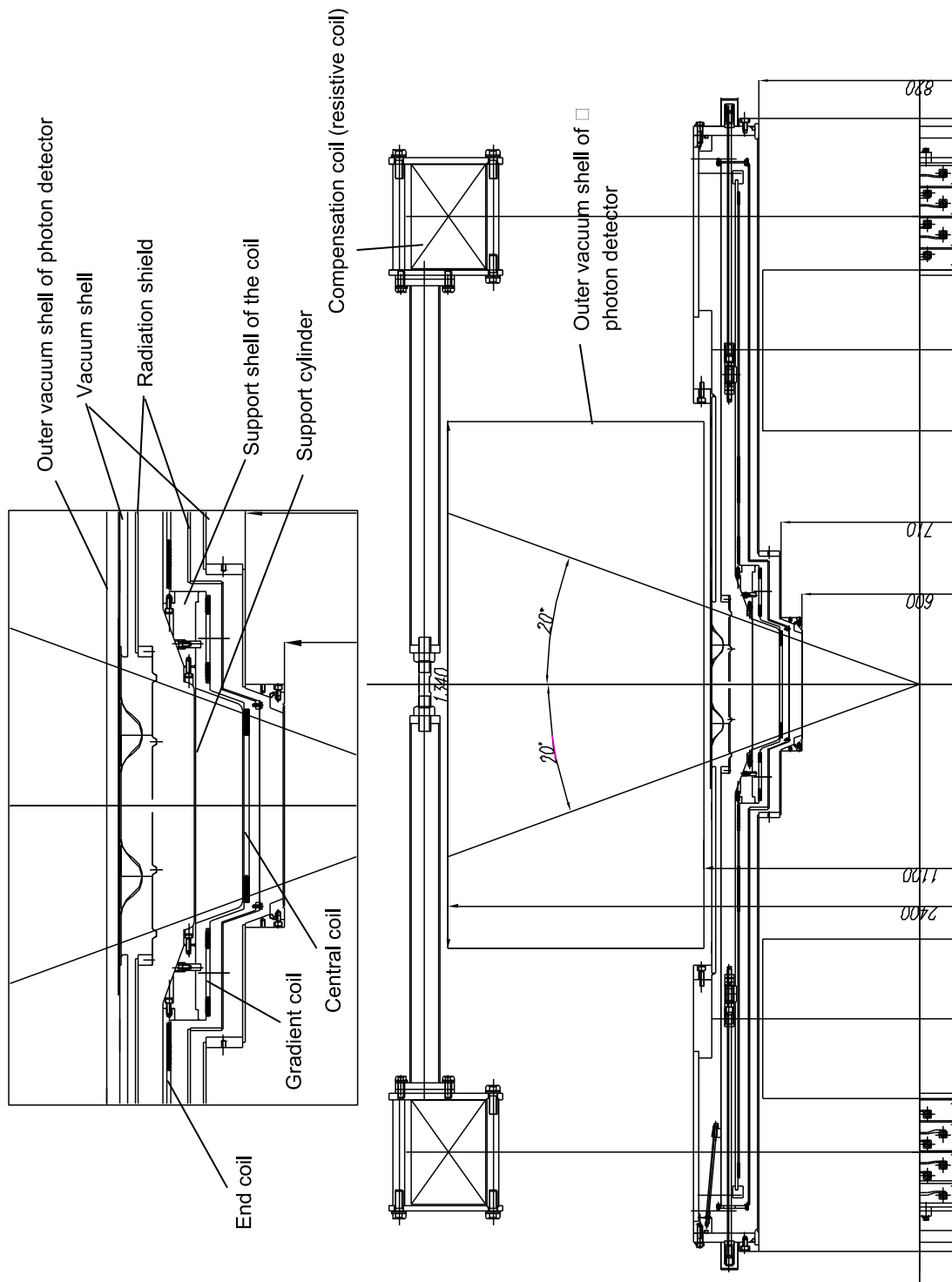


Figure 2.9: Design view of the coil and cryostat of the COBRA magnet.

net, can traverse. In order to achieve this thickness a high-strength aluminum-stabilized conductor was specially developed [38, 39].

The stray field produced by the superconducting coils, has to be reduced to a level of 50 Gauss in the vicinity of the photon detector as will be described in later sections. This is necessary since the photomultiplier tubes used in the photon detector would suffer

Table 2.4: Parameters of the COBRA magnet.

Coil	Central	Gradient	Inner end	Outer end	Compensation
Conductivity	Super	Super	Super	Super	Resistive
Inner dia. (mm)	699.1	809.1	919.1	919.1	2210
Outer dia. (mm)	711.6	820.6	929.5	929.5	2590
Length (mm)	240.3	110.4	189.9	749.2	265
z of coil center (mm)	0	± 235	± 405.4	± 874.95	± 1190
Layers	4	4	3	3	14
Turns per layer	267	123 (1st) 92(2nd-4th)	80	624 (1st-2nd) 92(3rd)	20
Turns (total)	1068	399	240	1548	280
Winding density (Turns/m)	4444.4	3614.1	1263.8	2066.2	1056.6
Winding	e-w	e-w(1st) f-w(2nd-4th)	f-w	f-w	double pancake
Inductance(H)	1.64	0.62	0.35	2.29	0.54
Current (A)	360	360	360	360	360
Energy E (kJ)	106	40	23	148	35
Weight M (kg)	9	4	7	28	1620
E/M (kJ/kg)	11.8	10.0	3.3	5.3	0.02

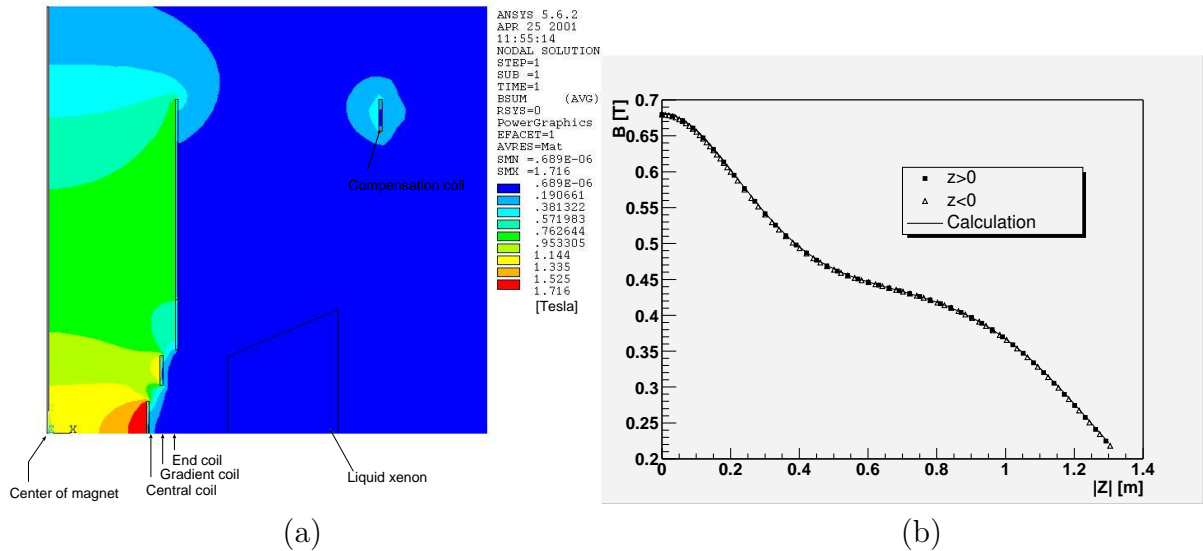


Figure 2.10: (a) Contour plot of the magnetic field produced by the COBRA magnet; (b) Magnetic field along the magnet axis measured with a coil current of 200 A.

from gain variations as the applied magnetic field strength was changed. This would lead to a performance degradation of the calorimeter and will be avoided by the use of

the compensation coils. Fig. 2.11 shows a distribution of stray magnetic field around the photon detector measured during excitation tests. The measurement was done at 50% operating current and the field strength shown in the figure is normalized to the full operating current. It can be seen that the field strength in the photon detector region is compensated as designed and well below requirement.

Excitation tests were carried out several times on site. Quench propagation was measured by inducing a quench via several methods as described in [35], enabling us to confirm safe operation of the magnet.

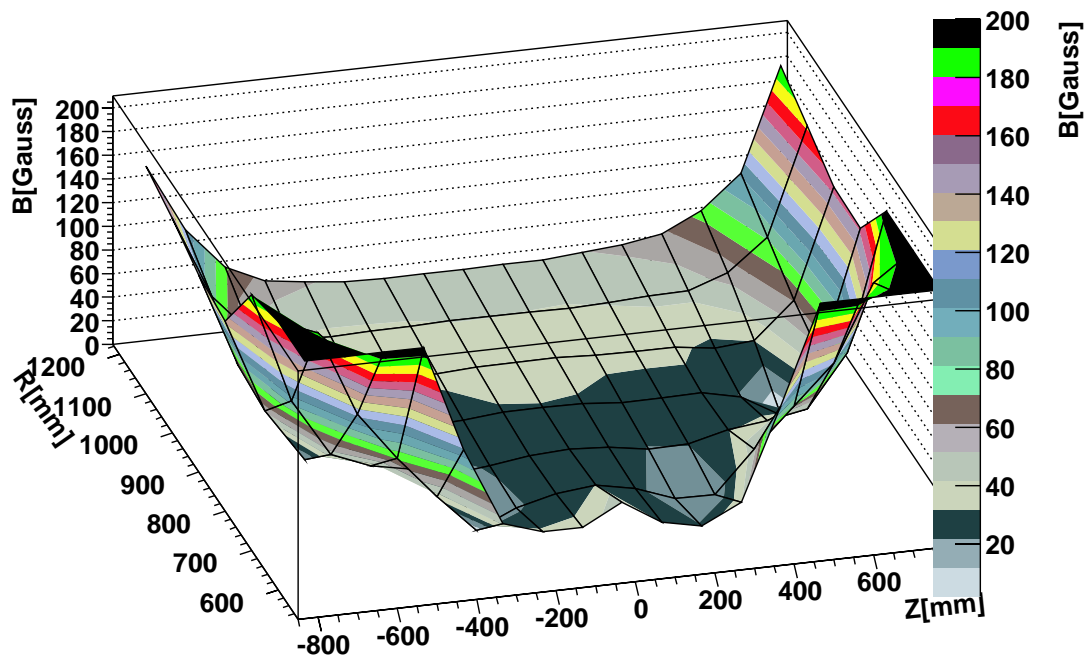


Figure 2.11: Stray magnetic field measured in the photon detector region in the excitation test. The measurement was done at 50% operating current. The field strength shown in this figure is normalized to the full operating current.

2.3.3 Chamber System

Positron tracks are measured with 16 drift chamber sectors aligned radially at 10° intervals in azimuthal angle. Each sector consists of two staggered arrays of drift cells, as shown in Fig. 2.12.

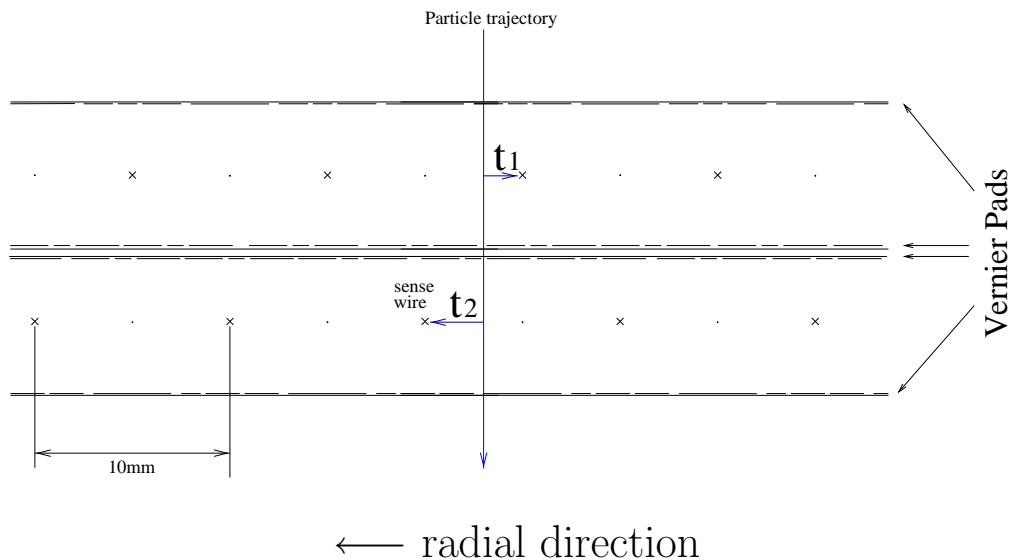


Figure 2.12: Cross-sectional view of a part of a chamber sector. It consists of two layers of drift cells staggered by half-cell.

This staggered-cell configuration allows us to measure the r -coordinate and the absolute time of the track simultaneously. It is expected that the difference between the drift times ($t_1 - t_2$) in the adjacent cells gives the r -coordinate of the track with $100 - 200 \mu\text{m}$ accuracy, while the mean time $(t_1 + t_2)/2$ gives the absolute time of the track with $\sim 5 \text{ ns}$ accuracy. This excellent timing resolution is important for the pattern recognition.

By the ratio of charges observed at both ends of a sense wire the z -coordinate along the wire can be initially located with an accuracy of $\sim 1 \text{ cm}$. The chamber walls are made of thin plastic foils. A thin layer of aluminum deposit on the four cathode foils is shaped to make a Vernier pattern as shown in Fig. 2.13. By a comparison of the charges induced on the two sets of Vernier pads of each cell it is possible to determine the z position with an accuracy of about $300 \mu\text{m}$ as reported in [35]

The chamber sectors and the volumes between them are filled with 50% He – 50% C_2H_6 gas mixture at 1 atm. Such a mixture is chosen to have sufficient ionization loss in the gas ($\sim 65 e^-/\text{cm}$ for minimum ionizing particles) as well as to minimize multiple Coulomb scattering of tracks ($X_0 \sim 650 \text{ m}$). This mixture has proved to work well in several existing experiments like BELLE [40] and BaBar [41]. The drift velocity saturates at roughly $4 \text{ cm}/\mu\text{s}$ for a relatively low electric field ($\sim 1.5 \text{ kV}/\text{cm}$) [42].

Fig. 2.14 shows the structure of a chamber sector and an assembly of 16 sectors to be inserted into the COBRA magnet. A foil of Kapton, $12.5 \mu\text{m}$ thick, is stretched on a frame made of carbon fiber. An array of sense and potential wires are also strung between the end-arms of the frame. Each frame with wires and foils is fixed to a support structure made of G10, which is then fixed to the inner wall of the magnet cryostat.

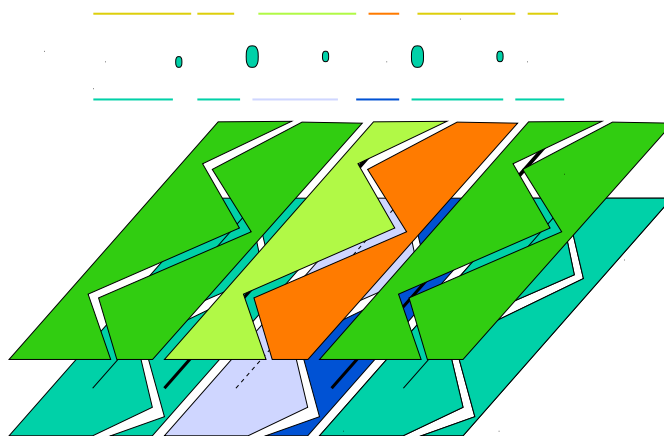


Figure 2.13: Structure of the cathode vernier strips.

2.3.4 Timing Counter

This detector is designed to measure the positron timing with a resolution better than 100 ps in FWHM and to be used in the trigger for selecting events containing a positron coincident in time and collinear in direction with a photon identified in the photon detector. Hodoscope arrays of plastic scintillators are placed on both ends of the positron spectrometer to provide the positron timing and trigger signal.

Fig. 2.15 shows the configuration of the timing counter, which consists of scintillator hodoscope and fiber bundle layers, orthogonally placed along ϕ and z directions, respectively. Each scintillator hodoscope is viewed from both ends by two photomultipliers, which measure the pulse heights as well as the arrival times of the scintillation light (t_L and t_R) at both ends. The time difference $t_L - t_R$ provide another measurement of the impact point along the scintillator, while the mean time $(t_L + t_R)/2$ measure the absolute impact time. For obtaining redundancy in z measurement a scintillating-fiber bundle layer is equipped on each hodoscope layer. Each scintillating-fiber bundle ($5\text{mm} \times 10\text{mm}$) is viewed by avalanche photo-diodes from both ends.

Because the detector is located under the magnetic field of the COBRA magnet, all the relevant devices must be operational under magnetic field. Due to this a fine-mesh dynode type photomultiplier (PMT) with a 2-inch diameter is chosen for hodoscope readout and the relative angle of the PMT to the magnetic field is carefully designed as shown in Fig 2.16. Performance tests of a full-size prototype have been conducted in the real COBRA magnetic field using a pulsed blue laser (60 psec pulse width) in order to investigate the gain and transition time spread of the PMT, and light transmission in the hodoscope.

As already mentioned above, an avalanche photo-diode (APD) will be employed for the scintillating-fiber bundle readout. This is because the APD keeps a good response even under the magnetic field due to its compact structure, and has better sensitivity to light than the PMT although attention has to be paid to handle small amplitude signal due to its lower gain. Vigorous studies on the APD is in progress to finalize the design in the collaboration. It is also an important issue to develop readout electronics with minimum amount of material in the magnet to avoid unexpected background to the photon detector while keeping the signal quality.

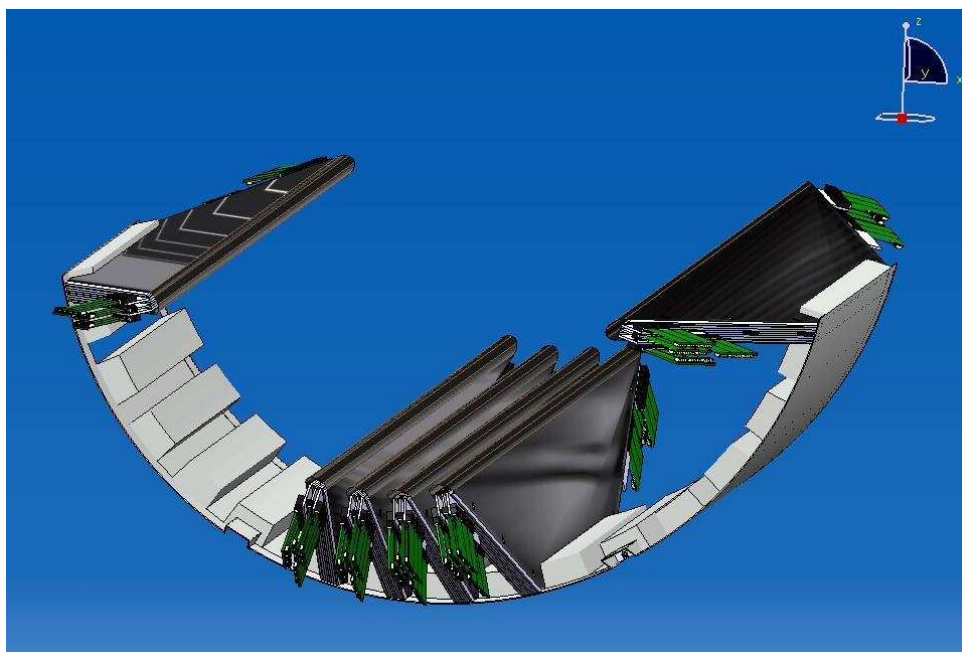
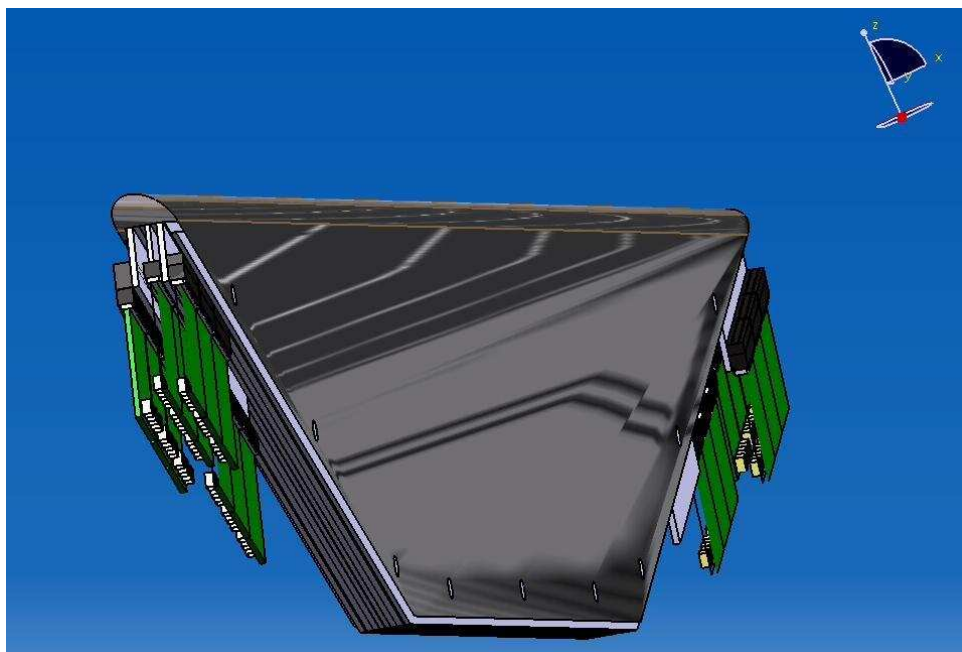


Figure 2.14: A sector of the drift chamber and an assembly of 16 sectors. Only 6 sectors are shown in the assembly.

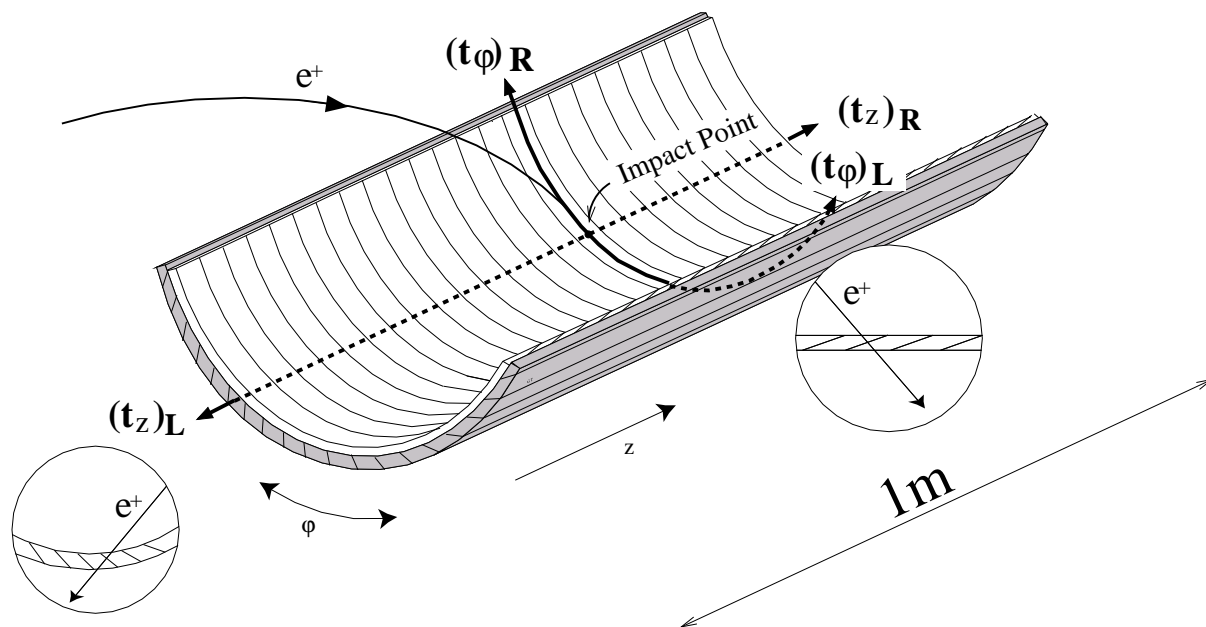


Figure 2.15: Configuration of the timing counter.

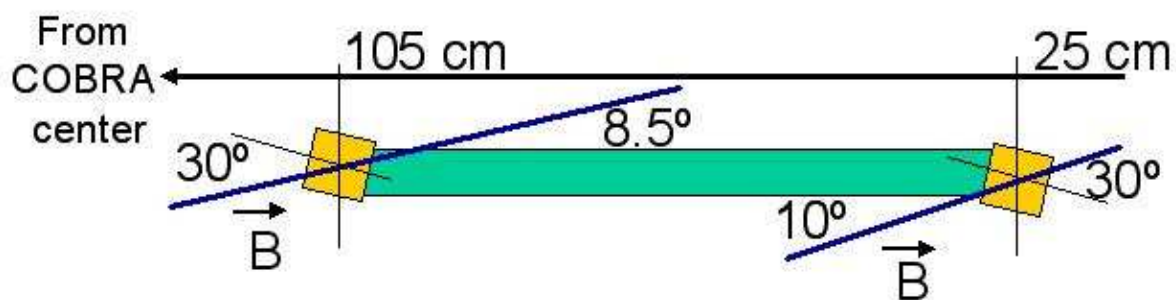


Figure 2.16: Geometry of the timing counter hodoscope with PMTs.

Chapter 3

Liquid Xenon Scintillation Detector

We adopt liquid xenon scintillator as a detector material as described in Sec. 2.1. The general properties of liquid xenon as a scintillation material and the technical details of the design of the 100-liter prototype detector are described in this chapter.

3.1 Liquid Xenon Scintillator

As described in Sec. 2.1, the requirement for γ -ray detector in MEG experiment is quite high. After some investigation, we chose liquid xenon (LXe) scintillator instead of crystal scintillators such as NaI, CsI, BGO, and so on in order to detect 52.8 MeV γ rays with accuracy. In this section, we describe the properties of the LXe scintillator as a detector material to show the advantages of the use of LXe in the γ -ray detector in the MEG experiment.

3.1.1 Why Liquid Xenon?

The requirements for the scintillator medium for the gamma-ray detector in the MEG experiment are the following,

- Large light yield
- Short radiation length
- Short decay time
- Short rise time

Is there such a scintillator medium? In general scintillators can be classified into two categories: organic and inorganic. Organic scintillators have fast response but have low light yield. Inorganic ones have high light yield but have slow response. Table 3.1 shows main features of various scintillators. For example PbWO_4 has a short decay time but a low light yield. NaI(Tl) , BGO, and CsI(Tl) have high light yield but long decay time. On the other hand LXe has good points of both organics and inorganics. LXe can be considered the best scintillator for the γ -ray detector in the MEG experiment.

LXe has some other advantages. Because LXe is not a crystal, the shape can be changed as we like and it is free from a problem of non-uniformity, cracks, and aging.

Table 3.1: Properties of various scintillators.

	LXe	LAr	NaI(Tl)	CsI(Tl)	CsI	BGO	PbWO ₄
Density (g/cm ³)	2.98	1.40	3.67	4.53	4.53	7.13	8.28
Radiation length (cm)	2.77	14	2.59	1.85	1.85	1.12	0.89
Mollier radius (cm)	4.2	7.2	4.5	3.8	3.8	2.4	2.2
Decay Time (nsec)	45	6.7	250	1000	10	300	5
slow component		1620			36		
Emission peak (nm)	178	127	410	565	305	410	440
slow component					480		
Light yield relative to NaI	0.75	0.9	1	0.4	0.1	0.15	0.01

It is difficult for crystal scintillators to be purified again after starting experiments. In case of LXe, it is possible to remove impurities at any moment. In fact, we developed a circulation purification system for xenon, which will be detailed in Sec. 4.2.

3.1.2 Properties of Xenon

Chemical and physical properties of xenon are summarized in Table 3.2.

Disadvantage of LXe is that we have to keep it at low temperature. We overcome this problem by using a vacuum-insulated cryostat and proper cooling system.

Table 3.2: Main properties of liquid Xe.

Material Properties	Value & Unit	Ref.
Atomic Number	54	
Atomic Mass	131.29 amu	[43]
Density at 161.35 K	2.98 g/cm ³	[44]
Boiling point	165.05 K	
Melting point	161.25 K	
Temperature at triple point	161.30 K	
Pressure at triple point	0.805 atm	
Density at triple point	2.96 g/cm ³	
Gas/Liquid volume ratio	518.9	[45]
Radiation length	2.77 cm	[46]
Critical Energy	14.5 MeV	[47]
Moliere radius	4.2 cm	[47]

Fig 3.1 shows the phase diagram of xenon. LXe is normally kept at 165 K and 1.3 atm in our detector. In this figure it can be seen that the temperature range of the liquid at 1.3 atm is narrow. A stable and powerful cryogenic system to keep the liquid stably is a key technology in the LXe detector. The cryogenic system in the 100-liter prototype is based on a cooling with a mechanical refrigerator and liquid nitrogen and is described in detail in Sec. 3.5

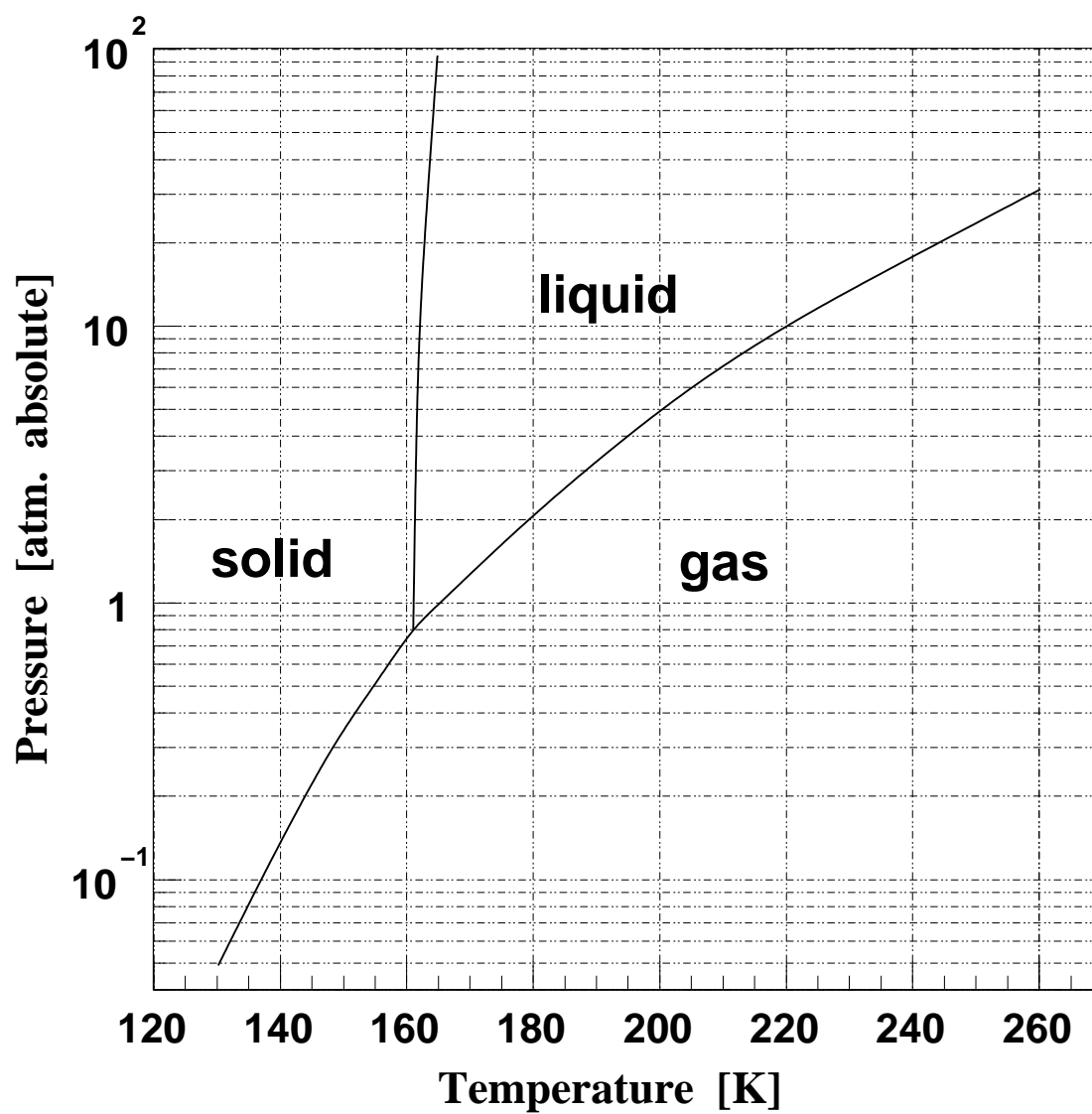


Figure 3.1: Xe phase diagram.

3.1.3 Scintillation of LXe

LXe has been known as a good medium for scintillators. Since the late 1970s, many new devices with liquid rare gas have been proposed and developed in the fields of elementary particle physics, nuclear physics, and astrophysics experiments. Properties of xenon scintillation are listed in Table 3.3. Some properties of xenon scintillation are not yet understood well.

Table 3.3: Scintillation photon of LXe.

Properties	Value & Unit	Ref.
Emission peak	178 nm	[48, 49]
Spectral width	14 nm	[48, 49]
Refractive index	1.57 to 1.72	[50–53]
W_{ph} for 1 MeV electrons	21.6 eV	[54]
W_{ph} for α particles	17.9 eV	[54]
Decay time (recombination)	45 ns	[55]
Decay time (Fast Components)	4.2 ns	[55]
Decay time (Slow Components)	22 ns	[55]
fast : slow	1 : 0.43	[55]
Absorption length	> 100 cm	Chap. 4
Scattering length	29 cm to 50 cm	[56–59]

The spectrum of LXe scintillation light has a single peak at 178 nm. The wavelength is slightly shorter than that of gaseous xenon (GXe).

Decay of LXe scintillation signal has two components: fast component and slow component. The fast and slow component is related to the light emission process:



where Xe^* is the first excited level of xenon, and $h\nu$ is VUV scintillation photon. The recombination process is presented by



where Xe^+ is a singly-ionized xenon, and Xe^{**} is the second excited level. In both processes, the excited dimer (excimer) Xe_2^* is de-excited to the dissociative ground state by emitting a single VUV photon since the energy gap between the lowest excited level and the ground state is so large that there is no decay channel such as non-radiative transition.

It is impossible for Xe scintillation photons to be re-absorbed by Xe molecules. since they are not emitted by the excited state Xe^* but by the excimer Xe_2^* [55]. This means that the scintillation photons are not absorbed by xenon itself.

Fig. 3.2 shows a cross section and mean free path of photon in xenon. The mean free path is 4.8 cm for 52.8 MeV and the maximum of mean free path is about 10 cm. In order to let 52.8-MeV gamma rays deposit their whole energy, the detector depth has to be 50 cm at least, being estimated from a simulation.

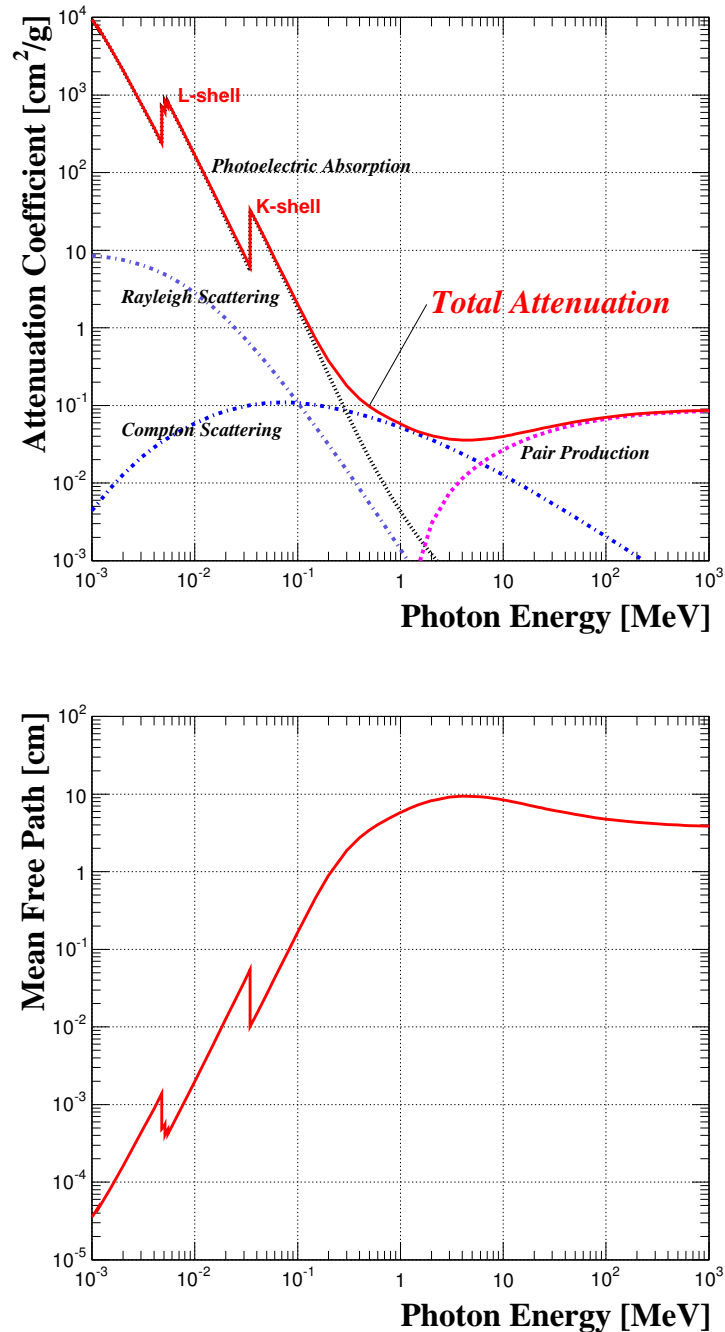


Figure 3.2: Photon cross section of Xe atoms (upper) and mean free path in LXe when its density is 2.98 g/cm^3 (lower).

Fig. 3.3 shows a typical LXe scintillation signal from γ -ray of 320 keV. In this figure a typical NaI(Tl) signal is also shown for comparison. It is clearly seen that the rise and decay time of LXe signal are much shorter than NaI(Tl) signal. LXe signal has the rise time of less than 10 nsec and the pulse settles down to ground level typically in 200 nsec. The short rise time and decay time of the signal are quite important features of the LXe scintillator for precise timing measurements and minimizing pile-up under high rate background, respectively.

Fig. 3.4 shows signals of the LXe scintillator from various kinds of particles. It can be seen that the decay time strongly depends on the particle type. This indicates that it is possible to discriminate particle type using pulse shape.

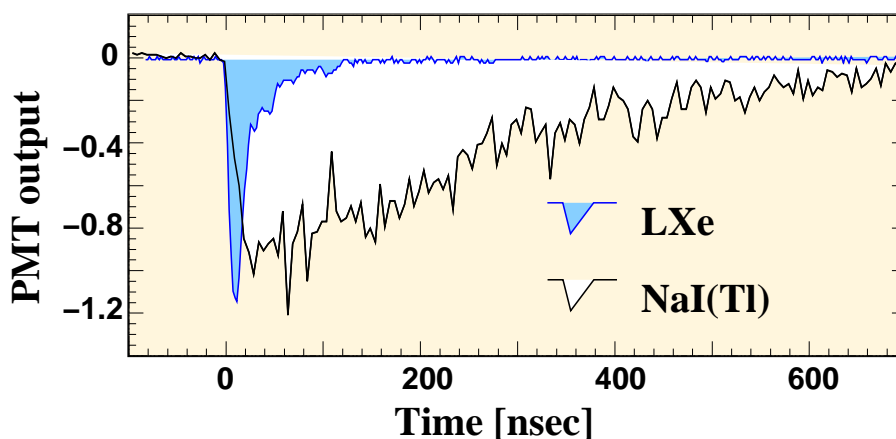


Figure 3.3: Typical LXe scintillation signal from 320 keV γ . A NaI(Tl) scintillation signal is also shown. The unit of PMT output is arbitrary. The pulses are normalized in the pulse height for comparison.

3.2 Strategy of Development of LXe Detector

We constructed two prototypes for demonstrating the performance of the planned LXe γ -ray detector in the MEG experiment. For comparison the specifications of the two prototypes and the planned final detector are summarized in Table 3.4.

Table 3.4: Three versions of LXe scintillation detectors.

Type	Prototype		Final design
	10-liter	100-liter	1000-liter
Fiducial volume	2.34 liter	68.6 liter	\sim 800 liter
Shape	rectangular	rectangular	C-shape
PMT	32	228	\sim 800
Cooling method	LN ₂	refrigerator+LN ₂	refrigerator+LN ₂
γ -ray energy for testing	up to 1.8 MeV	up to 128 MeV	up to 128 MeV

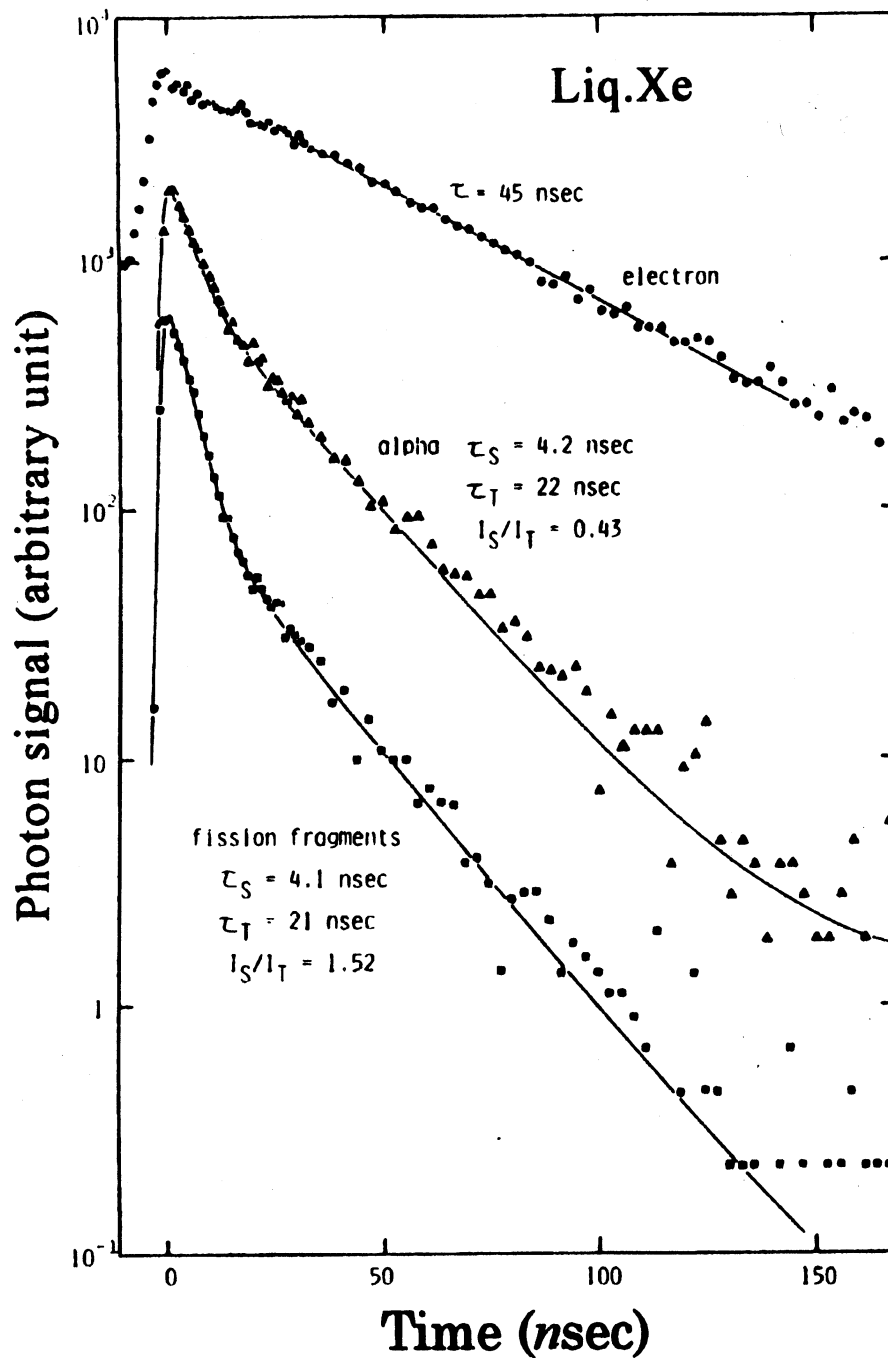


Figure 3.4: Decay curves of scintillation signals from LXe measured for electrons, α particles, and fission fragments. [60]

The details of the 10-liter prototype are described in Appendix A. We constructed a larger prototype with 100-liter liquid xenon after the feasibility study with the 10-liter prototype in order to evaluate the performance achievable in the final detector with more realistic conditions. The details of the design and the performance of this larger prototype (100-liter prototype) are described in the following sections.

3.3 100-liter Prototype of LXe Scintillation Detector

The energy of γ -ray source used in the tests with the 10-liter prototype was limited up to ~ 1.8 MeV because of its small volume and the system such as cryostat and vessel, and PMT holding frame were simplified and specialized for the 10-liter prototype.

On the other hand the 100-liter prototype can be considered to be a detector with the same scale as in the final detector except for its limited acceptance.

The purposes of the 100-liter prototype can be summarized as follows,

- Evaluate detector performance with higher-energy γ rays
- Introduce cryogenic system based on a mechanical refrigerator
- Study the long term stability of the detector
- Develop the slow control system for stable operation of the detector
- Develop a purification system.

A schematic view of the 100-liter prototype detector is shown in Fig. 3.5. It has an active volume of $372 \times 372 \times 496$ mm³ (69 ℓ) viewed from all sides by 228 PMTs assembled into a rectangular shape (Fig. 3.6). The cryostat consists of thermal insulated vessels equipped with a pulse tube refrigerator [61,62] and a liquid nitrogen cooling pipe. Several sensors are used inside the vessels for monitoring temperatures and pressures.

For avoiding interactions of γ -rays before the active volume of the detector the incidence face should not be massive. A thin aluminum plate and a honeycomb window made of stainless steel are used as an entrance window. Only 0.01% of incident gamma-rays interact in this entrance window. Thickness of the material used in the front face including the PMTs and the holder is as thin as $0.24 X_0$ within the entrance window as illustrated at the bottom of Fig. 3.5.

The signals from the PMTs are taken out of the cryostat with a high-density feed-through which was originally developed for the liquid argon calorimeter in ATLAS experiment [63].

In order to reduce the amount of the liquid the space outside the active volume is stuffed with hollow fillers made of SUS and aluminum plates.

The detector is equipped with 8 blue LEDs and four ²⁴¹Am α sources, two LEDs and one α source on each lateral face, for PMT calibration. Three pairs of trigger counters (TC1, TC2, and TC3) are placed above and below the vessel to select cosmic ray muons traversing the LXe for various tests.

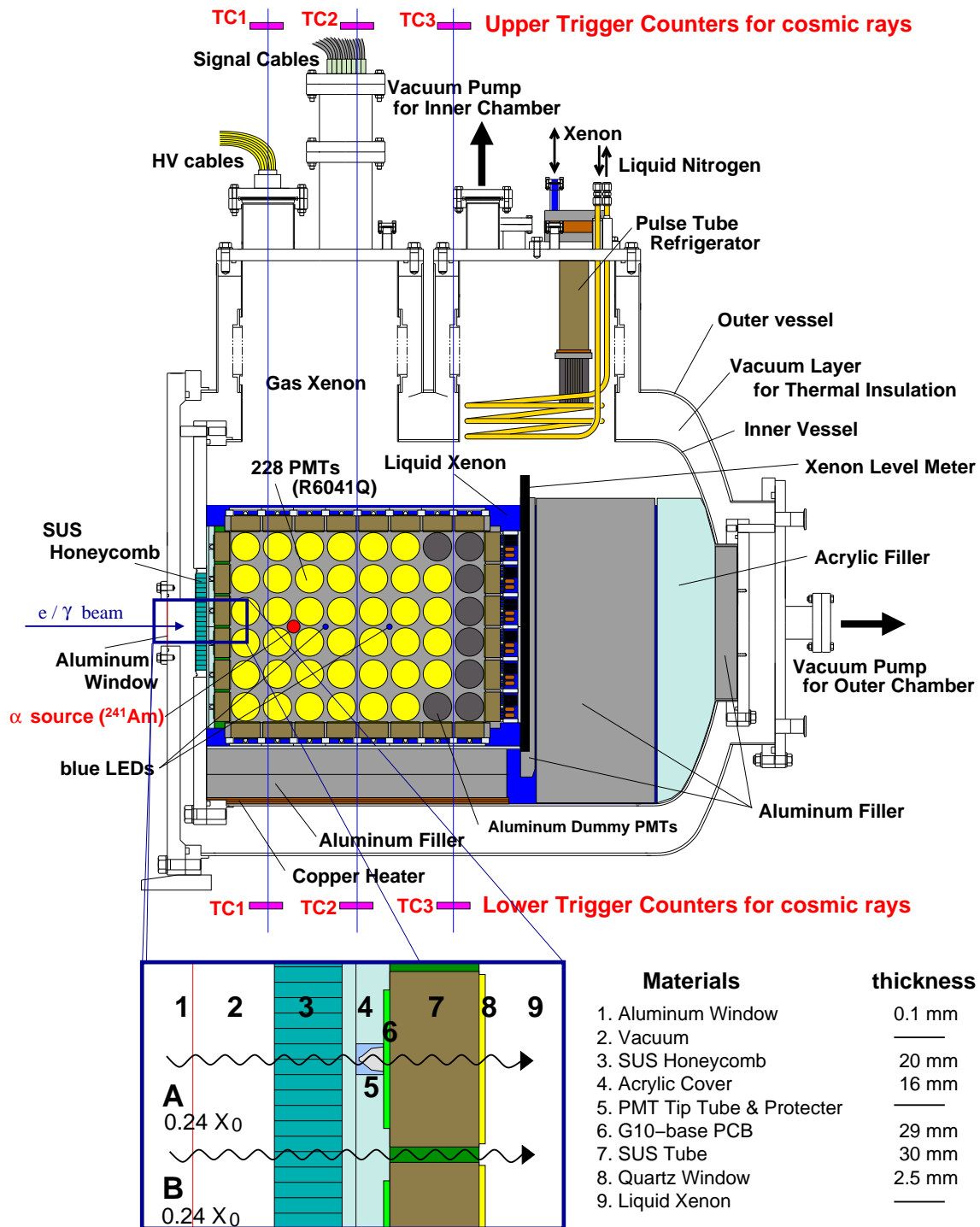


Figure 3.5: Schematic view of the 100-liter prototype of the LXe scintillation detector.

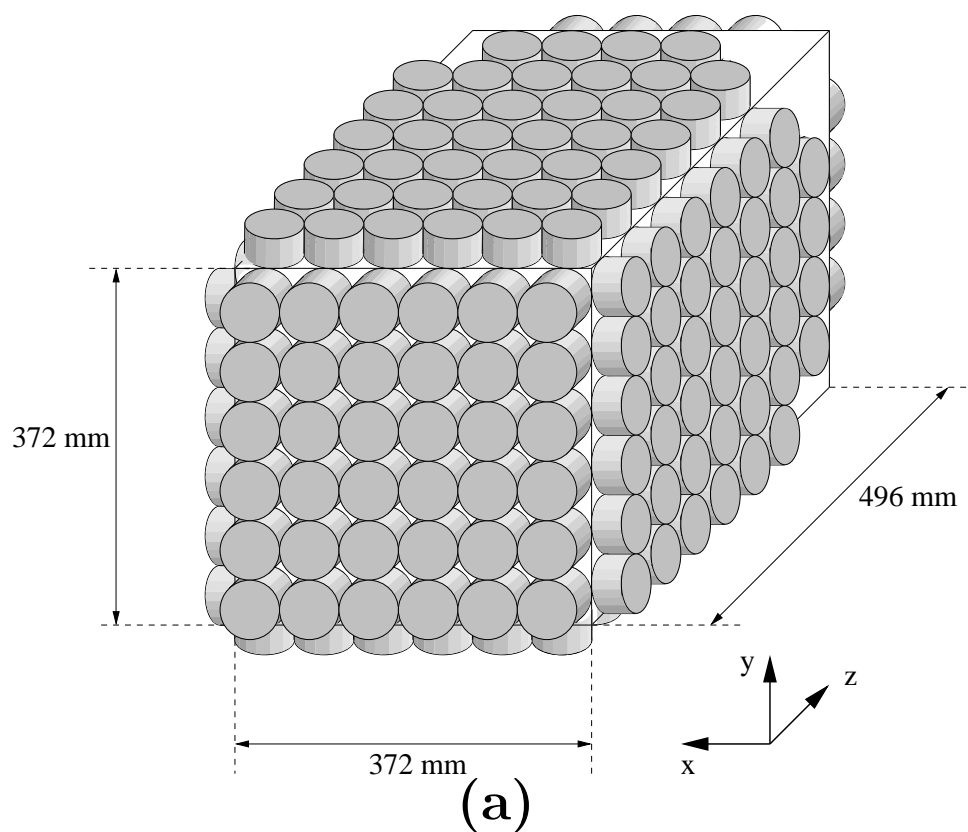


Figure 3.6: (a) Schematic view of the PMT holder. (b) Picture of the PMT holder in the 100-liter prototype detector from the front. Front face structure is mainly made of G10 and acrylic.

3.4 Photomultiplier

Photomultiplier (PMT) is the most essential item in the LXe detector. The PMTs are immersed in the LXe to collect as many scintillation photons as possible. The requirements for the PMT in the LXe detector can be summarized as follows:

- Operational at LXe temperature (165 K).
- VUV-sensitive photo-cathode.
- VUV-transparent window
- Pressure-proof up to 3 atm.
- Compact
- Low out-gassing.

We have been developing the PMT to meet these severe requirements in cooperation with HAMAMATSU photonics. The properties of the PMT (HAMAMATSU R6041Q) used in the 100-liter prototype are summarized in Table 3.5. Fig. 3.7 illustrates the charge multiplication process in the metal channel dynode PMT. The voltage divider circuit of the R6041Q is shown in Fig. 3.8.

Table 3.5: The properties of the PMT (R6041Q). These are typical values.

Properties	Value
Size	2 inch (51 mm)
Dynode type	Metal channel
Number of Dynodes	12
Photocathode material	Rb-Cs-Sb
Active Area Diameter	45 mm
Window	Synthetic quartz
Typical HV	900 V
Typical Gain	1×10^6
Dark Current	5nA
Rise Time	2 nsec
Transit Time	12.5 nsec
Transit Time Spread (TTS)	0.75 nsec
Cathode Radiant Sensitivity	74 mA/W
Cathode Luminous Sensitivity	200 A/lm
Anode Luminous Sensitivity	70 A/lm

Since the LXe detector will be placed close to the magnet, the PMT used in the LXe detector have to work under the fringing field from the magnet.

Fig. 3.9 shows the relative output of the PMT as a function of the magnetic field [64] where the z -axis is defined by the PMT axis. The output degradation due to the magnetic field strongly depends on the direction of the applied magnetic field with respect to the

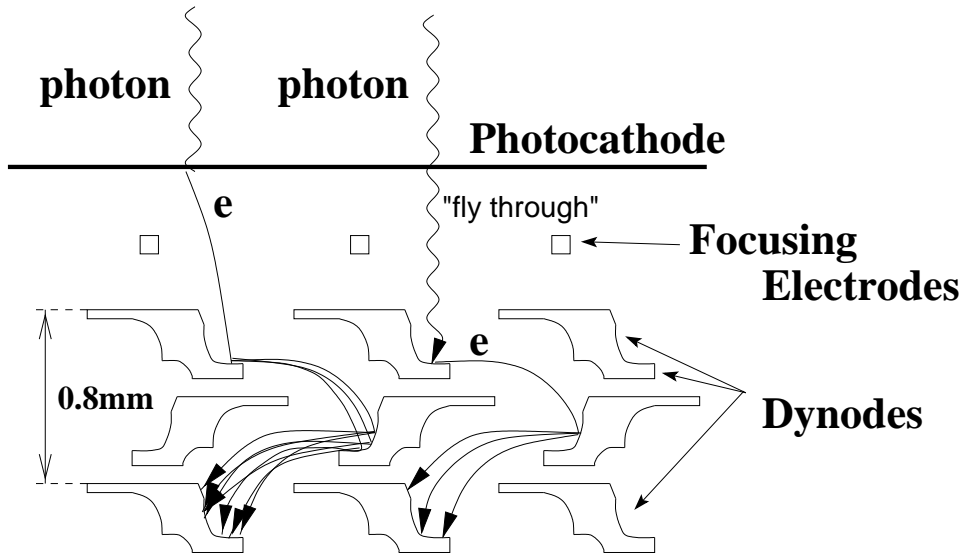


Figure 3.7: Charge multiplication process in the metal channel dynode PMT. Some photons directly hit the first dynode.

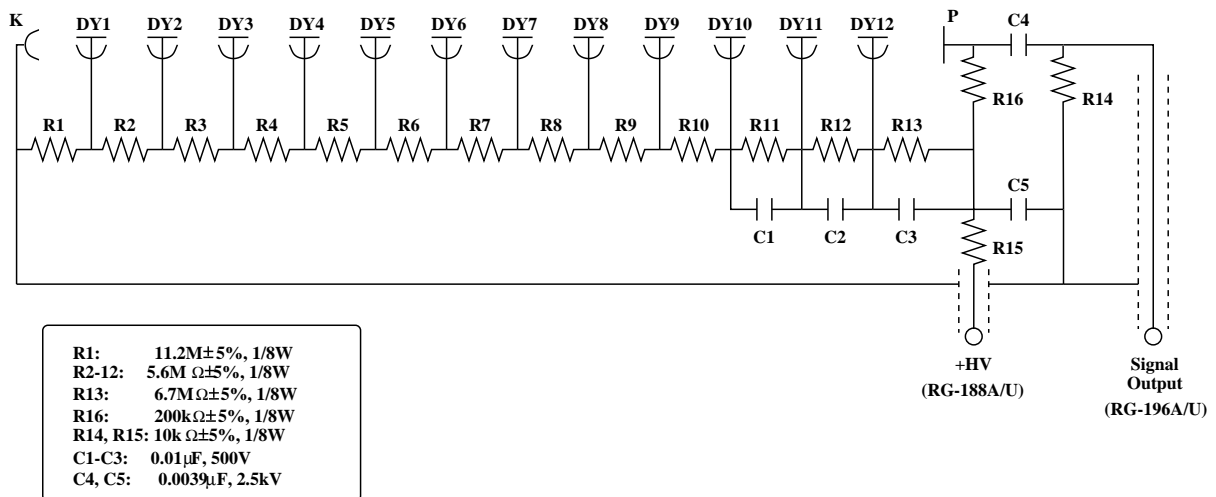


Figure 3.8: Voltage divider circuit of R6041Q.

tube axis. There is a strong dependence even on the direction on the photo-cathode plane due to the structure of the dynodes. The maximum allowed strength of the magnetic field is 150 Gauss and 50 Gauss for the perpendicular and parallel directions to the tube axis, respectively. The maximum allowed strength is defined as the field strength which reduces the relative gain of the PMT by 50%.

As mentioned in Sec. 2.3.2, we succeeded to reduce the fringing field from the magnet down to 50 Gauss level in the LXe detector region by canceling the field using compensation coils.

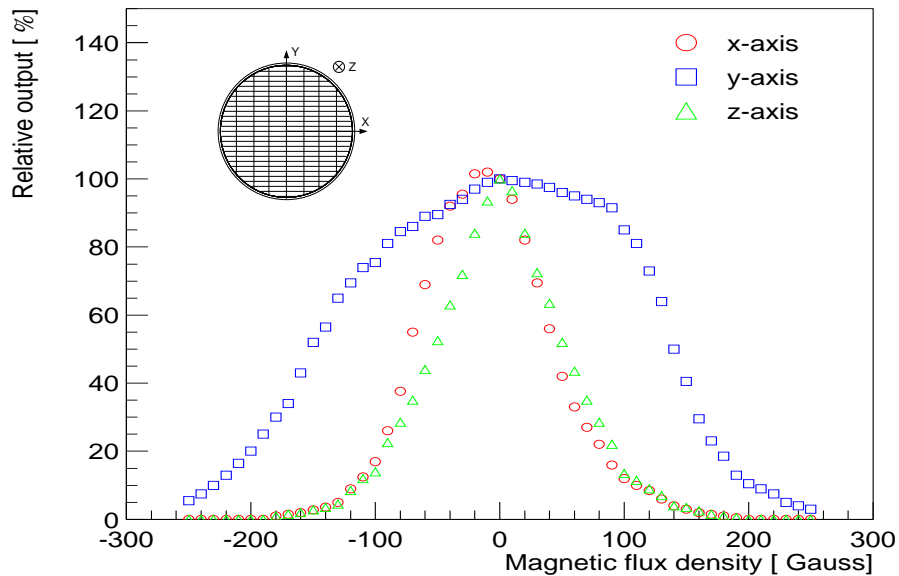


Figure 3.9: Relative output of R6041Q to be used in the LXe detector as a function of the applied magnetic field. The z -axis is defined by the PMT axis here.

3.5 Cryogenics

As described in Sec. 3.1.1, the temperature range of LXe at a reasonable pressure is rather narrow. Stable and powerful cryogenic system is indispensable for the proper operation of the LXe detector.

As shown in Fig. 3.5, the 100-liter prototype has a cryostat composed of pulse tube refrigerator, thermally insulated vessels, and cooling pipe for liquid nitrogen. The inner vessel is isolated from outside by vacuum of 10^{-4} Pa \sim 10^{-3} Pa for thermal insulation. By using multi-layer super-insulation foils in the insulation vacuum, heat inflow due to thermal radiation is reduced down to 24 W which is well below the cooling power of the cooling system based on the refrigerator and the liquid nitrogen cooling pipe.

A new pulse tube refrigerator was developed for the 100-liter prototype [65] (Fig. 3.10). The remarkable features of the refrigerator are summarized below.

- Easy to use
- Effective direct re-condensing
- Compact cooling part
- No cryogen required
- No sub-cooling required

- Quiet environment
- Eco-friendly
- Possibly long life

The refrigerator consists of two parts: helium compressor (LEYBOLD Coolpak series) and cold head (developed in KEK). The compressor can be placed several meters away from the cold head installed on the top flange of the cryostat. The refrigerator produces much less noise because there is no mechanical moving part around the cold head. The specifications of the refrigerator are listed in Table 3.6. The refrigerator has a cooling power of 70 W at 165 K which is well above the heat load in the cryostat of the 100-liter prototype (Table 3.7).



Figure 3.10: Pulse tube used in the refrigerator of the LXe detector. The right is the pulse tube for the 100-liter prototype with a cooling power of 70 W at 165 K. The left is the latest version which will be used in the final detector and its cooling power is improved up to 190 W at 165 K.

As shown in Fig. 3.5, the cryostat is also equipped with the cooling pipe in the inner vessel where liquid nitrogen can flow. The liquid nitrogen cooling pipe is only used for the liquefaction of xenon and also in case of emergency such as a power cut. During the normal operation of the detector, the LXe is cooled only by the refrigerator.

Table 3.6: Refrigerator performance.

Cooling Power at 165 K	70 W
Surplus Power	20 W
Compressor Power	2.2 kW
Compression Cycle	2.2 Hz
Coefficient of Performance (COP)	3%

Table 3.7: Heat load in the cryostat of the 100-liter prototype.

	Static	PMT	Cable	Total
heat Load [W]	24	16	10	50

3.5.1 Operation

The vessel of the 100-liter prototype has to be filled with ~ 120 liter LXe in total. Some preparations are needed to bring the 100-liter prototype into operational conditions, and it normally takes half a month to complete all the processes of the preparation.

All the processes of the cryogenic operation are monitored and controlled by the slow control system based on the MSCB [66]. The control software was developed with LabVIEW [67] as shown in Fig. 3.11.

Evacuation: Both the inner and outer vessels are initially evacuated. The best procedure for removing water adsorbed in the materials inside the vessel would be to bake the inner vessel above 200 °C. The baking temperature for the inner vessel is, however, limited up to 70 °C because of the temperature tolerance of the PMTs and acrylics inside the inner vessel. After the continuous evacuation for about ten days the inner pressure reaches 10^{-3} Pa.

Pre-cooling: A pre-cooling phase then starts in order to cool the inner vessel down to 165 K prior to liquefaction. The inner vessel is filled with gaseous xenon (GXe) of 0.2 MPa, and then cooled by both the liquid nitrogen cooling pipe and the refrigerator for a whole day.

Liquefaction: Xe is liquefied by using the liquid nitrogen cooling pipe after the inner vessel is sufficiently pre-cooled. The GXe is purified with a gas purifier (SAES Getter [68]) and molecular filters (Oxisorbs [69]) before entering the inner vessel and getting liquefied. The gas purifier can adsorb various contaminants in the GXe such as H₂O, O₂, CO₂, N₂, and CH₄ down to a ppb level. The molecular filter can adsorb oxygen. It usually takes two days to complete the liquefaction. The vapor pressure is kept constant by controlling the flow of the GXe and flow of liquid nitrogen in the cooling pipe.

Keeping LXe: After the liquefaction, the LXe is maintained at 165 K and 1.3 atm mainly by the pulse tube refrigerator.

During the beam tests at the AIST we kept the LXe stable over about 2000 hours.

Recovering and Warming-up: After the detector operation the LXe is recovered to a storage tank. The refrigerator is turned off and the outer vessel is filled with heat exchange gas (gaseous nitrogen) to accelerate the LXe evaporation, and a heater under the PMT holder is switched on. The tank is cooled down by liquid nitrogen in order to re-condense the xenon from the detector vessel. The recovery and warming-up of the cryostat take two and four days, respectively.

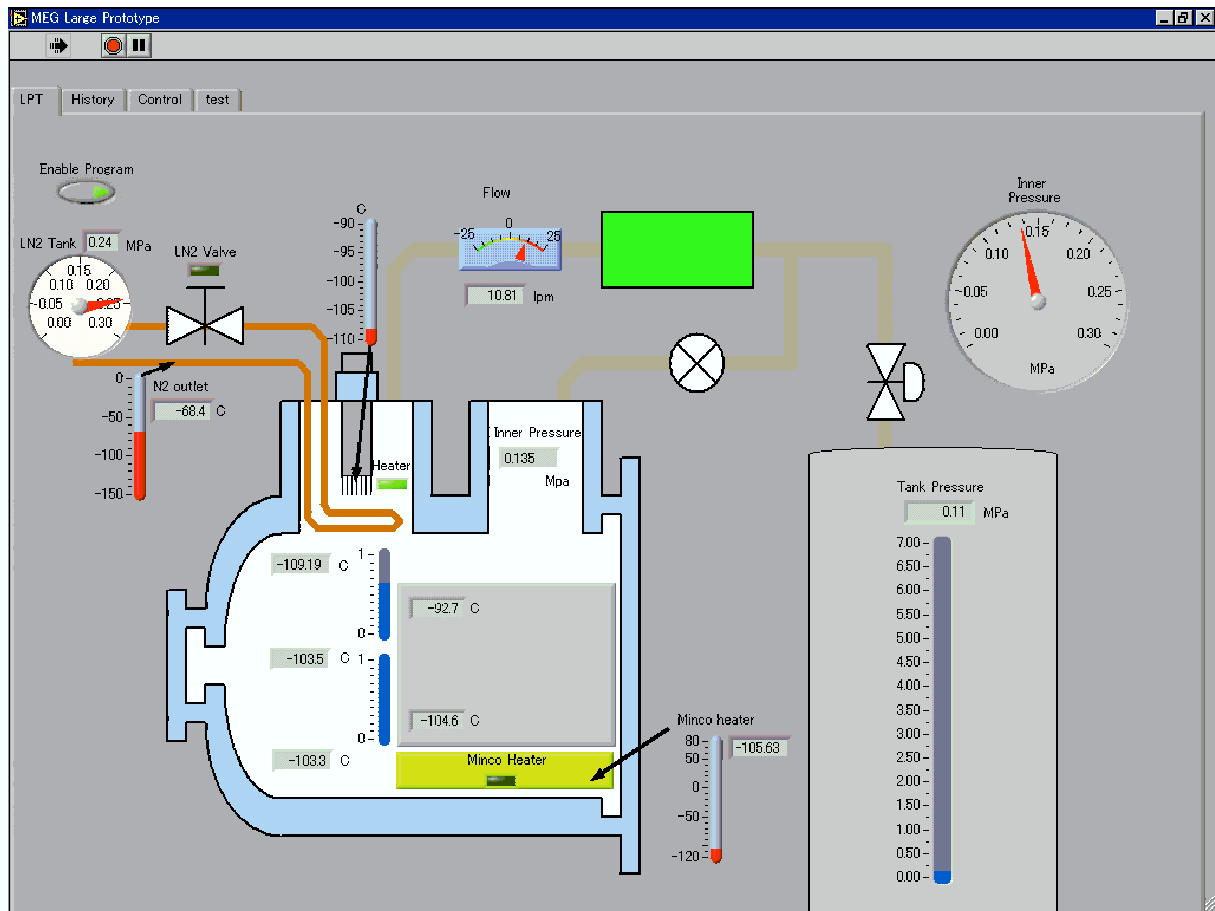


Figure 3.11: Control software of the cryogenic system of the 100-liter prototype developed with LabVIEW.

3.6 Monte Carlo Simulation

The Monte Carlo (MC) simulation for the 100-liter prototype detector was coded based on GEANT3 [70]. This simulation has run modes such as γ -rays, cosmic muon rays, and α particle in order to compare with measured data. Since GEANT3 can not simulate transportation of scintillation photons, we coded a ray-tracing routine for scintillation photons. The routine has some features. In the MC simulation, every scintillation photo has each wavelength which obeys a Gaussian distribution, and for each photon Rayleigh scattering and absorption length in LXe, reflectance and transmittance to quartz are defined according to the wavelength. Tab. 3.8 shows the parameters and their values in the MC simulation. An example of simulation event for 40-MeV γ ray is shown in Fig. 3.12. In this thesis the MC simulation was employed especially for estimation of QE.

Table 3.8: Parameters and values in the MC simulation for the 100-liter prototype detector.

Parameter	Value
Wph(α) (LXe)	18.1 eV
Wph(α) (GXe)	18.1 eV
Wph(e) (LXe)	21.6 eV
Scintillation Spectrum	178 nm \pm 2.1 nm (1σ)
Refractive index of xenon	1.62
Rayleigh Scattering Length	45 cm
Absorption Length (LXe)	1 m
Quantum efficiency	5%
Transmissivity of 2.5-mm Quartz	0.792
Refractive index of quartz	1.58
Absorption Coefficient on PMT holder	1.0 (no reflection)

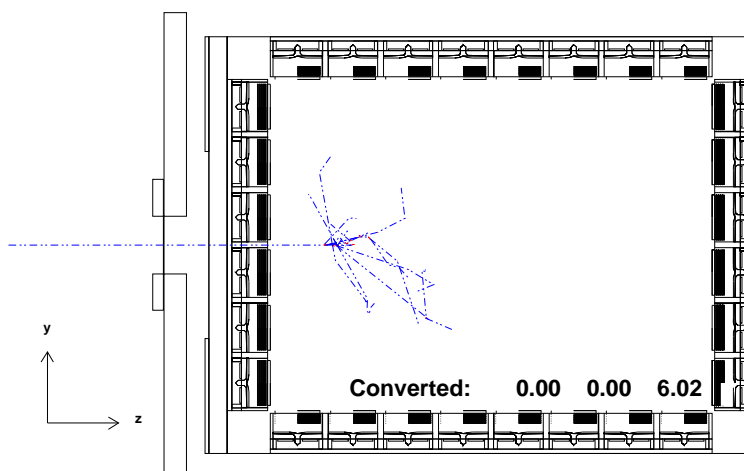


Figure 3.12: An example of MC simulation for 40 MeV γ ray. In this event the first conversion depth is at 6 cm from the PMT surface of the incident face.

Chapter 4

Purification and Absorption Length

LXe should in principle be transparent to its own scintillation light thanks to the scintillation mechanism through the excimer state Xe_2^* [55] as mentioned in Sec. 3.1.3. However possible contaminants in LXe, such as water and oxygen at ppm level, considerably absorb scintillation light [71,72]. Such contaminants have to be minimized in the LXe of our detector because the loss of the scintillation light will deteriorate the detector performance. We, therefore, developed a circulation-purification system for the 100-liter prototype. In this chapter we describe the performance of this purification system and discuss the impact of transparency of LXe on the expected performance of our detector for 52.8 MeV γ -ray.

4.1 Optical Properties of LXe

Firstly we discuss the optical properties of LXe that are of interest for a scintillation detector. The main optical properties of LXe are listed in Table 4.1.

Table 4.1: Optical properties of LXe.

Material Properties	Value & Unit	Ref.
Refractive index at scintillation wavelength	1.6 – 1.7	[50, 53, 73]
Peak scintillation wavelength	178 nm	[48, 49]
Scintillation spectral width (FWHM)	~ 14 nm	[48, 49]
Absorption length λ_{abs}	> 100 cm	present work
Scattering length λ_{sca}	29 - 50 cm	[53, 56–58, 73]

Light attenuation in LXe can be described by the attenuation length, λ_{att} , as defined in the equation, $I(x) = I_0 e^{-x/\lambda_{\text{att}}}$. The attenuation length consists of two separate components, the absorption length, λ_{abs} , describing real absorption and loss of photons, and the scattering length, λ_{sca} , that represents elastic scattering of photons without any loss. For the elementary photon scattering they are related by: $1/\lambda_{\text{att}} = 1/\lambda_{\text{abs}} + 1/\lambda_{\text{sca}}$. For an actual photon beam one must take into account the fact that photons can be forward scattered. In our case the elastic scattering is dominated by Rayleigh scattering, therefore λ_{sca} may be regarded as the Rayleigh scattering length, λ_{Ray} . The knowledge of refraction index n in the region of the xenon VUV light emission is also relevant.

The most important among these parameters for the detector performance is the absorption length λ_{abs} , since the energy measurement relies on the total number of scintillation photons detected by the PMTs that surround and view the LXe volume from all sides and is therefore not affected by photon scattering.

The experimental knowledge of these quantities, λ_{att} , λ_{abs} , λ_{sca} and n for pure LXe is poor. Especially no measurement of λ_{abs} has been made before. There are also some discrepancies among the available experimental data, which might partly be explained by the degree of purity of the LXe. As we shall show later, small amounts of VUV absorbing molecules like H_2O or O_2 , at the level of a few parts per million, can dramatically change LXe optical parameters. Thus a reliable determination of optical parameters necessarily requires monitoring the level and the stability of the xenon purity. In addition a size of the LXe volume comparable to the absorption/scattering lengths is needed to make a reasonable measurement of these lengths.

Considering the scintillation mechanism of LXe through the excimer state Xe_2^* [55], absorption in pure LXe is improbable, i.e. $\lambda_{\text{abs}} \sim \infty$; any absorption is thus caused by VUV absorbing impurities. In this paper we report the first measurement of λ_{abs} using our prototype and present a significant lower limit.

In contrast to the situation for LXe, better information is available for gaseous xenon (GXe) at various pressures both for visible and VUV light [74–76]. One can then examine if optical properties for LXe can be derived from those for GXe, although this might imply a daring extrapolation in terms of density. For a non-polar gas like xenon, however, this extrapolation proves to be valid [53]. One has to ascertain up to which value of photon energies the extrapolation maintains its validity. This point was further investigated by us [77]; the extrapolation is reliable up to a photon energy of 8.1 eV. At higher energies and closer to the first xenon absorption line at 8.3 eV the extrapolation is no longer valid. Our prediction for the value of the LXe refractive index at its emission line (7 eV corresponding to the wavelength of 178 nm) is $n = 1.65 \pm 0.03$. Most of the information obtained for GXe in various physical conditions can be used for reliably predicting other LXe optical properties [77]. Here we restrict the discussion to the relation between two quantities: n and λ_{Ray} .

For a dense fluid like LXe λ_{Ray} depends on density and temperature fluctuations of the medium, according to the Einstein's expression [78]:

$$\frac{1}{\lambda_{\text{R}}} = \frac{\omega^4}{6\pi c^4} \left[KT\rho^2\kappa_T \left(\frac{\partial \epsilon}{\partial \rho} \right)_T^2 + \frac{KT^2}{\rho c_v} \left(\frac{\partial \epsilon}{\partial T} \right)_\rho^2 \right] \quad (4.1)$$

where ϵ is the dielectric constant, κ_T is the isothermal compressibility, c_v is the specific heat at constant volume and K is the Boltzmann's constant.

Since xenon is a non-polar fluid, the second part of Eq. 4.1 comes out to be negligible [44, 53, 79]. The derivative appearing in the first part of Eq. 4.1 can be computed from the Clausius-Mossotti equation:

$$\frac{\epsilon(\omega) - 1}{\epsilon(\omega) + 2} = \frac{4\pi}{3} \frac{N_A \alpha(\omega) \rho}{M}, \quad (4.2)$$

where N_A is the Avogadro's number, $\alpha(\omega)$ is the molecular polarizability and M is the molecular weight. The Einstein's equation reduces then to:

$$\frac{1}{\lambda_{\text{R}}} = \frac{\omega^4}{6\pi c^4} \left[KT\kappa_T \frac{(n^2 - 1)^2 (n^2 + 2)^2}{9} \right]. \quad (4.3)$$

This equation establishes therefore a useful relation between the index of refraction in pure LXe and the Rayleigh scattering length.

4.2 Xenon Purification

In Fig. 4.1 (a) the absorption coefficients for VUV light are shown for 1 ppm contamination of water vapor [80] and oxygen [81]. The absorption spectra of water and oxygen largely overlap with the xenon scintillation spectrum. Given these absorption coefficients and neglecting the scattering ($\lambda_{\text{abs}} < \lambda_{\text{Ray}}$), we calculated the light intensity as a function of the distance from the light source for various concentrations of the contaminant. The result is shown in Fig. 4.1 (b) and (c). Apparently water is the most dangerous contaminant. Since water tends to absorb light with shorter wavelengths, only a component with longer wavelengths survives for a long distance. This might explain the discrepancies among the measurements of the LXe refractive index n , as n varies rapidly as a function of the wavelength in the vicinity of the scintillation wavelength.

As we already noted in Sec. 3.5.1, xenon is well purified before filling the detector vessel, but some inner components of the prototype are made of G10 and acrylic that are known to absorb and desorb water. During the initial stage of the prototype operation, a strong absorption of scintillation light was observed.

We investigated on the residual gas in the inner vessel of the 100-liter prototype by means of mass spectroscopy. A quadrupole mass spectrometer [82] was used in this gas analysis. The result is shown in Fig. 4.2. There are several peaks and they correspond to He (mass number=4), H₂O (18), N₂ (28), O₂ (32), and CO₂ (44). The peak at Mass = 65.5 corresponds to doubly ionized xenon Xe⁺⁺. It was found that water contamination was the dominant in the vessel while the oxygen concentration was an order of magnitude smaller. The level of other VUV absorbing contaminants such as hydrocarbons was more than two orders of magnitude smaller. We concluded that water at the ppm level seemed to be desorbed from the detector material into LXe.

We therefore introduced a circulation-purification system in the 100-liter prototype as schematically shown in Fig. 4.3, to remove the water. In this system, xenon, taken from the bottom of the vessel through the Teflon tube and evaporated by the heat exchanger, is pumped by a diaphragm pump and circulated through the gas purifier and the molecular filter, and is finally condensed back into the detector. The flow rate of GXe is about 500 cm³/min, hence the whole volume could be circulated in a few month time. We also carried out various tests to study the purification process, such as stopping or changing the flow rate and bypassing the purifiers or the filters.

4.3 Absorption Length Estimate

Purification was continuously performed for over 1200 hours. To evaluate and monitor light absorption in LXe separately from Rayleigh scattering during purification, we used cosmic ray muons as well as the α sources.

The total number of photoelectrons collected by all the PMTs (N_{pe}) for each cosmic ray event, being sensitive only to the loss of the scintillation photons, is a good measure of the light absorption. Note that cosmic rays triggered by pairs of scintillation counters TC1, TC2 and TC3 (Fig. 3.5) traversed vertically the front, middle and back parts of the

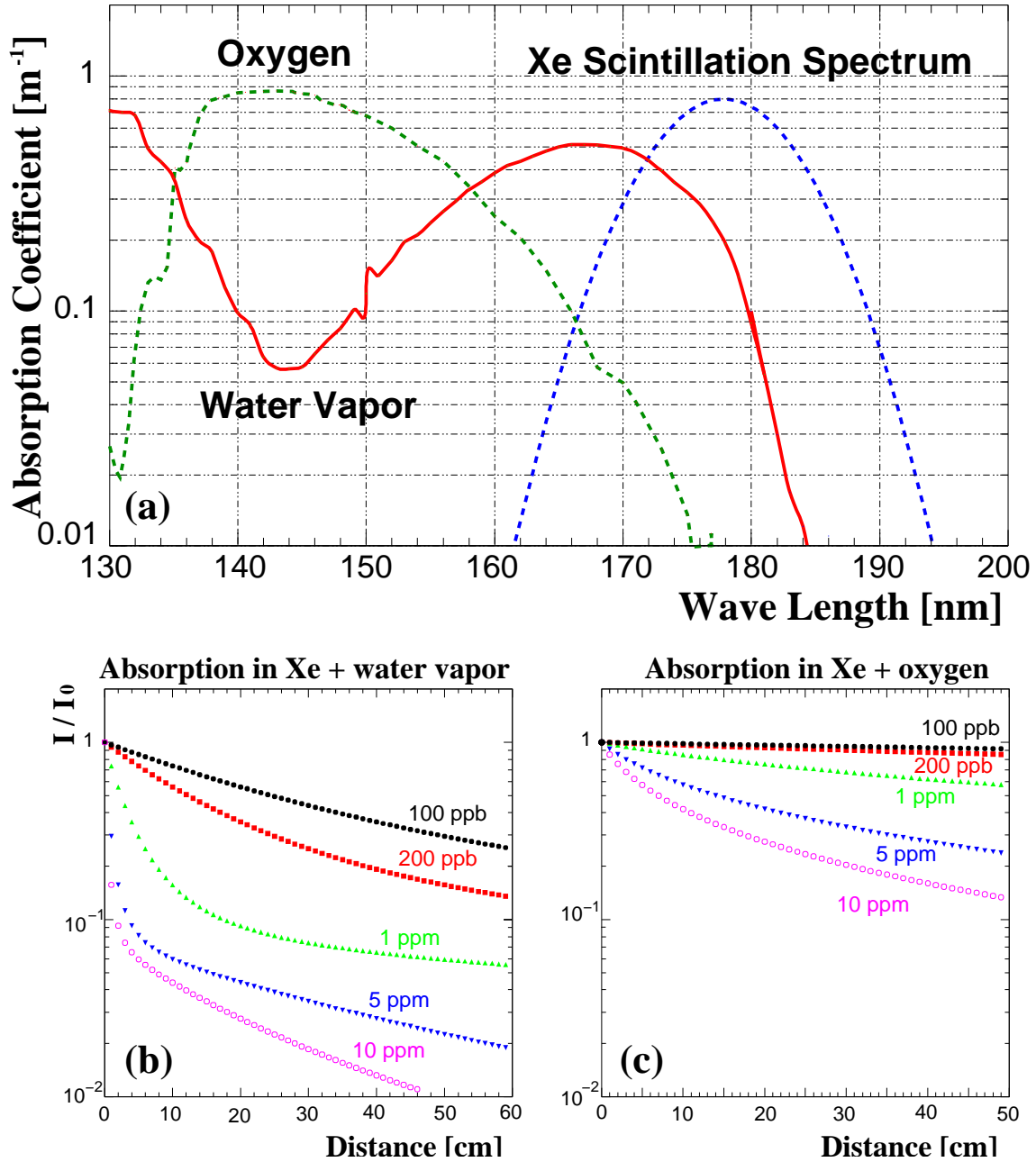


Figure 4.1: (a) Absorption coefficient for VUV photons in 1 ppm water vapor and oxygen. The Xe scintillation spectra is superimposed. (b) Light absorption calculated for various concentrations of water in LXe, where the source of scintillation photons is placed at $d = 0$, and I/I_0 is relative intensity of scintillation photons at a distance from the source. (c) Light absorption for oxygen.

detector. In Fig. 4.4 (c), the number of photoelectrons (N_{pe}) is plotted as a function of time for the cosmic rays triggered by TC2. It increased by a factor of four in about one month (700 hours) and almost saturated. Fig. 4.4 (a) and (b) show spectra of the total N_{pe} for cosmic rays before and after the purification, respectively. In a more careful study the number of photoelectrons collected by the front (or back) PMTs were compared for

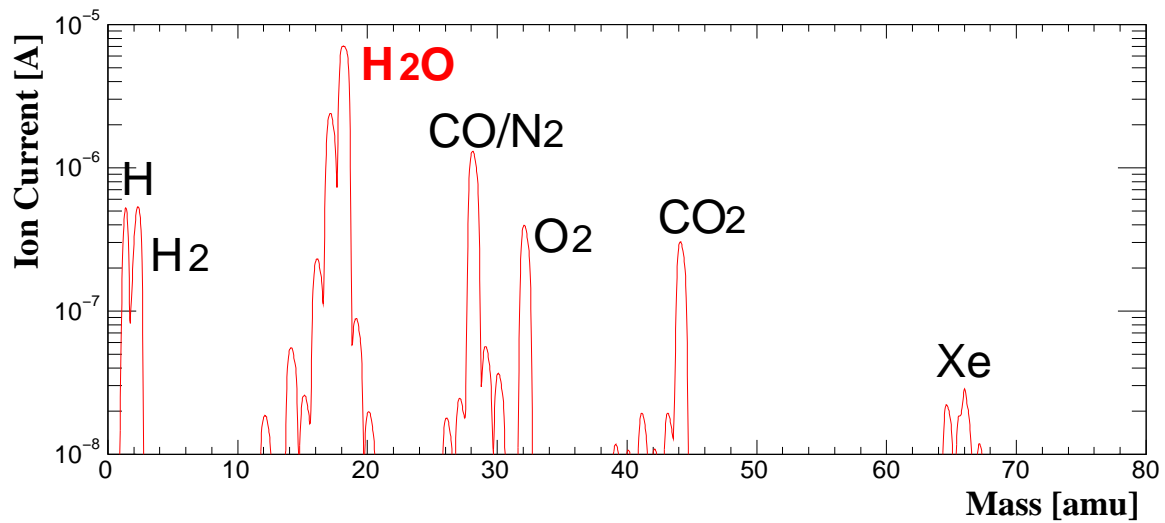


Figure 4.2: Mass spectrum obtained in the residual gas analysis. The multi-peak is caused mainly by decomposition of the parent molecule or by recombination with ions generated from the decomposition. For instance, the neighbors of H₂O(18) are H₃O⁺(19), OH⁺(17), O⁺(16), and so on.

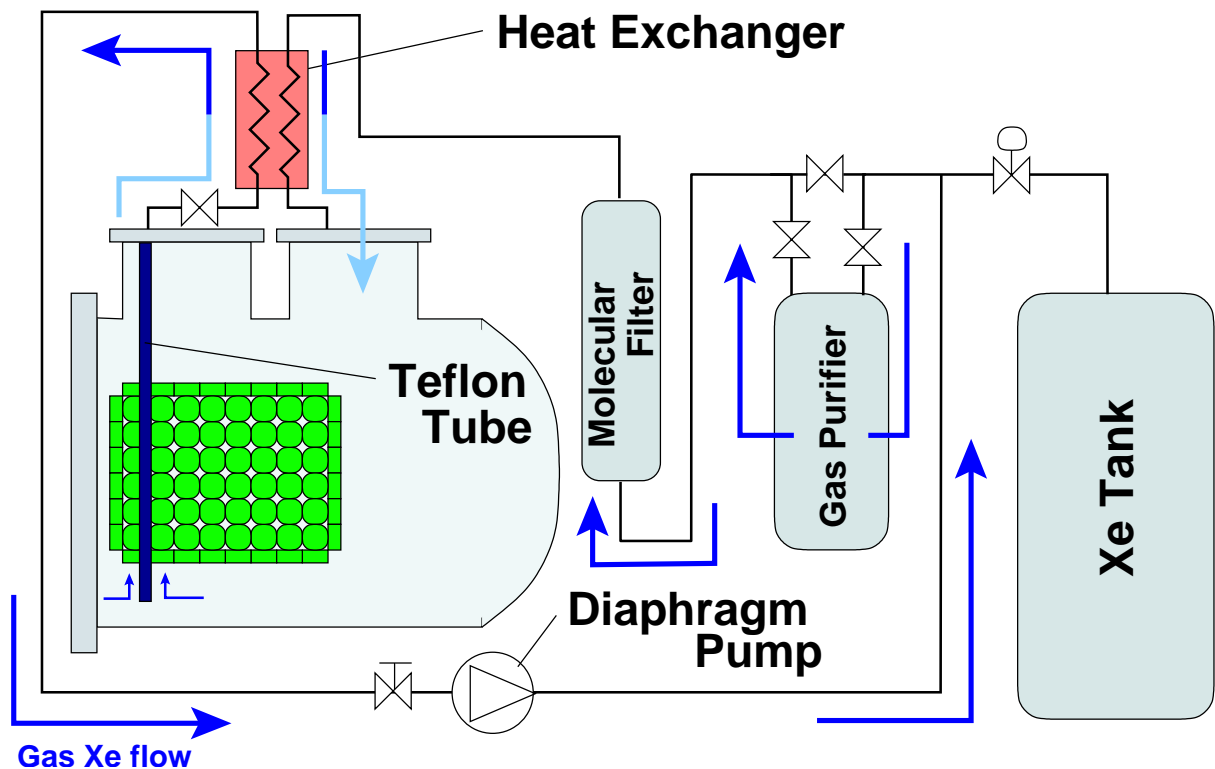


Figure 4.3: Setup for circulation and purification of xenon.

the events triggered by TC1, TC2 and TC3. A comparison with a Monte Carlo simulation indicates that λ_{abs} increased from ~ 10 cm to above 1 m.

Fig. 4.5 (a) shows spectra of the total N_{pe} for α particle events before and after the purification. In Fig. 4.5 (b) the relative changes in the α peaks of the PMTs located at certain distances (7.6 cm and 11.6 cm) from the α sources are plotted. For the PMTs at a longer distance, the PMT outputs increased much more significantly and saturated slightly later, just as expected for the light absorption in LXe, $e^{-x/\lambda}$ with increasing λ .

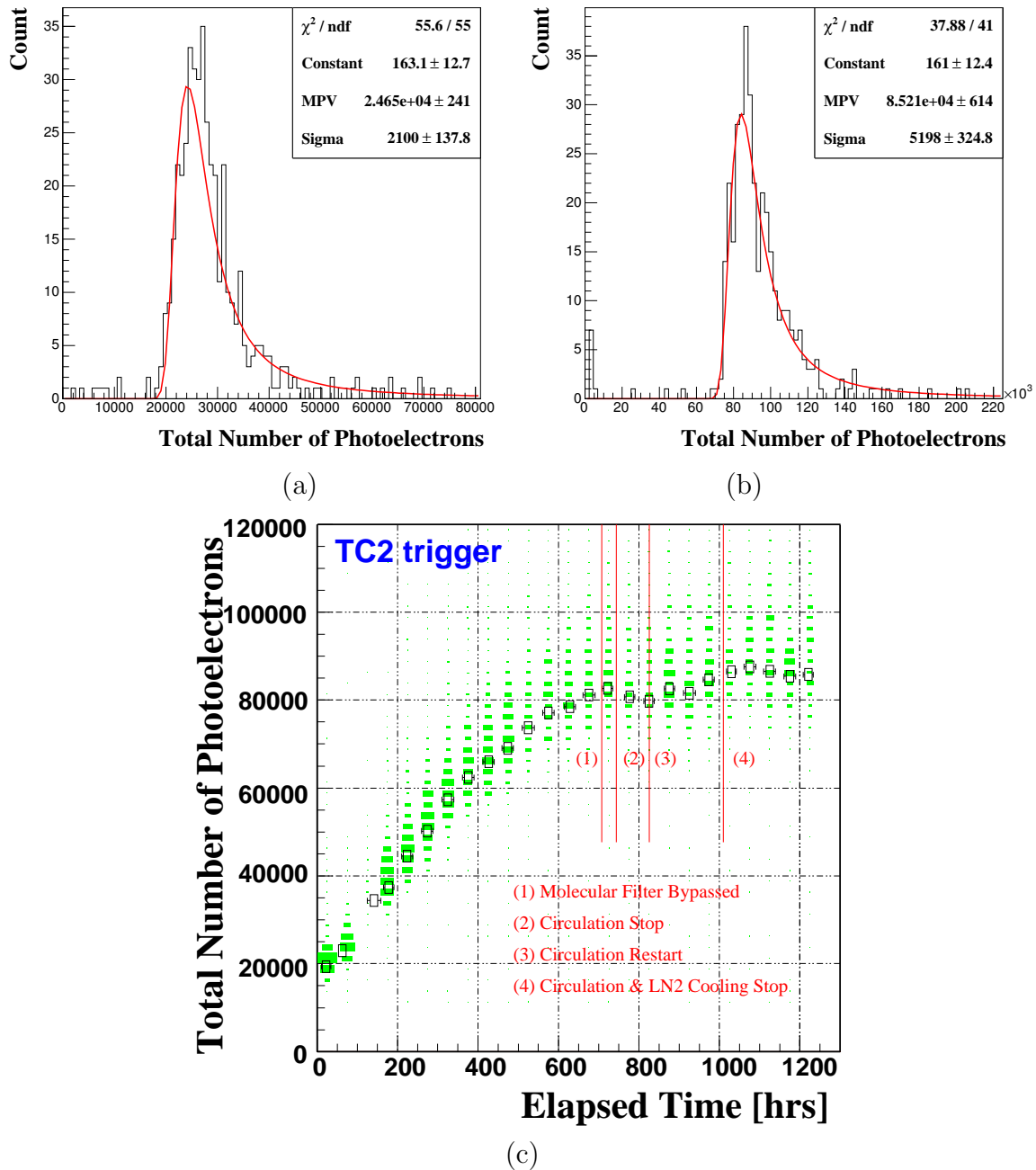


Figure 4.4: (a) A number of photoelectrons before the purification and (b) after the purification (c) Light yield transition for cosmic-ray muon events. The deposit energy for minimum ionizing particles (MIP) is approximately 155 MeV from the MC simulation.

We first made a crude estimate of the Rayleigh scattering length by using the PMTs

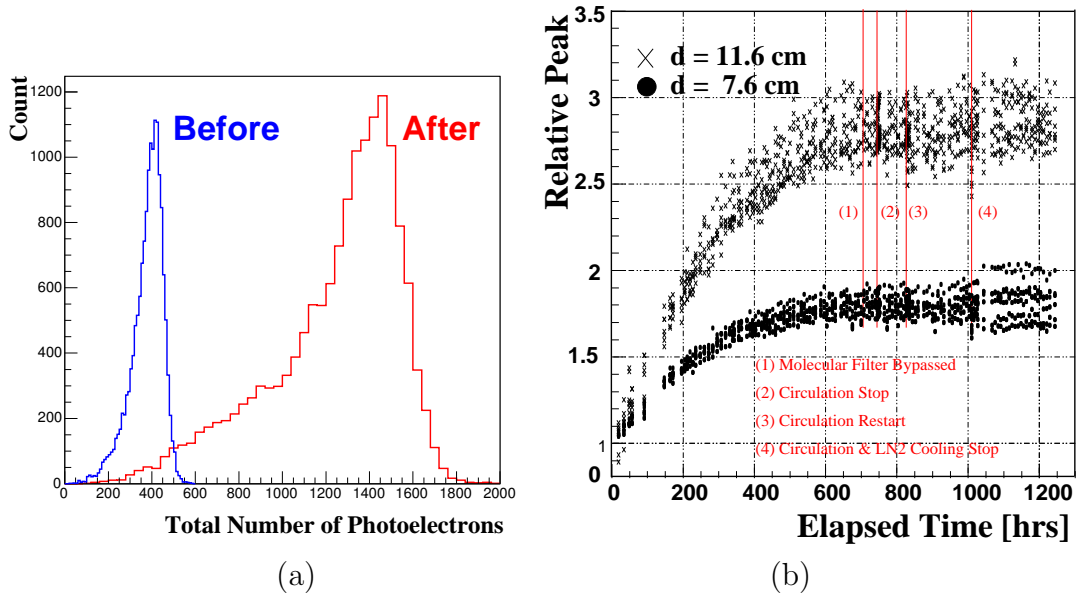


Figure 4.5: (a) Total N_{pe} before and after the circulation. (b) Light yield transition for α particle events, observed by one PMT.

located on the same face as the α source; these PMTs can not directly see the scintillation light from the α particles but only the scattered light. Although ambiguities in reflection of scintillation photons on the walls do not allow a more accurate estimate, our data prefer values of $\lambda_{Ray} = 40 - 50$ cm, which are consistent with the numbers currently available in the literature [53, 56–58, 73].

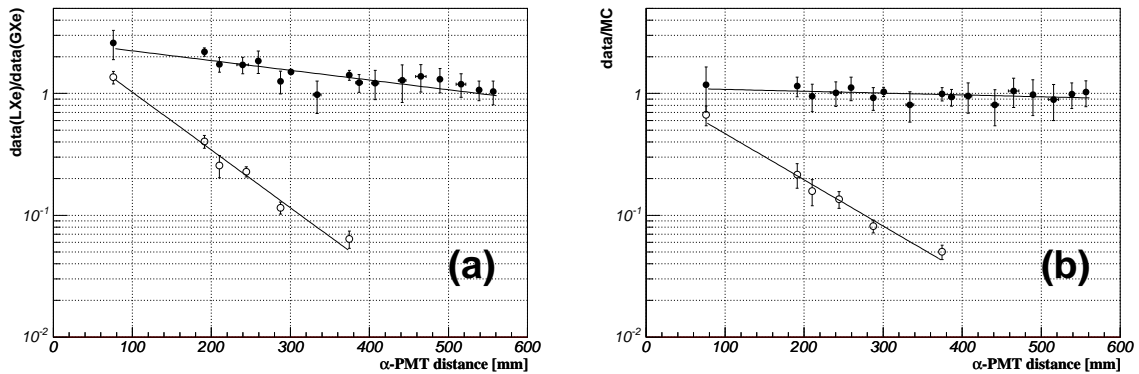


Figure 4.6: The PMT outputs normalized either to those in the GXe data (a) or to the MC simulation without absorption (b) are plotted as a function of the source-PMT distance at the beginning (open circle) and after purification (closed circle). The solid lines are fitted results.

To evaluate the absorption length λ_{abs} , we compared the PMT outputs in the LXe to those in the GXe and to a Monte Carlo simulation with no absorption and a variable λ_{Ray} . Note that both absorption and scattering are negligible in the GXe. In Fig. 4.6 the PMT outputs normalized either to those in the GXe (a) or to the MC simulation with

$\lambda_{\text{Ray}} = 45$ cm (b) are plotted against the source-PMT distance. Here the distributions at the beginning of purification (open circles) and after one month of purification (closed circles) are compared. The evident exponential decline at the beginning almost vanished after purification. Note that the slopes are steeper in the GXe normalized plots because they also contain the effect of scattering which is not canceled by normalizing to the GXe data.

These distributions were then fitted with exponential functions. From the comparison with the GXe data an effective attenuation length of 54_{-9}^{+14} cm was obtained after the purification. This effective length contains the effects of both the absorption and the Rayleigh scattering. Since the scattered photons are not totally lost but may be detected by other PMTs, the obtained effective attenuation length is longer than λ_{att} and, especially if $\lambda_{\text{abs}} \gg \lambda_{\text{Ray}}$, it is longer than λ_{Ray} . Note that the LXe/GXe ratio is larger than unity since the ratio of the scintillation yields in LXe and GXe is approximately 2.7 [83].

The comparison with the simulation does not show a significant slope. We used this result to establish a lower limit on the absorption length λ_{abs} of 91 cm at 90% confidence level or 80 cm at 95% confidence level, where λ_{Ray} was varied from 30 cm to 50 cm in the simulation. Before the purification λ_{abs} was 12.0 ± 1.8 cm. We conclude that the level of water content after the purification was much lower than 100 ppb.

After successful purification of LXe under the operational conditions, efforts have been focused on reducing the initial amount of water contamination in the vessel. We replaced most of the acrylic parts with Teflon to suppress out-gassing in the inner chamber, which resulted in an initial absorption length λ_{abs} of 30 cm in the subsequent operation. A lower limit on the absorption length λ_{abs} of 100 cm at 90% confidence level was then achieved in a much shorter time of xenon purification, in about 300 hours.

We are also developing a liquid-phase purification system with a fluid pump to increase the purification efficiency. In such a system the circulation speed could be increased up to 100 ℓ /hour of LXe, more than 1000 times faster than the current system.

Chapter 5

Performance of the 100-liter Prototype

5.1 Motivation

The γ -ray energy from the $\mu \rightarrow e\gamma$ decay is just 52.8 MeV, whereas energy of γ rays of backgrounds in MEG experiment, for instance γ rays from the Michel decay, is never more than 52.8 MeV. Therefore the LXe detector should have an excellent energy resolution in the energy region of around 50 MeV. Moreover, good energy, position, and time resolutions are required in order to recognize pile-up events of accidental backgrounds.

In order to verify the performance of the LXe detector, a beam test was carried out with the 100-liter prototype by using γ -ray beam up to 40 MeV from a laser Compton scattering (LCS) facility. Based on the obtained result we can estimate the expected performance of the final LXe detector to be used in the MEG experiment. It is also quite important to develop Monte Carlo simulation by using measured data with a simple configuration of PMTs, as employed in the 100-liter prototype, compared to the final detector. Furthermore it is also possible to mimic the PMT configuration of the final detector, curved C-shape geometry, by masking whole PMTs on certain plane of the detector. Estimating the efficiency and evaluating how the detector performance deteriorates when we place additional material, in front of the entrance window, with equivalent thickness to that of the COBRA magnet is another issue to be examined in this test. These provide essential information to the design work of the final LXe detector.

It must be mentioned that another kind of beam test was performed later on this work by using γ rays from π^0 decays produced in the charge exchange process ($\pi^- + p \rightarrow \pi^0 + n$) and from the radiative capture process ($\pi^- + p \rightarrow \gamma + n$). In this test it is possible to evaluate the detector energy resolution by using almost monochromatic γ rays up to 129 MeV while in LCS beam the resolution has to be evaluated by the shape of the sharp edge of γ -ray spectrum below 40 MeV. Nevertheless conducting the test by using the LCS beam is significant because the detector can be radiated with pure γ -ray beam with reasonable intensity necessary to evaluate position resolution with a collimator. Note that thanks to the beam purity it is not necessary to consider the effect of possible background sources like slow neutrons.

In this thesis the result from the π^0 beam test is not mentioned in detail. All performance evaluation and consideration on the final detector performance rely on the results obtained in the LCS beam test.

5.2 Laser Compton Scattering beam test at AIST

For evaluating the performance of the LXe detector, a beam test was performed in April 2004 by using γ rays from laser Compton scattering (LCS) provided at the electron storage ring, TERAS, at National Institute of Advanced Industrial Science and Technology (AIST) in Tsukuba, Japan. Fig. 5.1 shows a schematic view of TERAS. In the TERAS facility, there are several beam lines to provide synchrotron radiation light and soft X-ray. Among these there is a beam line, shown as LCS-1 in the figure, where high energy γ -ray beam can be delivered.

In the TERAS facility electron acceleration and storage is done in the following way. Electron beam of 310 MeV provided from a linear accelerator is injected into TERAS up to 30 to 250 mA. Then injection is terminated and stored electrons in the ring are started to be accelerated to ~ 800 MeV by RF powers. When electron energy reaches a target value, the operation mode is switched from acceleration mode to storage mode. It is possible to store electrons stably with a life time of 8 hours in normal operating condition. Electron injection into TERAS is usually performed twice a day. The ring parameters for TERAS are summarized in Tab. 5.1. Electron energy in TERAS was set to be 764 MeV in this test.

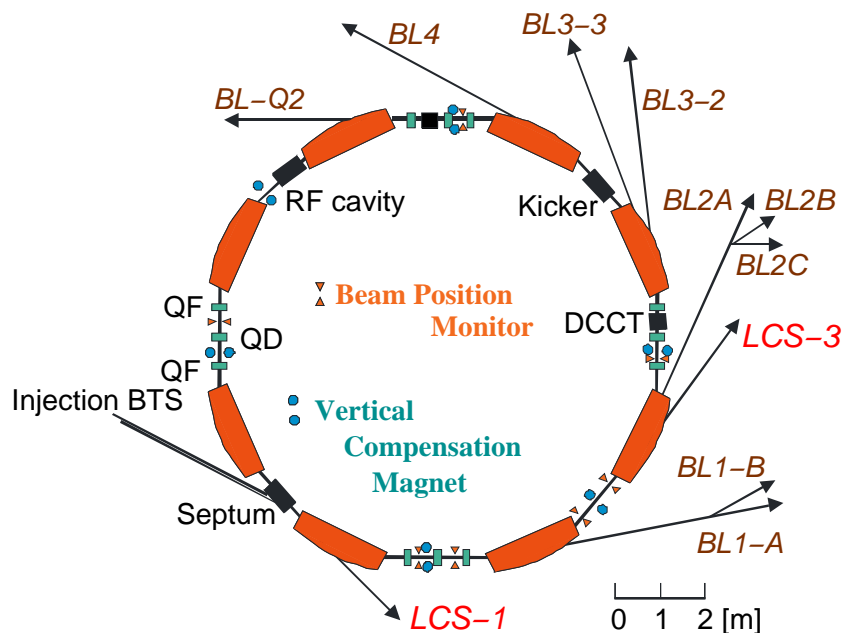


Figure 5.1: Schematic view of TERAS.

In the LCS-1 beam line laser photons are generated by Nd:YAG pulse laser. Its fundamental wavelength is 1064 nm and it can be converted to the second harmonic of 532 nm and the fourth harmonic of 266 nm for providing higher energy γ -ray beams. The laser photons are guided to the collision point in the TERAS ring by a half-mirror and collide head-on with electrons. Through Compton scattering on an electron, a laser photon receives most part of the electron energy and boosted back in the direction of initial electron beam. The energy of the LCS γ rays can be set up to 40 MeV by changing the laser wavelength and/or the electron energy in TERAS. The properties of laser and

Table 5.1: Ring parameter and laser properties for LCS beam.

Storage ring	Circumference	31.45 m
	Bending radius	2.0 m
	RF frequency	171.682 MHz
	Max. stored current	350 mA
	Energy range	200 MeV to 800 MeV
	Energy in this test	764 MeV
	Energy spread (σ)	0.48% (3.7 MeV)
	Typ. storage time	8 hours for 100 mA
	Angular divergence (σ)	0.115 mrad
	Horizontal bunch size (σ)	1.55 mm to 2.2 mm
Vertical bunch size (σ)	1.0 mm	
Laser photon	Lasing wavelength	266 nm, 532 nm, 1064 nm
	Energy spread (FWHM)	0.002%
	Angular divergence (σ)	0.5 mrad
	Beam size	unknown
Compton edge energy		10.32±0.10 MeV
(Error in σ)		20.37±0.20 MeV
		39.67±0.38 MeV

the LCS beam are also shown in Table 5.1. Fig. 5.2 shows a picture of the experimental setup around the collision point.

It must be remarked that the LCS beam is not monochromatic but has an energy spread determined by the scattering angle of photons (and by relative angle between the laser photon and electron before collision). The energy spectrum of the LCS γ rays $F(E_\gamma)$ can be approximately written as [84]:

$$F(E_\gamma) = N \left\{ \left(E_\gamma - \frac{E_C}{2} \right)^2 + \frac{E_C^2}{4} \right\}, \quad (5.1)$$

where N is the normalization factor and E_γ is the γ -ray energy. This expression can be a good approximation if the energy of Compton edge E_C is much smaller than the electron energy. The E_C is determined by the energy of laser photon E_l as

$$E_C = \frac{4\gamma^2 E_l}{1 + \frac{4\gamma E_l}{m_e}}, \quad (5.2)$$

where γ is the relativistic factor of the incoming electron and m_e is the electron rest mass.

In this test, in order to define the incident spot on the detector and to select the γ -ray energy two collimators were placed between the collision point and the LXe detector as shown in Fig.5.3. They also served for excluding low energy γ rays from synchrotron radiation that cannot be eliminated completely since the scattering point is set in a bending section in the ring. The effect of the collimator on the incident γ -ray spectrum is estimated by a simple Monte Carlo simulation as shown in Fig. 5.4. It can be seen that

by placing a smaller size collimator in front of the detector the spectrum given in Eq. 5.1 becomes narrower while the sharp Compton edge remains. In this thesis, the data with the 1-mm ϕ collimator was used for analysis because no differences between results with 1-mm ϕ and 2-mm ϕ collimators were seen.

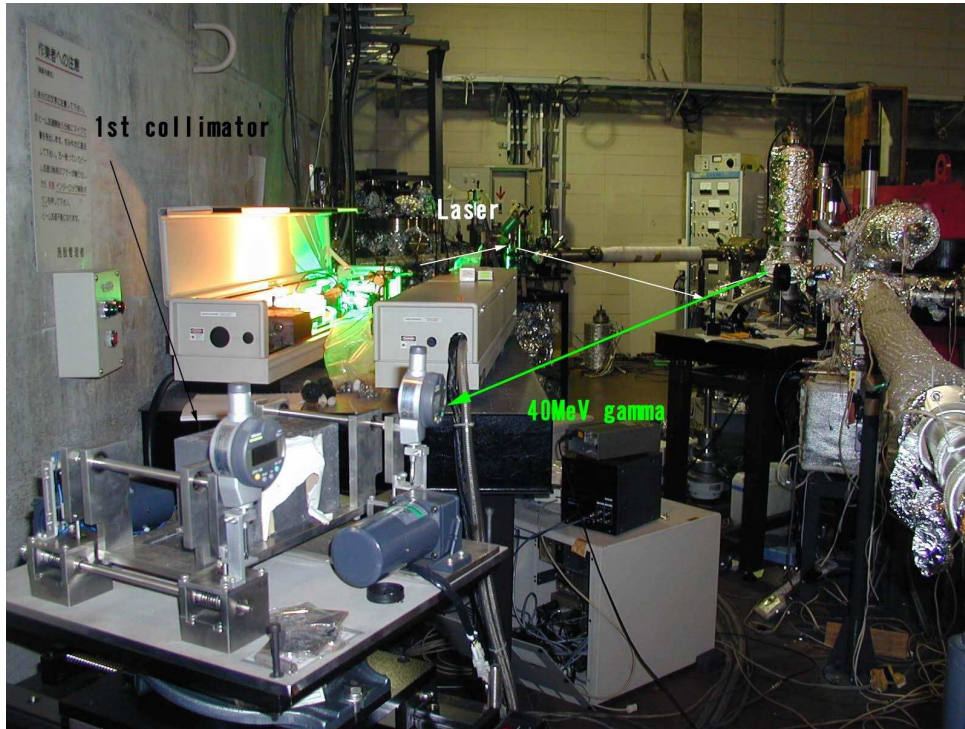


Figure 5.2: Setup for LCS beam. When the laser is green (532 nm), the energy of LCS γ rays is 20 MeV.

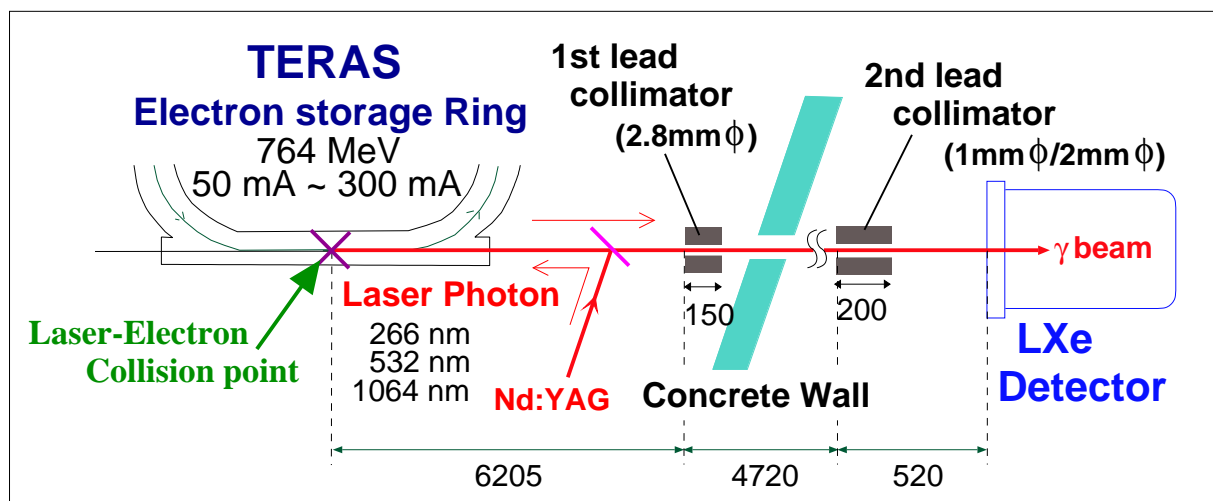


Figure 5.3: Experimental setup in TERAS beam test.

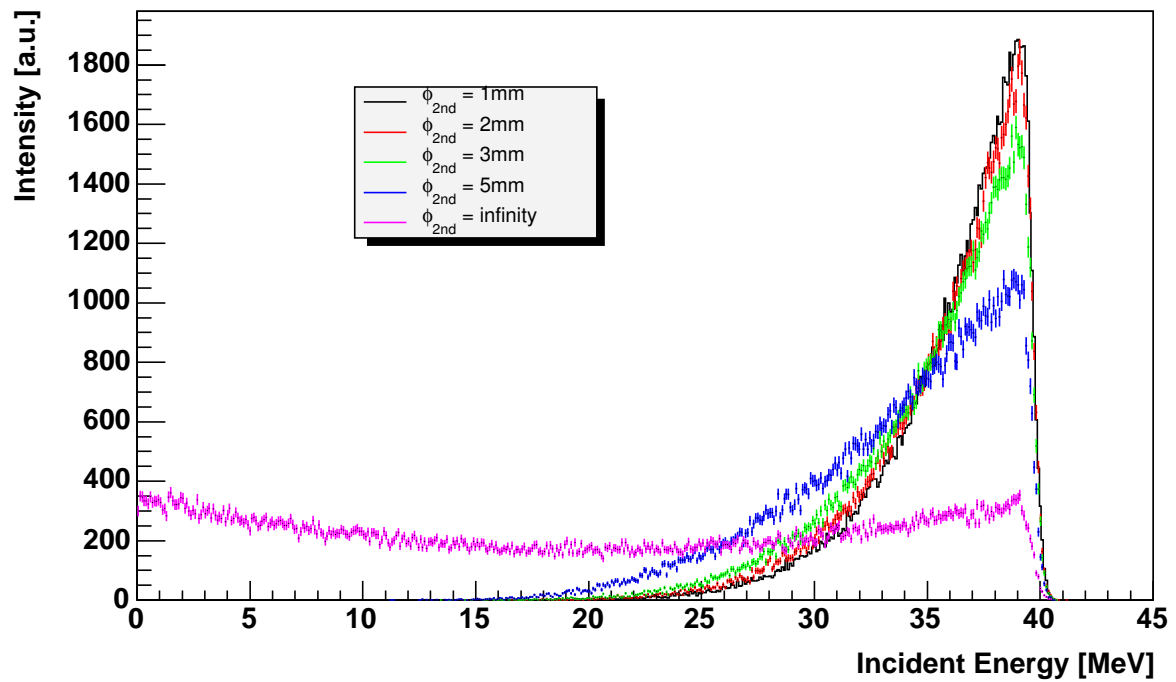


Figure 5.4: Energy spectra depending on the diameter size of the 2nd collimator. Beam and laser properties listed in Table 5.1 are taken into account in this calculation.

5.3 Trigger and Data Acquisition

The data flow in the data acquisition is shown in Fig. 5.6. There were two groups of PMT signals. The one is composed of signals from 128 PMTs located around the front face of the detector. These PMT signals are recorded both in ADC and TDC. The other consists of signals from remaining 100 PMTs located rather back in the PMT supporting holder. These PMT signals are recorded only in ADC. Signals from the 128 PMTs were also utilized to provide trigger information for the acquisition system. Signal splitters were prepared to split PMT signals to ADC and discriminators. Discriminator output was utilized both for TDC input and trigger decision. The splitter is custom made for the MACRO experiment and possible to pass analog signal with a bandwidth of 100MHz. The threshold level for each channel in discriminators was set to be minimum, that is, -10 mV which is the minimum level in the discriminator. This discriminator module can provide information about the number of hit channels (N_{hit}) above the threshold. In the trigger system another parameter N_{discr} was implemented. If N_{hit} of one discriminator is 2 or more, the N_{discr} is incremented, enabling us to count the number of fired PMT cluster. Cluster definition is illustrated in Fig. 5.6.

The TDC was operated in the common start mode. Timing jitter of the PMT signals relative to the trigger start timing was typically 50 nsec, which could be handled with the electronics time window without any significant problem.

Signals to ADC module were fed through 210-nsec cable delay so as to be entirely included in 600-nsec ADC gate. The width of ADC gate was set to be 600 nsec in every run mode to contain all signals fully. We prepared four kinds of trigger logics to deal various event types.

Pedestal and LED Run: In both run modes, the trigger is generated by NIM clock generator at the rate of 100 Hz. Only when the run mode was LED (light-emitting diode) mode, the LED driver (CAEN C529, [85]) fed driving pulses to LEDs. In this test, it was repeated several times a day for investigating the pedestal noise and stability of gain adjustment.

LCS γ -ray Run: This trigger mode was activated by the coincidence between a trigger from PMT outputs and a trigger from pulse laser. It allowed to veto the other sources such as α -particle, cosmic-ray, and environmental backgrounds. The threshold of N_{hit} was set to 2.

α -particle Run: The α sources was installed on each lateral face as shown in Fig. 5.5. Since the light yield from α particles is not high, α -particle event fires mainly the nearest cluster alone. When N_{hit} was 1, nearly 100% of those events was from α particle.

Cosmic-ray Muon Run: As shown in Fig. 3.5, three pairs of counters were set below and over the LXe detector. Since trigger rate was very low (about 0.01 Hz), cosmic-ray trigger was usually mixed with γ -ray trigger.

The data acquisition system consisted of mainly FASTBUS and partially CAMAC standards. Due to the slow communication to the CAMAC system the data taking rate

was less than 200 Hz. The data acquisition system was driven by an online/offline software package, MIDAS [66]. The MIDAS system managed also the slow control system including all kinds of control and status monitoring such as xenon and purification system with help of LabVIEW [67].

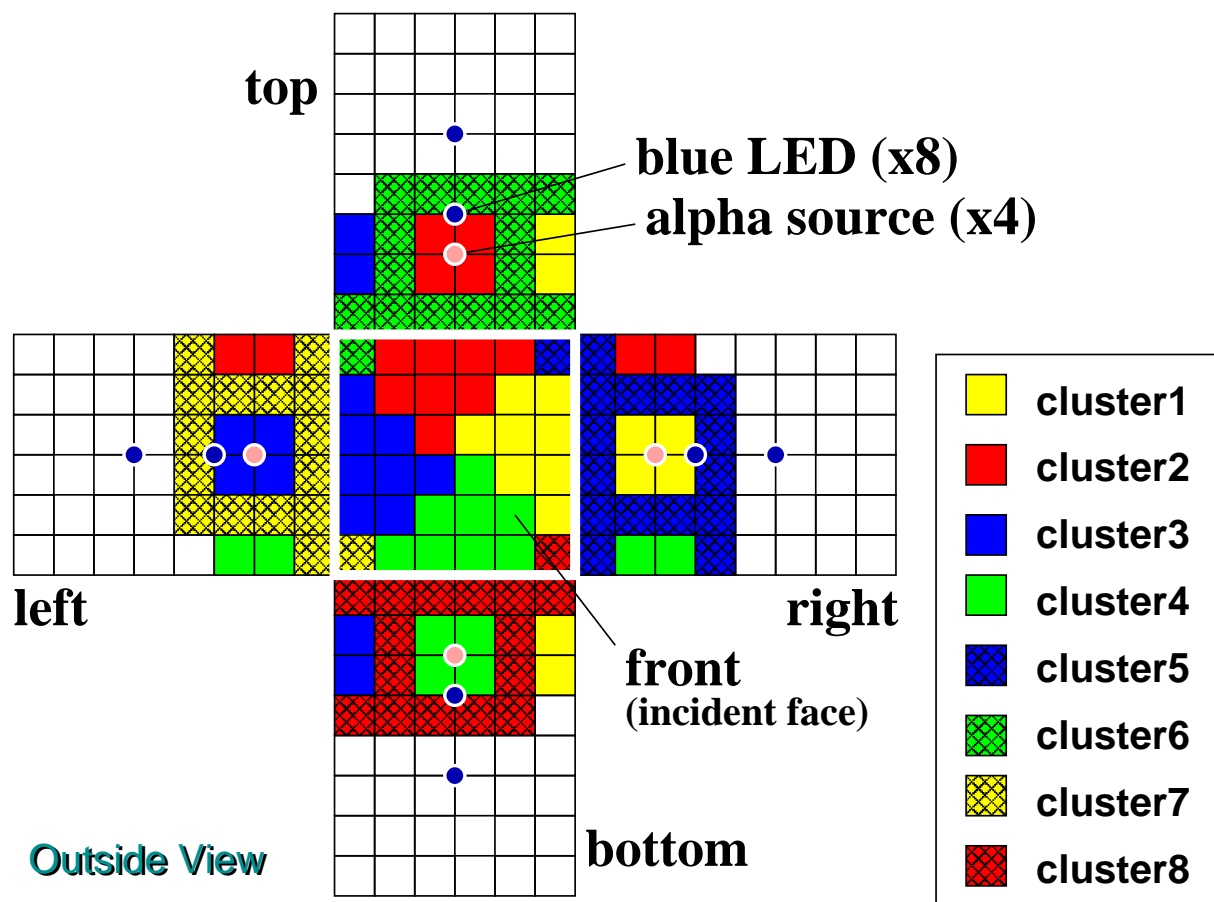


Figure 5.5: The clusters for generating trigger.

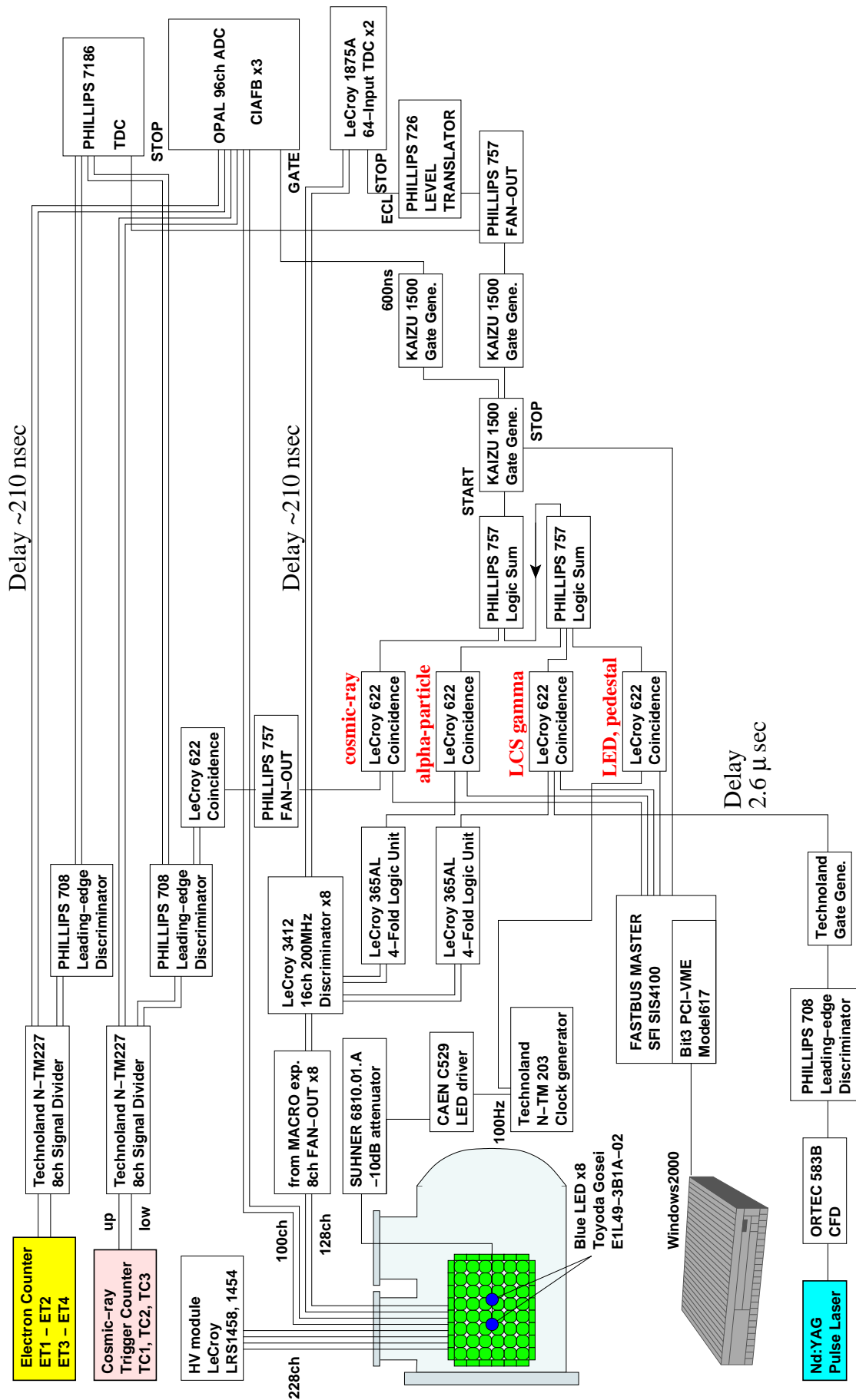


Figure 5.6: Data flow diagram in LCS beam test.

5.4 PMT Calibration

A precise knowledge of PMT gains and quantum efficiency (QE) is necessary for reaching an excellent energy resolution and reconstruction accuracy of the first conversion point in LXe.

The LXe detector is equipped with eight LEDs (two on each lateral face) to measure gains of each PMT and four ^{241}Am α sources (one on each lateral face) to measure QEs as described in Chapter 3. Gain adjustment is for converting ADC count to the number of photoelectrons (N_{pe}) and QE values of each PMTs are necessary for converting N_{pe} to the number of photons (N_{ph}) and, in particular, for position reconstruction.

5.4.1 Gain Adjustment

Method

PMT gains were adjusted to 1×10^6 in LXe (165 K and 1.3 atm). Blue LEDs [86] were used to adjust and monitor PMT gains. A pair of LEDs facing each other on the lateral detector side was flashed at 100 Hz by the LED driver. The gain for each PMT was set to 1×10^6 . During data acquisition over two weeks all the gains were monitored several times a day.

Since R6041Q is not good at single photon separation owing to its dynode structure, the strategy of the gain adjustment is to observe plenty of photons and estimate PMT gains from statistical fluctuation of them. In references of [87–89], the difficulty of single photon separation and the way to adjust gains with multi-photons from LEDs are detailed.

Our model is simple. We assume that LED output is constant and the statistics of N_{pe} obeys Poisson distribution. Some of those photons reach the quartz window of a PMT and transmit it, and photoelectrons are generated by photoelectric effect with a certain efficiency (QE), and hit the first dynode with a collection efficiency (CE). Both obey binomial distribution. Then the photoelectrons are amplified by dynodes.

The distribution of N_{pe} becomes a convolution of binomial distributions and Poisson distribution. In that case, the upper tail is broader than lower tail. When N_{pe} is large enough (10 photoelectrons at least), the contribution of binomial distribution is negligible. Therefore the spectrum after amplification can be Poisson distribution scaled by gain. The gain can be given by the following equation:

$$g = \frac{c\sigma^2}{eM}, \quad (5.3)$$

where g is the gain, c is the ADC least count (200 fC/ch), σ and M are the standard deviation and the mean of ADC spectrum fitted with a Gaussian, respectively, and e is the elementary electric charge, assuming that the number of photoelectrons (N_{pe}) observed on a PMT is so large that the ADC spectrum can be regarded as a Gaussian. In practice we have to consider a contribution from the deviation of pedestal to it as the following equation:

$$\sigma^2 = g\frac{e}{c}(M - M_0) + \sigma_0^2, \quad (5.4)$$

where M_0 and σ_0 are the mean and the standard deviation of the pedestal spectrum, respectively. The gain estimate becomes more reliable by using this equation. By changing the intensity of the LED the PMT outputs vary as shown in Fig. 5.7 (a). Fig. 5.7 (b) shows an example of the linear relation between σ^2 and M . The gain of the PMT is evaluated by fitting the relation with Eq. 5.4. Thus the precision of gain determination can improve by using data for various yield of photons.

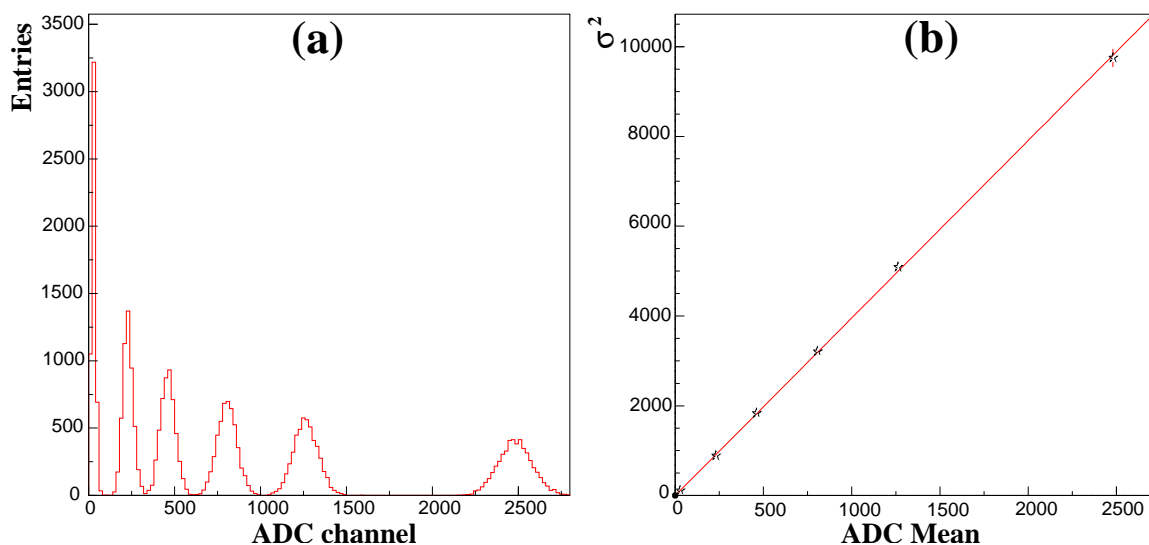


Figure 5.7: (a) ADC spectra of a typical PMT in the gain adjustment. (b) The relation between σ^2 s and the mean channels from (a), where σ^2 at ADC Mean = 0 corresponds with the variance of the pedestal σ_0^2 . In both figures the pedestal mean is already subtracted from the ADC spectrum.

As shown in Fig. 5.8, after a few iteration of gain adjustment, the spread of all the gains became approximately 3% in sigma. This was limited by the minimum controllable digit of the HV power supply. It is not so important to set them to the same gain. It is essential to determine the gains and keep them stable. Estimation of gain measurement and monitoring accuracy will be discussed in the following.

Accuracy of the Method

As described above, this method requires stable light source. If the LED was unstable and its stability was worse than the random noise amplitude, the linearity in Eq. 5.4 would be lost. Fig. 5.7, however, shows that the linearity is conserved during measurement.

The same pair of LEDs was always used out of 8 LEDs for calibration. In order to check the difference of the gain determination with the other pairs of LEDs, they were flushed and the same procedure was repeated for each of them. Fig. 5.9 shows a relation between σ^2 and ADC mean value for one PMT obtained by flushing different pairs of LEDs. It can be seen that all points stay on a line, indicating that there is no difference between selected pairs.

The LED calibration procedure was checked more systematically both by using different LED pairs and by using the same pair for several consecutive runs. It was found that the gain determination can be reproduced within an accuracy of 0.4% in sigma.

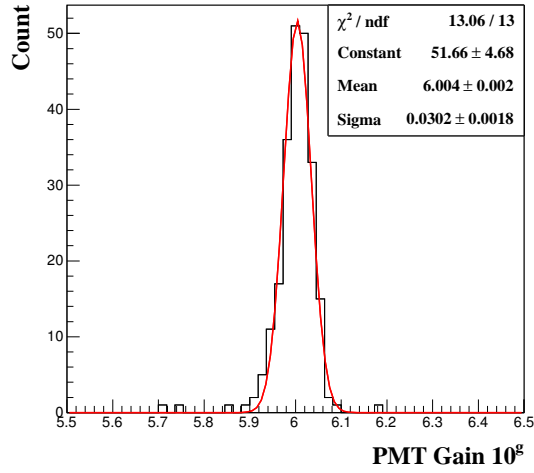


Figure 5.8: Gain distribution of 228 PMTs.

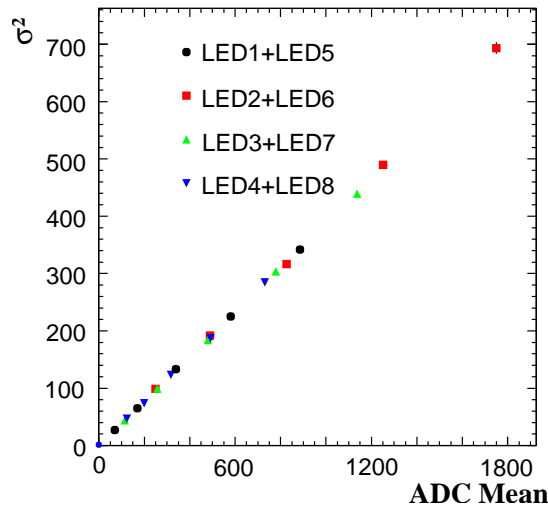


Figure 5.9: The relation between ADC mean and variance for 4 pairs of LEDs.

The stability of the gain adjustment for a particular LED pair was also checked by comparing two consecutive runs, flashing the same LED pair. The ratio of the gain obtained in two runs for each PMT was taken. Distribution of the ratios for all PMTs is shown in Fig. 5.10(a). It can be seen that the standard deviation is 1.6%. Since the PMT gain is not probable to change in such short period, this can be regarded as reproducibility of the procedure.

The long-term stability was also investigated as seen in Fig. 5.10(b). The data was taken for about one month in another period of detector operation than the LCS beam test. The gain variation is found to stay within 0.5% in sigma.

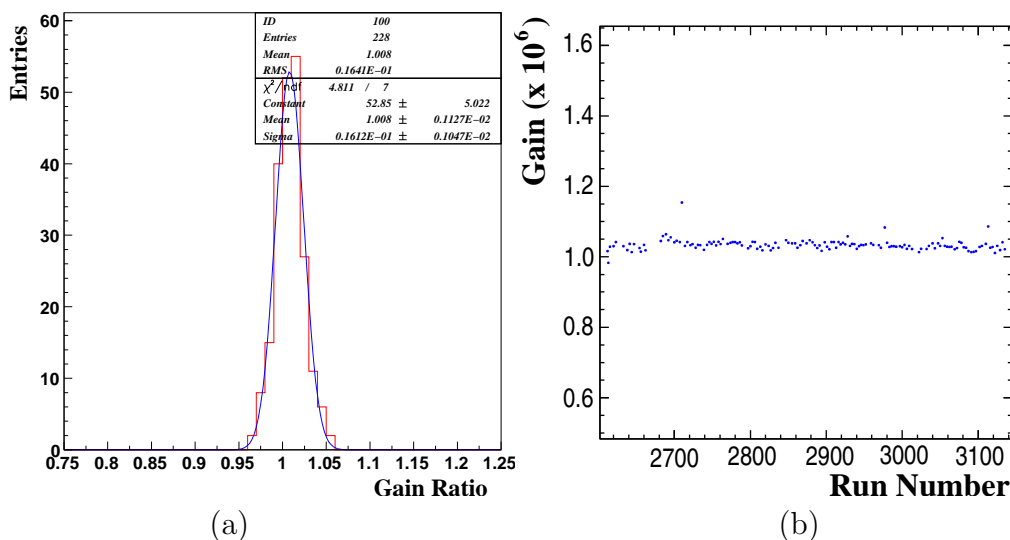


Figure 5.10: Short-term and long-term stability. (a) Ratio of the gain obtained in two consecutive runs. Ratio of the gain obtained in two consecutive runs. (b) Long-term stability of gain adjustment for a PMT.

5.4.2 QE Measurement

We must use same wavelength of light as Xe scintillation light for estimating QEs since QEs highly depends on the wavelength. This is why LEDs are inappropriate as a light source for QE estimation. For that purpose α particle is the most appropriate as the light source. Alpha-ray from ^{241}Am has an almost monochromatic energy spectrum (5.443 MeV (83%) and 5.443 MeV (15%)) with lower tail caused by energy loss in the source material itself and its range in liquid xenon is beneficially short as 40 μm . In addition it is very stable even at low temperature in LXe. The half life of ^{241}Am is long enough that the source intensity can be regarded to be constant. Therefore the α source is a good point-like light source for estimating QEs.

There are two possibilities to estimate QEs at low temperature around operating condition. One is to utilize cold gas xenon (GXe) and the other is just to measure the QEs during operation i.e. in LXe. In GXe effects of scattering and absorption of scintillation light is negligibly small while in LXe they are prominent. We tried both methods in this analysis.

We took α -particle data in such a condition that the inner vessel is filled with 1.3-atm cold (170 K) GXe, whose scintillation spectrum is not so much different with that in liquid phase [90, 91]. The data was compared with a Monte Carlo simulation. In this simulation, the scintillation efficiency (energy deposit required to emit one scintillation photon, $W_{\text{ph}}(\alpha)$) of GXe was assumed to be 49.6 eV and the absorption and Rayleigh scattering were switched off. As shown in Fig. 5.11, QE of each PMT was estimated by comparing the measured spectrum to the one obtained in the simulation.

We took α -particle data in LXe also. Similarly as in GXe, QE of each PMT was estimated, assuming $W_{\text{ph}}(\alpha)$ to be 17.6 eV, absorption length to be 1 m, and Rayleigh scattering length to be 45 cm. The QE distribution obtained by GXe data and LXe data are compared in Fig. 5.12. Clear relation between two estimation methods can be seen

although the absolute value is different. This is most probably caused by ambiguity of $W_{\text{ph}}(\alpha)$ in LXe and GXe. Although GXe data is easier to handle for avoiding problems of the absorption and scattering, we employed the LXe data for QE estimation because scintillation light yield is higher in LXe than in GXe and temperature uniformity in the cryostat is better in LXe than in GXe. Note that the newly installed purification system enabled us to do in this way. It had been impossible to estimate QEs in LXe before we succeeded in purifying xenon on site.

Fig. 5.12(b) shows the QE distribution estimated by using LXe data. The lower tail is attributed to the uncontrolled thickness of Mn-layer on the photo-cathode and to the inappropriate mixture of photo-cathode material resulting in resistivity increase at LXe temperature. The broad distribution is due to difficult evaporation technique for the photo-cathode material.

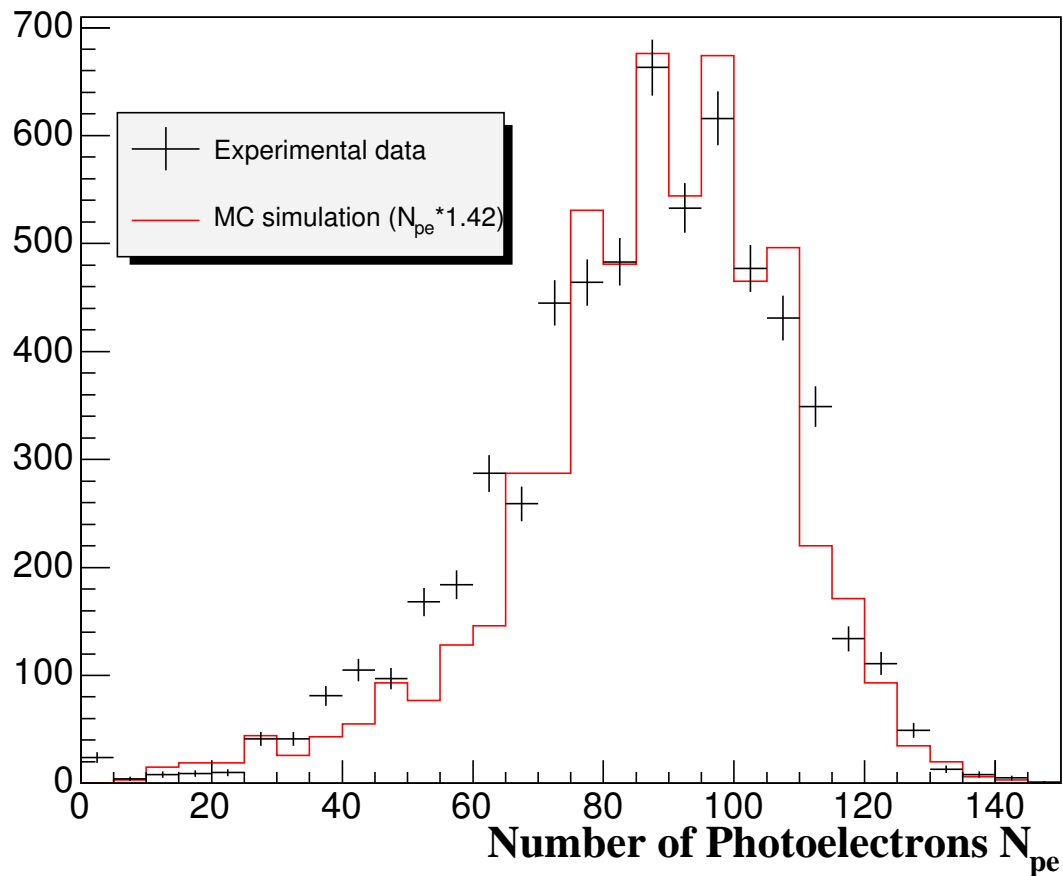
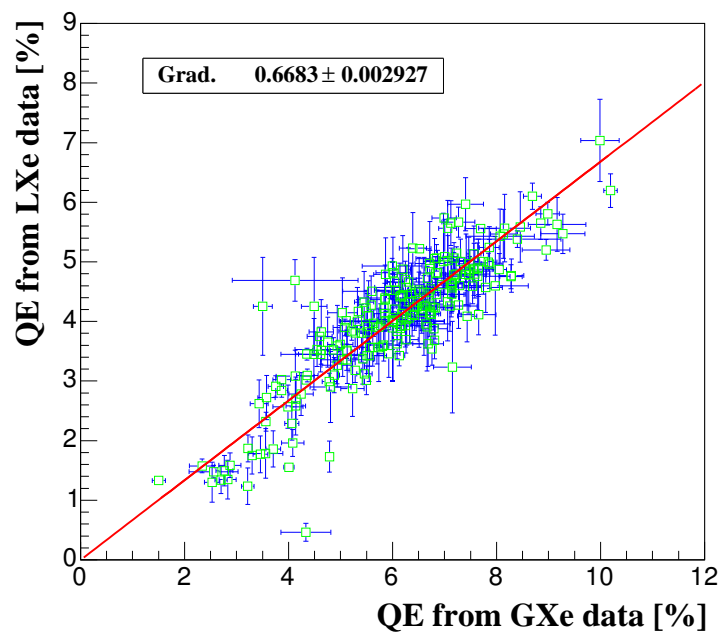
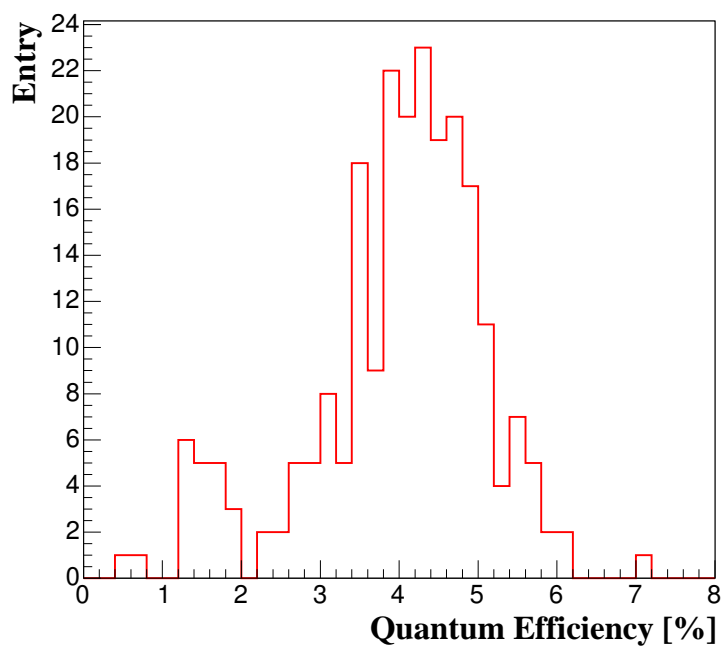


Figure 5.11: The N_{pe} spectra observed by a PMT for α particle in LXe. The ratio of experimental data to the simulation data was about 1.4.



(a)



(b)

Figure 5.12: (a) QE estimated from GXe and LXe data. (b) Distribution of QE estimated from LXe data.

5.4.3 Long-term Stability

The α -particle data in LXe are used for monitoring stability of the PMT outputs since they are regarded as stable light sources. Fig. 5.13 shows that the PMT outputs stabilized within 5%. This fluctuation includes the error of gain determination. The fluctuation of the raw ADC data is less than 5%. Normally PMT output is unstable and high gain just after completing liquefaction of xenon. As shown in Fig. 5.13 (b), the total N_{pe} was decreasing in the early days. It took about 2 days for PMTs to be stable. After that, the light yield was gradually increased by purification of LXe. If the effect of purification was taken into account, the total N_{pe} was able to be stable within 3%.

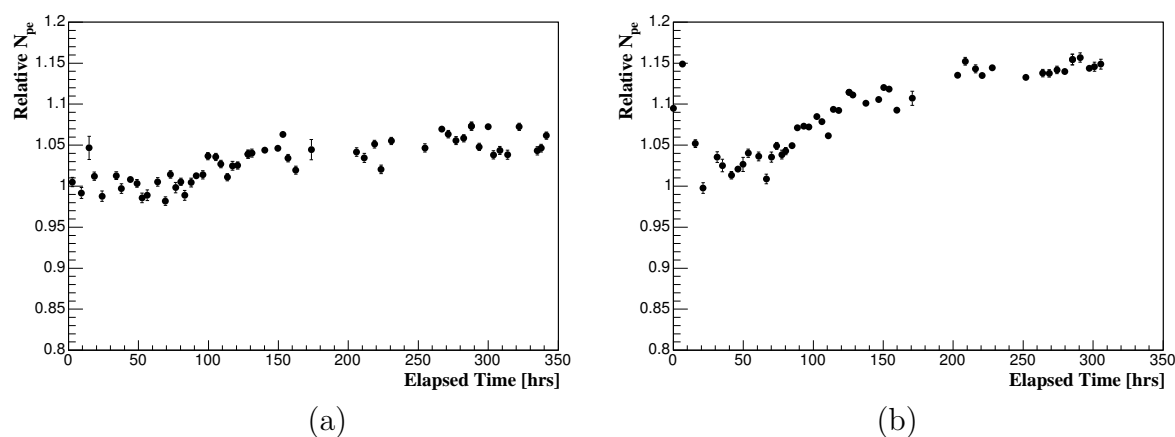


Figure 5.13: Long-term stability in α runs over the beam test for (a) N_{pe} observed by a PMT and (b) a sum of N_{pe} s by all PMTs. Elapsed time of zero corresponds to the beginning time of the test.

5.4.4 Noise Estimate

As in any electronics system, noise is an important concern in the detector performance. A typical distribution of the pedestal data is shown in Fig. 5.14(a). The distribution of the pedestal after summing all 228 channels are shown in Fig 5.14(b). The width of the pedestal distribution corresponds to the electronics noise level.

The noise is comprised of both incoherent and coherent noise:

$$\sigma_T^2 = \sigma_I^2 + \sigma_C^2, \quad (5.5)$$

where σ_T^2 stands for the total noise, σ_I^2 the incoherent noise, and σ_C^2 the coherent noise. The incoherent noise can be thought of as random, whereas the coherent noise can be thought of as noise correlated between PMTs and channels in the ADC module. The incoherent noise is defined as

$$\sigma_I^2 = \sum_{i=1}^n \sigma_j^2, \quad (5.6)$$

$$\sigma_i^2 = \frac{1}{N} \sum_{j=1}^N (q_{ij} - \bar{q}_i)^2 - \left\{ \frac{1}{N} \sum_{j=1}^N (q_{ij} - \bar{q}_i) \right\}^2, \quad (5.7)$$

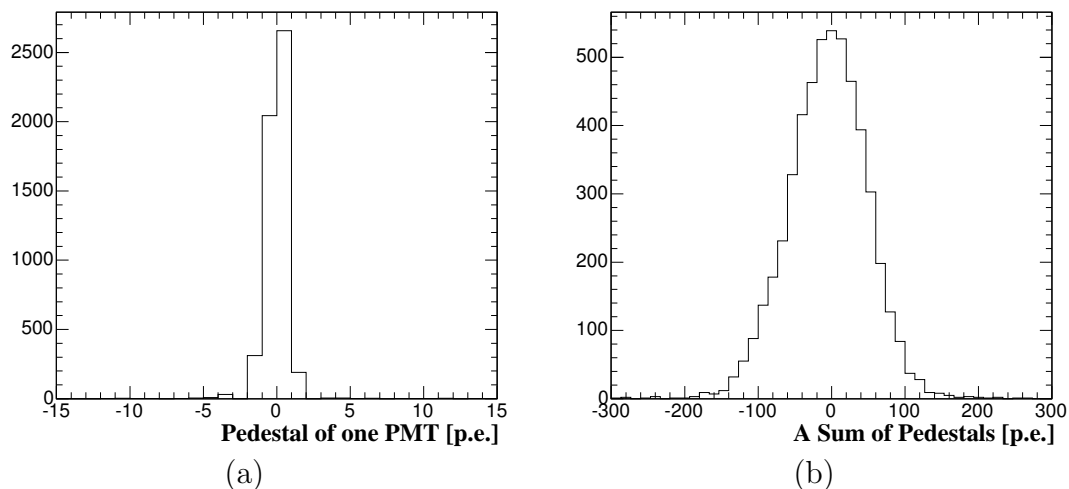


Figure 5.14: Typical pedestal distribution of one channel (a) and a sum of 228 channels (b) after converting ADC channel to number of photoelectrons.

where \bar{q}_i is the average of ADC count(q_{ij}) of j -th PMT over N events in the pedestal run. The coherent and incoherent noise calculated by using these equations are summarized in Tab.5.2

Table 5.2: Typical overall noise results.

Noise	ADC count	converted to N_{pe}
σ_T	37.4	53.6
σ_I	31.7	46.5
σ_C	19.7	26.7

5.5 Incident Beam

In order to estimate the detector performance for γ rays of tens of MeV, the scale of the incident beam energy were 10 MeV, 20 MeV, and 40 MeV at Compton edge.

Moreover, we studied the position dependence of the detector performance by moving the detector with respect to the beam. The impinging points are shown in Fig. 5.15. The point P0 corresponded to the center of the impinging (front) face. The point P9 was shifted from the center of the PMT by +2 mm along x axis to avoid the edge of the entrance window of the cryostat. In this analysis the data from P1 to P8 was not used.

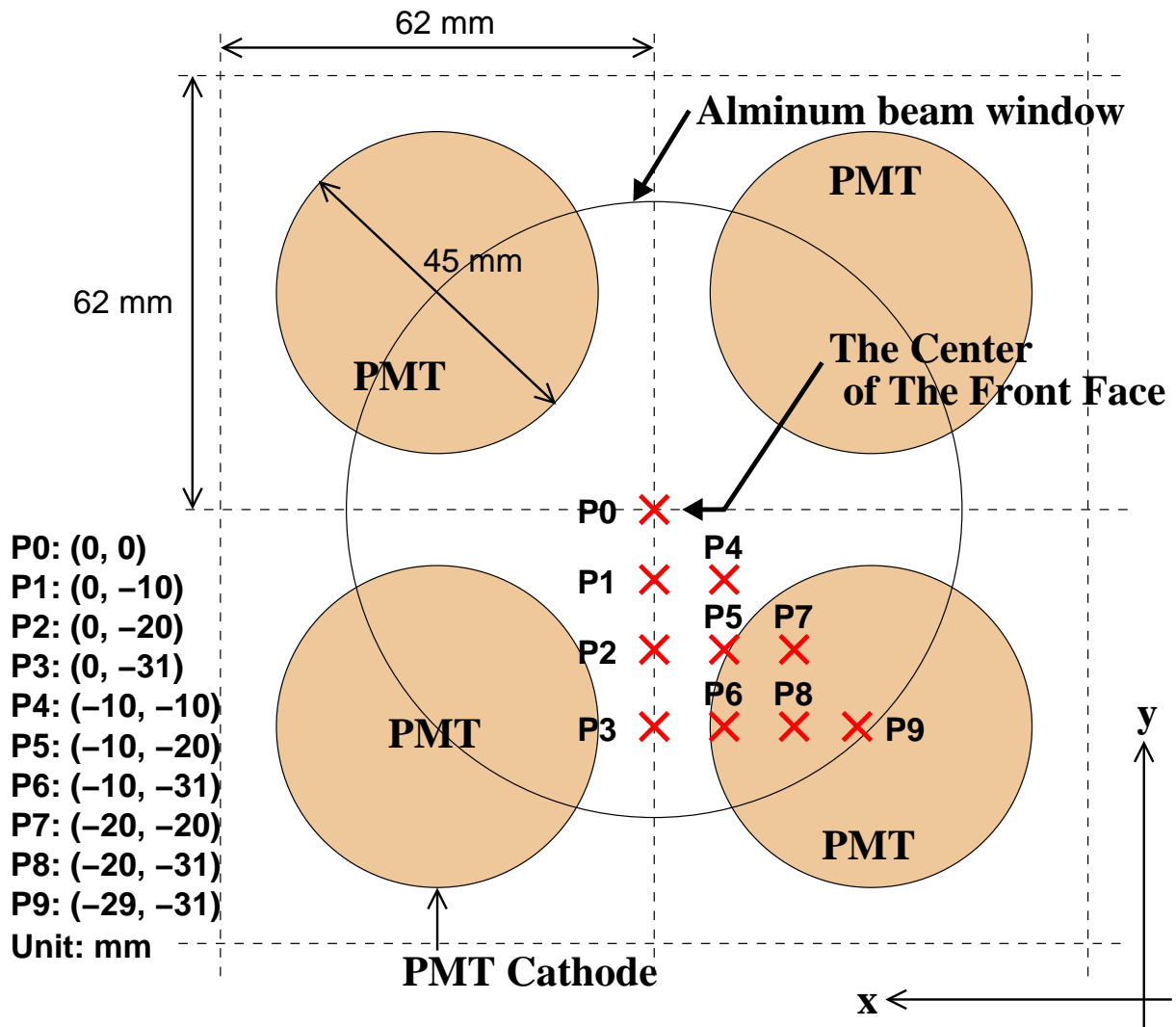


Figure 5.15: Impinging points of γ rays in this test.

Table 5.3: Energy and position of impinging beam in this test.

γ -ray Energy at Compton edge	Impinging position
10 MeV	P0 and P9
20 MeV	P0 and P9
40 MeV	P0 ~ P9

5.6 Position Resolution

5.6.1 Position Reconstruction in Simulation

The first conversion points of γ rays in LXe were reconstructed by using the spread of charge distribution on the front face. The point projected onto the front face can be estimated as:

$$X = \frac{\sum_{i=1}^{36} q_i X_i}{Q_f}, \quad (X = x, y) \quad (5.8)$$

$$Q_f = \sum_{i=1}^{36} q_i, \quad (5.9)$$

where q_i is the number of photoelectrons observed by the i -th PMT located at X_i . We call the X "simple weighted mean". This value tends to be pulled by q_i far from the incident position. For avoiding this problem, we newly devised a method to estimate the incident position. In this method the following procedure was taken:

1. Calculate the simple weighted mean (x, y) .
2. Make a 2-dimensional map with 6×6 blocks as Fig. 5.16. Each block has a circle bin and it corresponds to a PMT photo-cathode with a diameter of 45 mm.
3. Fill the circle bin with PMT outputs like a histogram.
4. Draw a circle whose center is at (x, y) . Define the radius R_f such that the sum of q_i inside the circle becomes a half of Q_f .
5. Calculate the weighted mean of PMT outputs inside the circle. In this case, x_i is the center of overlap of the circle with i -th circle bin.
6. Iterate the 4 and 5 processes till the weighted mean converges.

In other words, the R_f is the radius of the circle such that

$$\frac{\sum_{i=1}^{36} q_i C_i}{Q_f} = 0.5, \quad (5.10)$$

where C_i is an overlap ratio of the circle and i -th circle bin. If the circle includes the i -th circle bin, C_i equals to 1. At this time we introduce a new variable:

$$N_f(0.5) = \sum_{i=1}^{36} C_i. \quad (5.11)$$

This parameter N_f is a number() of PMTs included in the circle R_f , and a function of the ratio n for Q_f . When the ratio n was changed from 0.1 to 0.9 every 0.1, it was found that n of 0.5 was the best. This value $N_f(0.5)$ can be a good measure of the first conversion depth as described later.

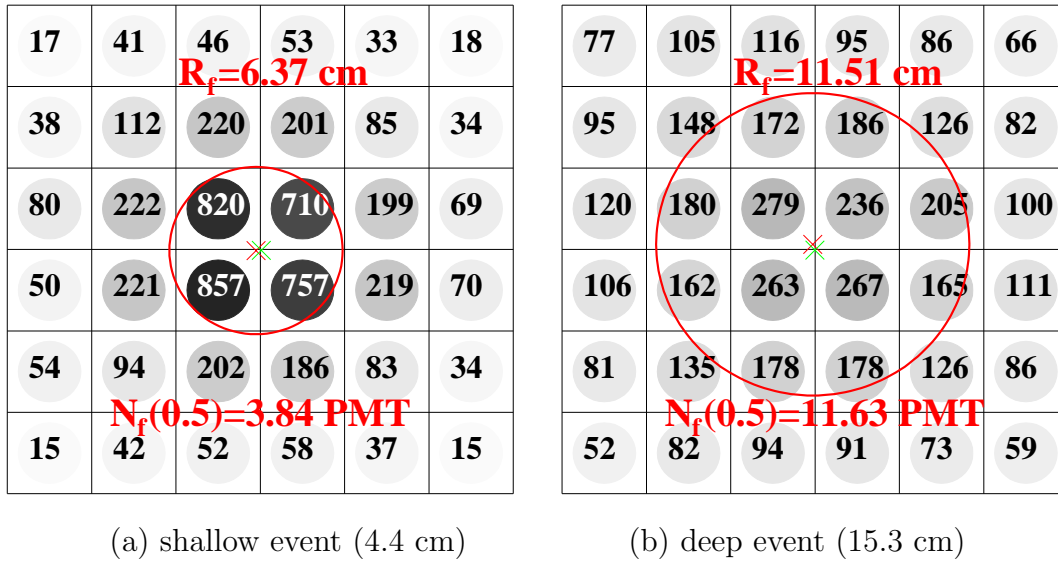


Figure 5.16: Schematic histograms of charge distribution on the front face. Each N_{pe} is drawn with gray scale and as a table in green. The radius of the red circle equals to R_f and $N_f(0.5)$ is the number of PMTs in the circle. Numbers on the circle are observed N_{pe} . Green crosses show true first conversion points. Red crosses show local weighted means.

Figure 5.17 shows a 2-dimensional distribution of differences between true and reconstructed positions obtained from MC simulation data. The data was generated under the following conditions:

- LCS beam with 40-MeV Compton edge.
- Impinging area was 124 mm×124 mm at the center of front face and the beam was uniformly impinged.
- Events the first conversion occurred in the active volume.

The resolution of position reconstruction is estimated to be about 5.7 mm in σ by fitting the distribution with a 2-dimensional Gaussian function, where the sigma in x direction equals to one in y direction.

In Fig. 5.18 a comparison between (a) local weighted mean and (b) simple weighted mean is shown. It is clear that the local weighted mean is superior to the simple weighted mean for deep events. The reconstructed position by the simple weighted mean tends to be pulled to the centers of PMTs whereas the local weighted mean not. Thus we can conclude that the reconstruction of incident γ -ray positions can be done in a less biased way with the local weighted mean.

Fig. 5.19 shows the relation between $N_f(0.5)$ and local weighted mean in MC simulation. It can be seen that the position resolution for the shallow event ($N_f(0.5) < 4$) deteriorates due to the bias by the nearest PMT. In the case of (b), the resolution was very high. In the region both are considered to be biased by the nearest PMT.

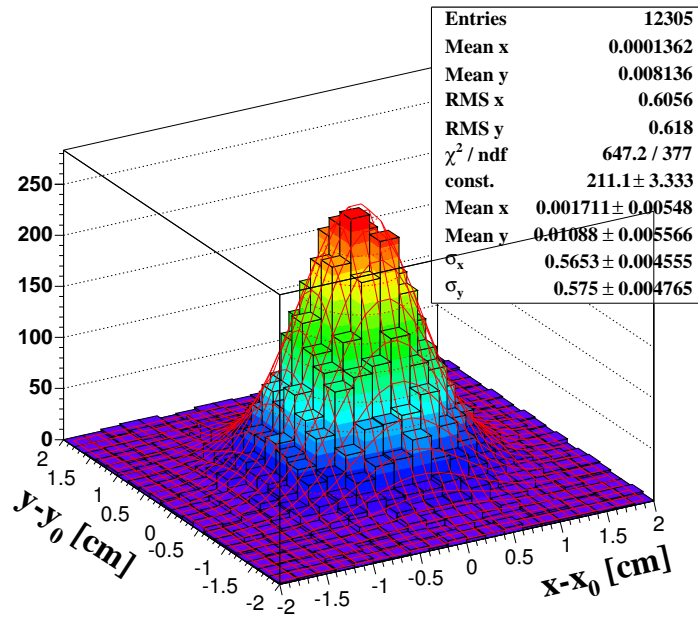
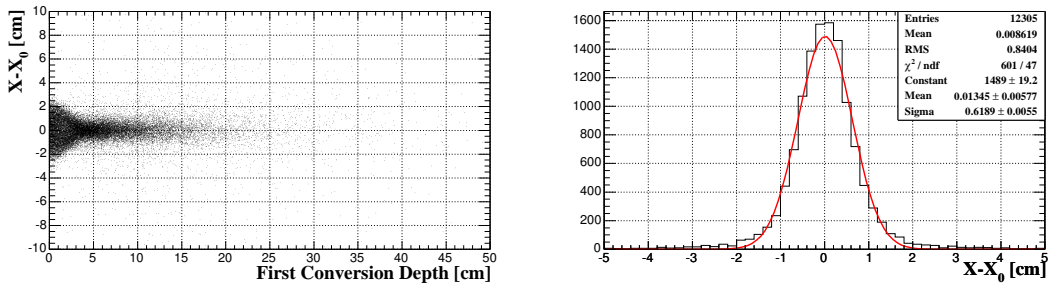
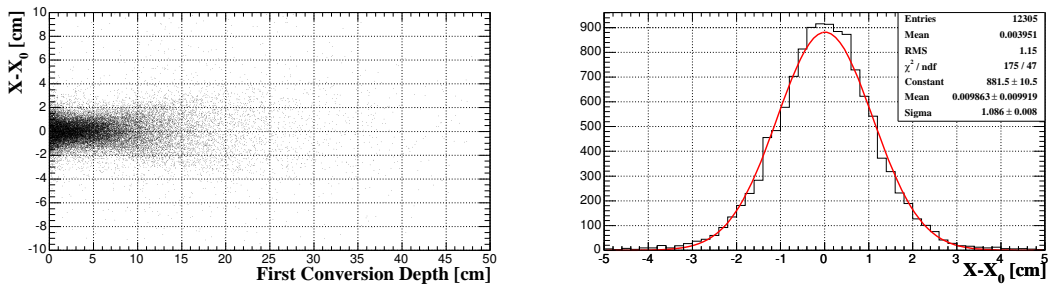


Figure 5.17: Difference between true and reconstructed positions in simulation.



(a) local weighted mean



(b) simple weighted mean

Figure 5.18: Difference between the local weighted mean and simple weighted mean. Left figures of (a) and (b) are the distributions of the residual between reconstructed and true positions vs. the true first conversion depth in MC simulation. Right figures are their projections onto the $x - x_0$ axis and fitting results with Gaussian.

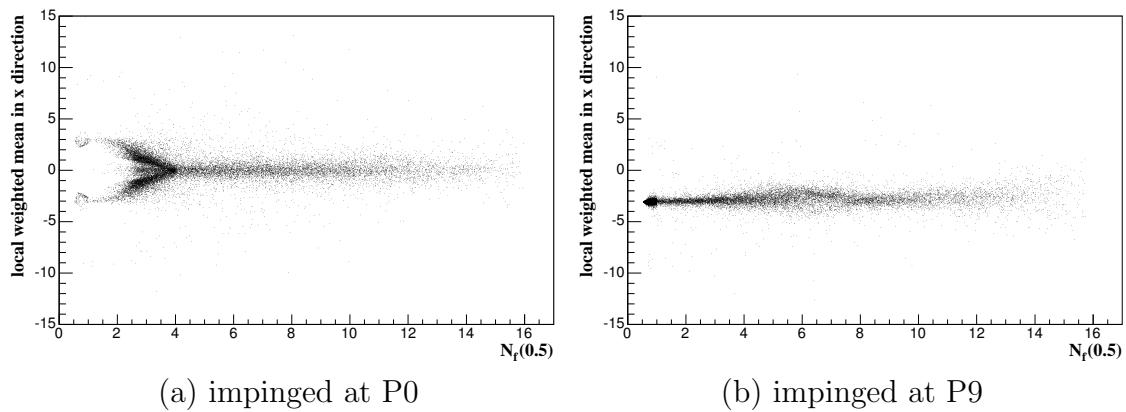


Figure 5.19: The relation between $N_f(0.5)$ and local weighted mean in MC simulation.

5.6.2 Depth Reconstruction in Simulation

The relations between $N_f(0.5)$ and the first conversion depth in MC simulation are shown in Fig. 5.20. It is found that the reconstruction of the depth at P0 is better lower than at P9 especially for the shallow event.

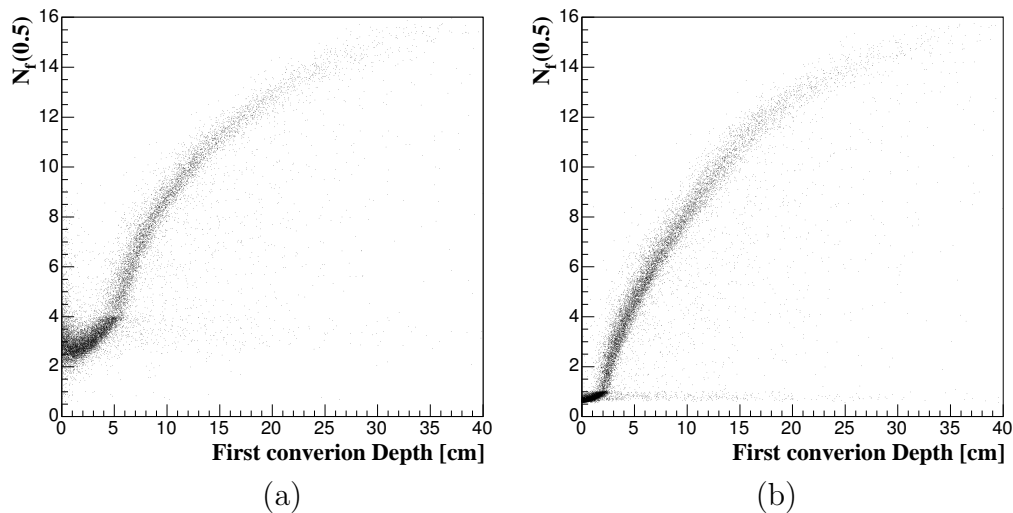


Figure 5.20: The relation between $N_f(0.5)$ and the first conversion depth in MC simulation. The impinging point is P0 for (a) and P9 for (b).

For the same MC data as used in Fig. 5.17, the relation between $N_f(0.5)$ and the first conversion depth was fitted with a second-order polynomial function to be corrected according to the first conversion depth. The result is shown in Fig. 5.21. In MC data, the precision for reconstructing the first conversion depth was 8 mm.

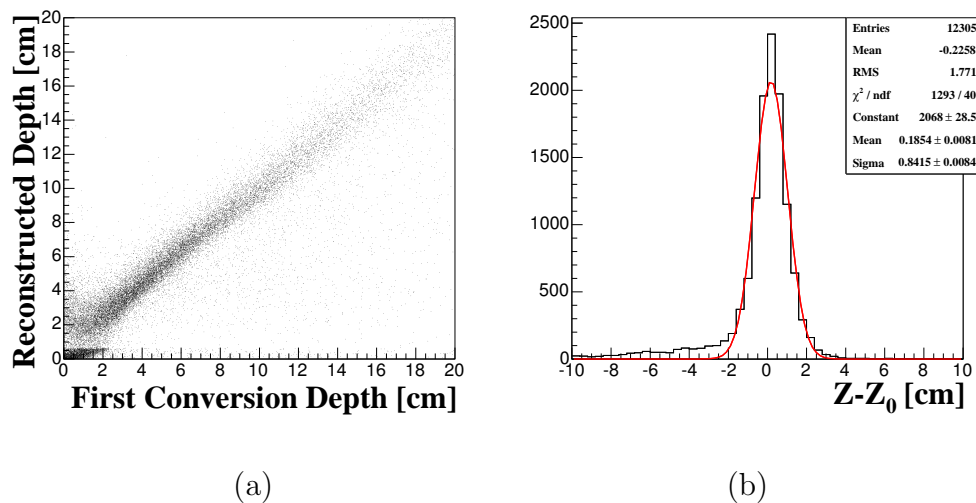


Figure 5.21: (a) Scatter plot of reconstructed and the true first conversion depths. (b) Residual distribution after reconstruction.

5.6.3 Position Reconstruction

Position resolution was evaluated after correcting with QEs obtained in subsection 5.4.2.

$$q'_i = q_i \times \frac{\bar{Q}}{Q_i}, \quad (5.12)$$

where Q_i means measured QE of i -th PMT, and \bar{Q} is an average of all QEs. These corrected charge q'_i was used in Eq. 5.9, 5.10 instead of q_i .

Fig. 5.22 shows that local weighted mean and $N_f(0.5)$ in experimental data. The behavior of reconstructed position was a bit different from one in MC simulation (Fig. 5.19). As seen in (b.1) of Fig. 5.22, the obtained means are pulled by the center of the front face. This phenomenon is considered to be caused by the miscalculation of QE. The position reconstruction depends on the accuracy of QE measurement. However the accuracy method of QE has not established yet.

5.6.4 Depth Dependence

To evaluate the position resolution, the events in the range of $4.0 < N_f(0.5) < 12.0$ was selected at the cost of the efficiency because too shallow or deep events are highly biased. This range corresponds to the actual first conversion depth from 4.5 cm to 18 cm, and the selection efficiency is about 35% from the MC simulation. More intelligent algorithm has to be devised so as not to discard such events. The events were sliced every $N_f(0.5)$ of 1.0 to fit with a 2-dimensional double Gaussian, which has four sigmas: narrow components σ_x and σ_y , and broad components ρ_x and ρ_y , where x and y mean the direction. An example of the fitting is shown in Fig. 5.23. All the results are shown in Fig. 5.24 for 10-MeV Compton edge, Fig. 5.25 for 20 MeV, and Fig. 5.26 for 40 MeV.

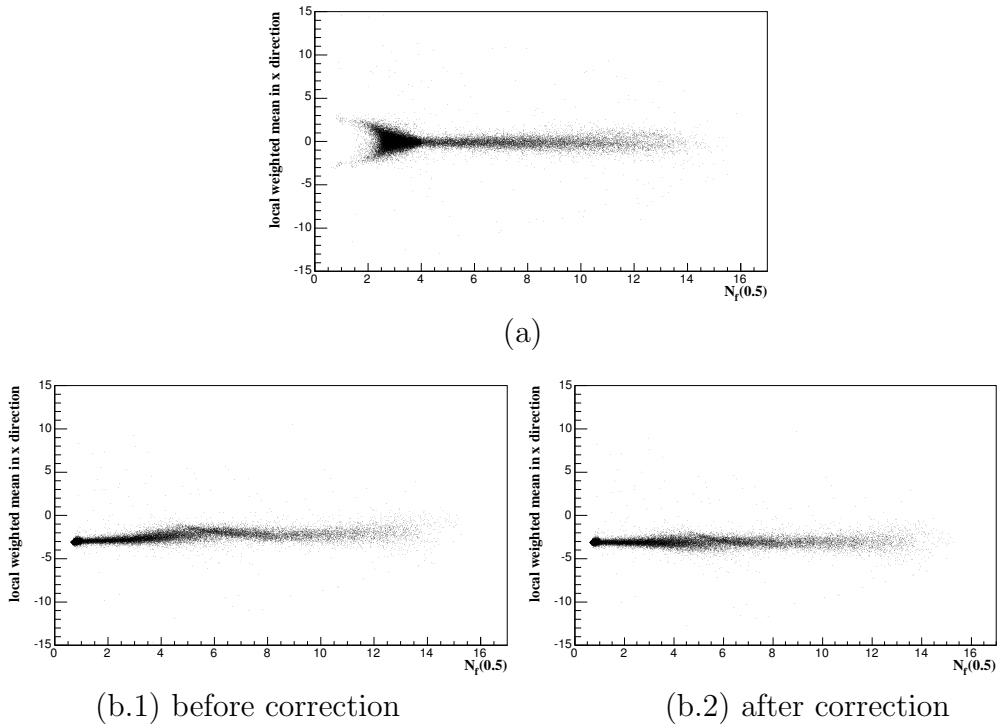


Figure 5.22: The relation between the depth parameter N_f and the local weighted mean. Compton edge energy is 40 MeV, and the incident point is at P0 (a) and at P9 (b).

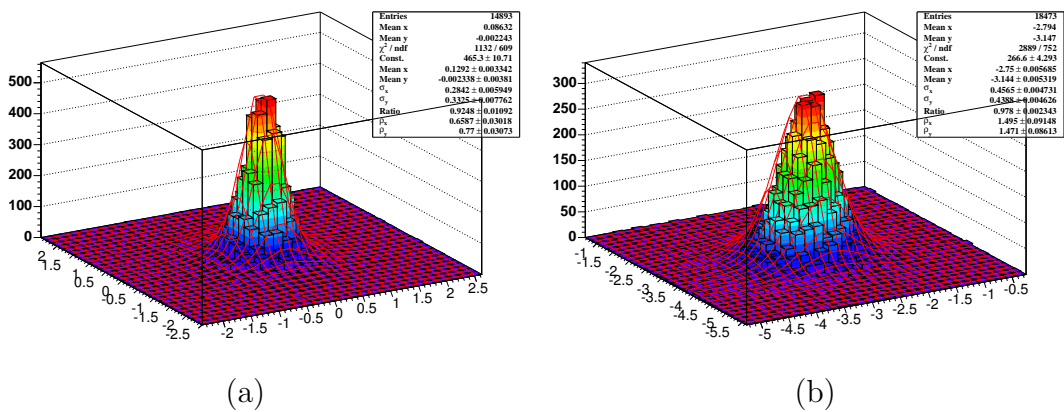
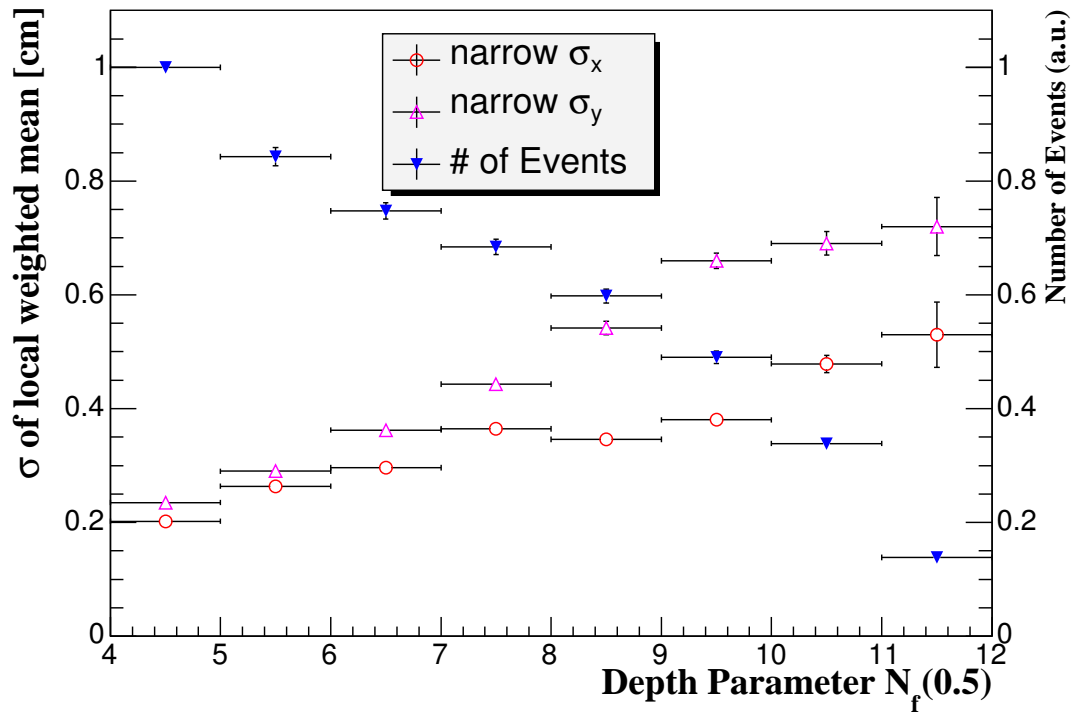
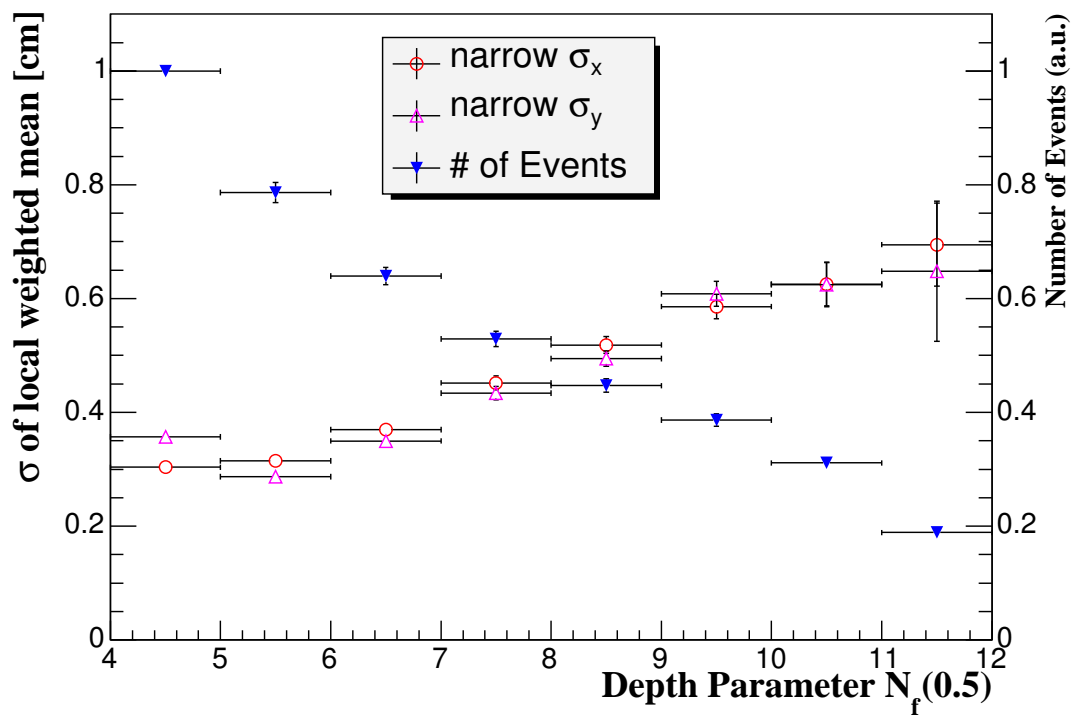


Figure 5.23: Examples of the fitting result with a 2-dimensional double Gaussian for $E_C = 40$ MeV and $N_f(0.5) > 4.0$. The incident point is at P0 (a) and at P9 (b).

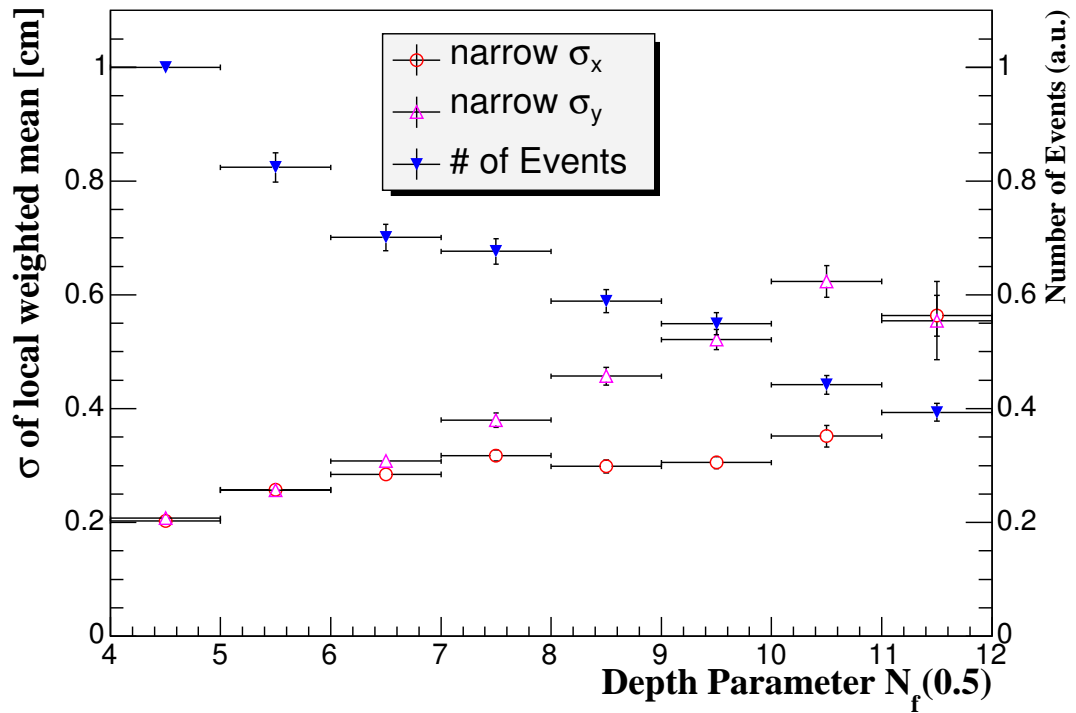


(a) 10 MeV, at P0.

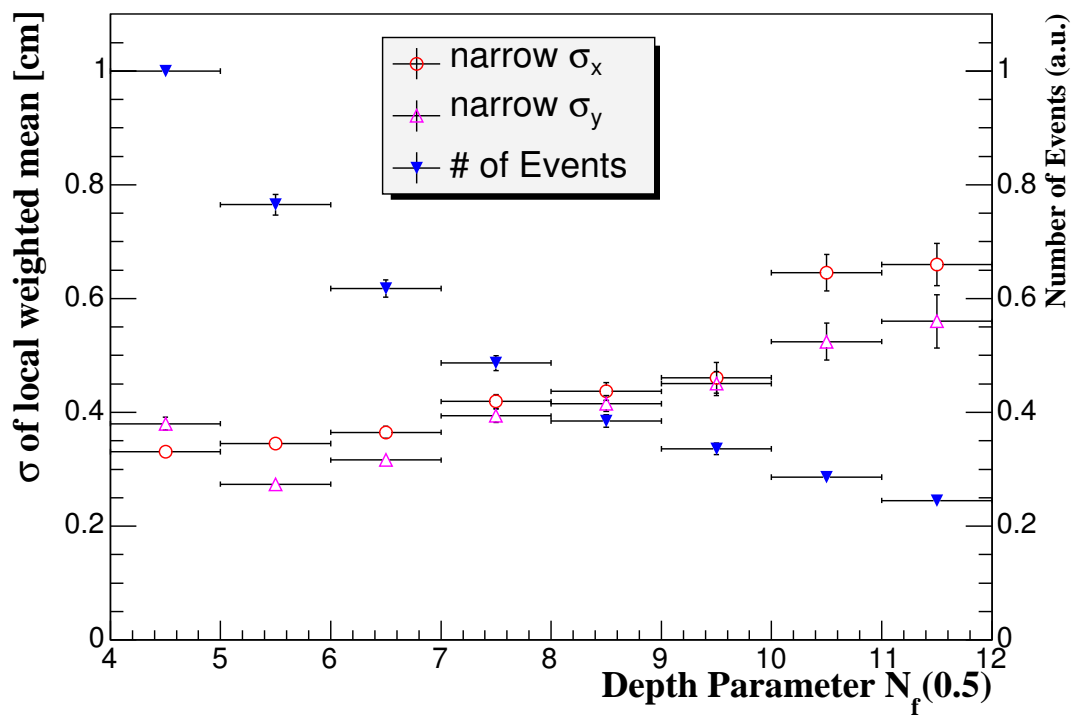


(b) 10 MeV, at P9

Figure 5.24: Position resolution as a function of $N_f(0.5)$ for $E_C = 10$ MeV, impinging at (a) P0 and (b) P9.

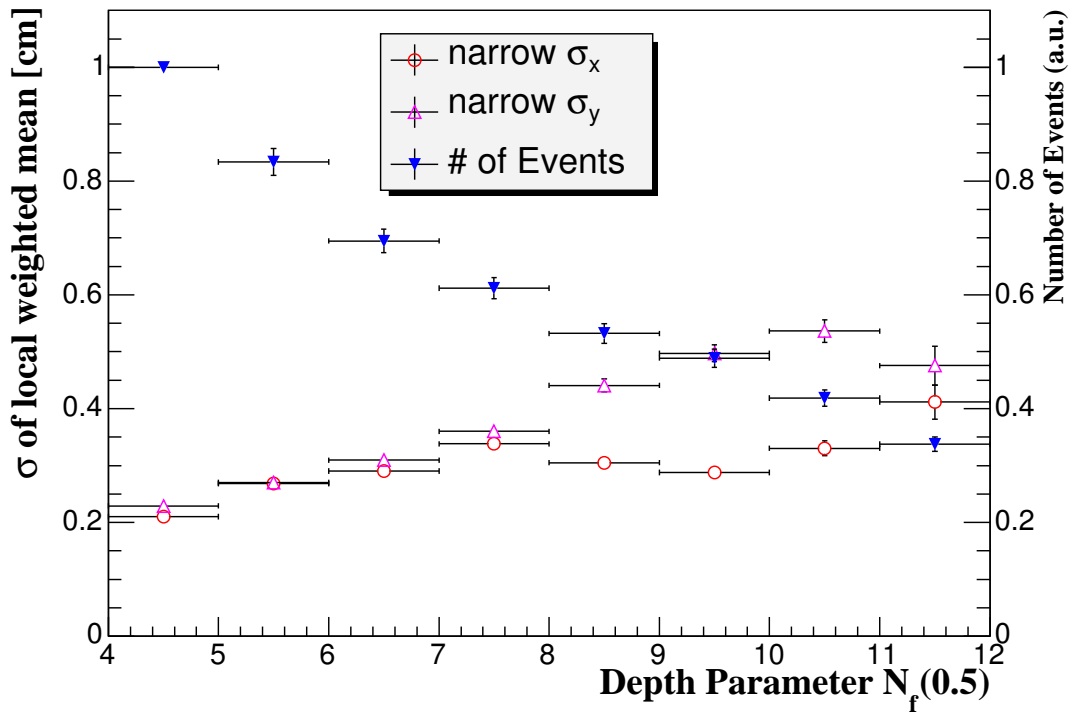


(a) 20 MeV, at P0.

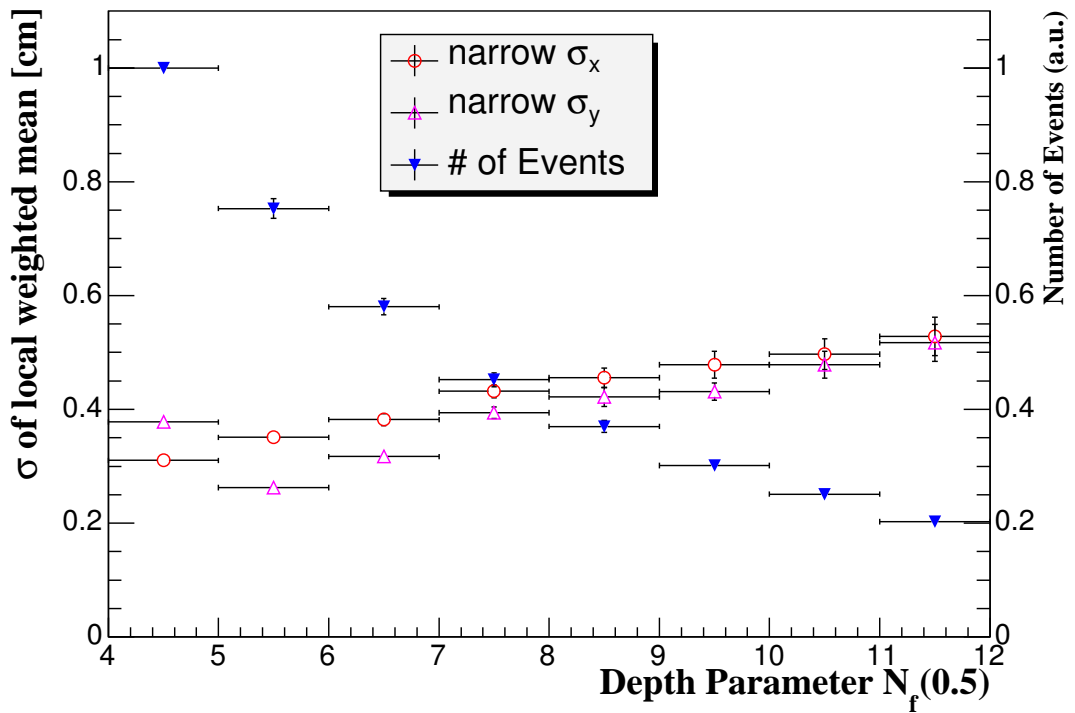


(b) 20 MeV, at P9

Figure 5.25: Position resolution as a function of $N_f(0.5)$ for $E_C = 20$ MeV, impinged at (a) P0 and (b) P9.



(a) 40 MeV, at P0.



(b) 40 MeV, at P9.

Figure 5.26: Position resolution as a function of $N_f(0.5)$ for $E_C = 40$ MeV, impinged at (a) P0 and (b) P9.

5.6.5 Energy Dependence

The difference of the resolution according to the incident beam energy was investigated. The range of $N_f(0.5)$ was over 4.0. The events were sliced every $N_f(0.5)$ of 1.0 to be corrected by shifting to the correct incident position (p0 or P9). The corrected events are shown in Fig. 5.22 (b.2). After the correction, the events were fitted with a 2-dimensional double Gaussian. The position resolution from measured data and MC simulation are shown in Tab. 5.4 and Tab. 5.5, respectively.

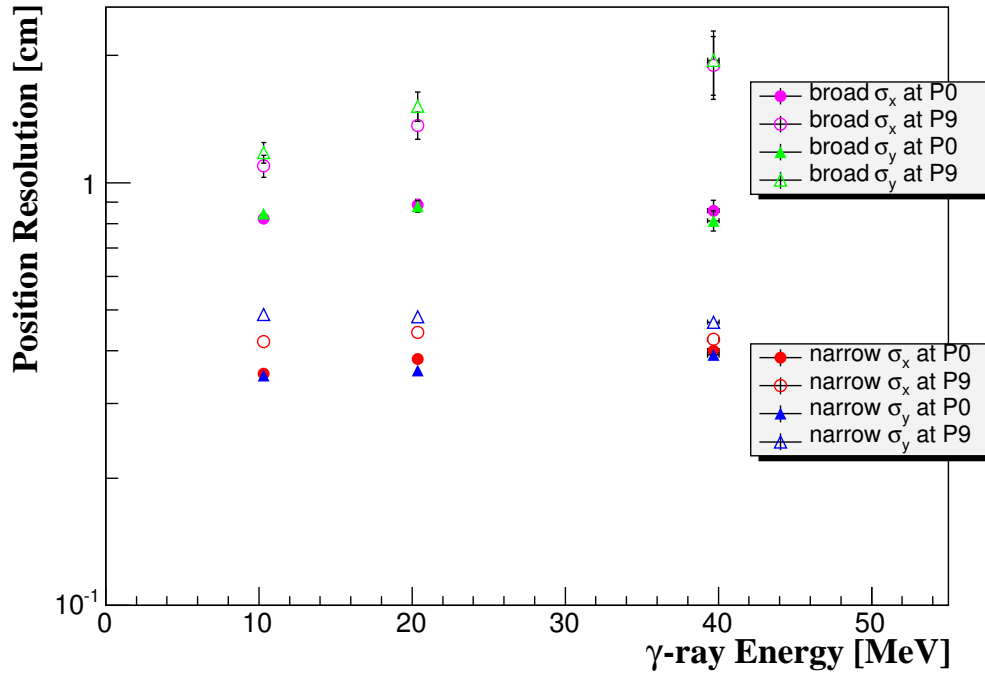
Table 5.4: Position resolution from measured data. Upper value in a column is narrow component and lower value is broad one. Unit is cm. The percentage in a parenthesis is a fraction of each component.

position resolution in x direction			
Position\Energy	10 MeV	20 MeV	40 MeV
P0	0.38 ± 0.01 (77.1%)	0.40 ± 0.01 (80.5%)	0.42 ± 0.01 (83.8%)
	0.89 ± 0.02 (22.9%)	0.86 ± 0.05 (19.5%)	1.10 ± 0.07 (16.2%)
P9	0.42 ± 0.01 (91.3%)	0.44 ± 0.00 (93.5%)	0.43 ± 0.00 (95.3%)
	1.10 ± 0.07 (8.7%)	1.37 ± 0.10 (6.5%)	1.90 ± 0.32 (4.7%)
position resolution in y direction			
Position\Energy	10 MeV	20 MeV	40 MeV
P0	0.35 ± 0.00 (77.1%)	0.36 ± 0.01 (80.5%)	0.39 ± 0.01 (83.8%)
	0.85 ± 0.01 (22.9%)	0.88 ± 0.03 (19.5%)	0.81 ± 0.05 (16.2%)
P9	0.49 ± 0.01 (91.3%)	0.48 ± 0.01 (93.5%)	0.47 ± 0.00 (95.3%)
	1.18 ± 0.07 (8.7%)	1.52 ± 0.12 (6.5%)	1.95 ± 0.34 (4.7%)

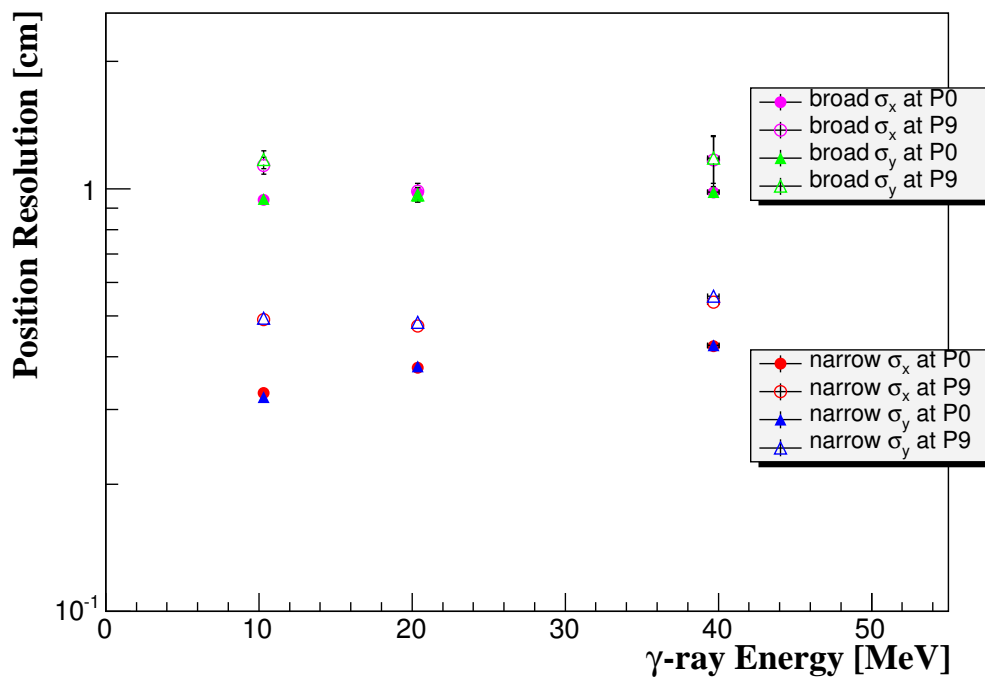
Table 5.5: Position resolution from MC simulation. Upper value in a column is narrow component and lower value is broad one. Unit is cm. The percentage in a parenthesis is a fraction of each component.

position resolution in x direction			
Position\Energy	10 MeV	20 MeV	40 MeV
P0	0.37 ± 0.01 (82.7%)	0.47 ± 0.01 (90.1%)	0.41 ± 0.01 (87.9%)
	1.12 ± 0.07 (11.3%)	1.66 ± 0.25 (9.9%)	1.51 ± 0.15 (12.1%)
P9	0.50 ± 0.01 (90.2%)	0.44 ± 0.01 (87.6%)	0.49 ± 0.01 (89.3%)
	2.64 ± 0.11 (9.8%)	1.66 ± 0.10 (12.4%)	2.15 ± 0.54 (10.7%)
position resolution in y direction			
Position\Energy	10 MeV	20 MeV	40 MeV
P0	0.35 ± 0.01 (82.7%)	0.48 ± 0.01 (90.1%)	0.41 ± 0.01 (87.9%)
	1.13 ± 0.06 (11.3%)	1.87 ± 0.33 (9.9%)	1.56 ± 0.17 (12.1%)
P9	0.51 ± 0.01 (90.2%)	0.43 ± 0.01 (87.6%)	0.50 ± 0.01 (89.3%)
	2.39 ± 0.11 (9.8%)	1.78 ± 0.10 (12.4%)	2.26 ± 0.68 (10.7%)

Fig. 5.27 shows the energy dependence of position resolutions.



(a) measured data



(b) MC simulation

Figure 5.27: The resolution of the local weighted mean in σ as a function of γ -ray energy. Only the statistical errors in the fitting are presented as error bars.

5.6.6 Difference between the Data and the Simulation

It is found that the position resolution from the measured data is better than that from the simulation. The position reconstruction in the measured data might be biased more than that in the MC and underestimated for some reasons. However it is appropriate that the discrepancy comes from defectiveness of the modeling in the MC simulation, since both resolutions were estimated by the same method. Indeed, the behavior of the scintillation photons close to PMTs is not understood well. There remain some parameters to be tuned: refractive index of xenon and PMT window for xenon scintillation photons, and reflectivity of PMT holders. If these parameters were tuned properly, the resolution in the simulation should be coincident with the intrinsic position resolution, which will be discussed in the next subsection.

5.6.7 Intrinsic Position Resolution

Here we will evaluate the intrinsic position resolution, which means the resolution concerning only the LXe scintillation process. The intrinsic resolution was expressed as:

$$\sigma_{intr}^2 = \sigma_x^2 - (\sigma_{noise}^2 + \sigma_{beam}^2 + \sigma_{col}^2), \quad (5.13)$$

where σ_{intr} , σ_{noise} , σ_{beam} , and σ_{col} are intrinsic position resolution, error sources from pedestal noise, the spread of the LCS beam, and the radius of the collimator, respectively. After excluding those factors from the obtained resolution, the intrinsic resolution will be evaluated.

Electronics Noise

The electronics noise represents the pedestal noise. MC simulations for monochromatic γ rays of 10 MeV, 20 MeV, and 40 MeV were performed. For those data, the incident positions were reconstructed after taking account of coherent and incoherent noises obtained in Sec. 5.4.4. The result is shown in Tab. 5.6. In principle the coherent noise does not affect the position resolution. The electronics noise was not dominant because the pedestal noise was small enough.

Table 5.6: Deterioration by electronics noise. Unit is cm.

Position \ Energy	10 MeV	20 MeV	40 MeV
P0	0.02	0.02	0.00
P9	0.05	0.04	0.01

LCS beam

As shown in Tab. 5.1, the energy spread of the Compton edge is 1%. The deterioration of position resolution was estimated by MC simulation. As shown in Tab. 5.7, little influence was seen.

Table 5.7: The effect by fluctuation of LCS beam energy. Unit is cm.

Position \ Energy	10 MeV	20 MeV	40 MeV
P0	0.02	0.00	0.01
P9	0.01	0.01	0.00

Radius of Collimator

The diameter of the second collimator was 1 mm ϕ and 2 mm ϕ . The analysis in Sec. 5.6.5 was performed for events with the 1 mm ϕ collimator. We also analyzed events with 2 mm ϕ collimator. Comparing both results, no significant differences were seen. The contribution to the error of the position resolution was considered to be negligible. It can be guessed by the spectra in Fig. 5.4.

From these evaluations, we could obtain the intrinsic resolution. However the contribution of σ_{noise} , σ_{beam} , and σ_{col} to the position resolution was negligible. Therefore the obtained resolution is considered to be almost intrinsic.

5.6.8 Systematic Error

Parameters in MC Simulation

The position resolution can be affected by the modeling in MC simulation because the position reconstruction depends on the accuracy of QE determination. Some parameters is not still fixed and have indefiniteness.

We examined whether the position resolution changed by varying each parameters in a certain range. The method was as follows:

- 1 Simulate α -particle events with a parameter set to a certain value.
- 2 Compare the N_{pe} observed by a PMT in experimental data with one in the simulation to estimate the QE of the PMT.
- 3 Reconstruct the incident position on the basis of the obtained QEs.
- 4 Fit the the distribution of the reconstructed position.
- 5 Obtain the difference between this resolution and one in Tab. 5.4.

Parameters to be examined were refractive index of LXe (n_{Xe}), Rayleigh scattering length (λ_{sca}), absorption length (λ_{abs}), and reflection ratio on the lateral face. The range of n_{Xe} was defined by Tab. 3.3, λ_{sca} λ_{abs} were by the result obtained in Chap. 4, and reflection ratio was from [92]. Tab. 5.8 shows the difference with position resolutions in MC simulations. Those errors are added to position resolutions in Tab. 5.4 as systematic errors.

Table 5.8: Difference of the position resolution by changing parameters in the MC simulation for QE estimate. Unit is cm.

Parameter	default value	range or value	Incident energy & position					
			10 MeV		20 MeV		40 MeV	
			P0	P9	P0	P9	P0	P9
n_{Xe}	1.62	1.56 to 1.72	0.1	0.0	0.0	0.0	0.1	0.0
λ_{sca}	45 cm	40 cm to 50 cm	0.1	0.1	0.1	0.1	0.0	0.0
λ_{abs}	1 m	90 cm to 3 m	0.0	0.0	0.0	0.0	0.0	0.0
Reflection	0%	0% to 10%	0.1	0.2	0.1	0.1	0.1	0.1
Quadratic Sum			0.2	0.2	0.1	0.1	0.1	0.1

Consequently the difference between the resolutions from the data and simulations was not understood completely. We should compare the position resolution with ones from simulation samples obtained by changing values of those parameters.

5.6.9 Position Resolution

The position resolution does not always depend on γ -ray energy. It is difficult to extrapolate the position resolution to 52.8-MeV. From MC simulations, position resolution for monochromatic 10-MeV γ rays is better than those for 20 MeV and 40 MeV. It is considered to be caused by electromagnetic shower because the critical energy of xenon is 14.5 MeV. However the position resolution improves according to γ -ray energy over 20 MeV. Hence the position resolution for $E_C = 40$ MeV is substituted for the resolution in 52.8 MeV.

5.7 Energy Resolution

5.7.1 Compton Edge

The energy spectrum of the LCS beam has a sharp Compton edge and lower tail. In order to evaluate the energy resolution, the shape of Compton edge was fitted with a convolution of the Compton spectrum and a response function. The Compton spectrum was simulated with parameters given in Tab. 5.1 and experimental setup shown in Fig. 5.3 on the basis of Klein-Nishina formula [84]. The spectra are shown in Fig. 5.28.

The amount of pile-ups depends on the beam current in TERAS. Fig. 5.29 shows pile-ups of multiple gamma rays when the beam current was about 120 mA. In this analysis the data for low electron beam current (~ 30 mA) were used to contamination of suppress pile-ups events as shown in Fig. 5.30. Hence the subtraction of pile-up events was not done in fitting procedure.

As seen in Fig. 5.30, the measured spectrum has a broader tail than the incident beam spectrum. The lower tail comes from conversions in the front material (See Fig. 3.5) or in the second collimator made of lead. However the Compton edge is sharp enough to estimate the energy resolution. The lower tail was employed for that purpose.

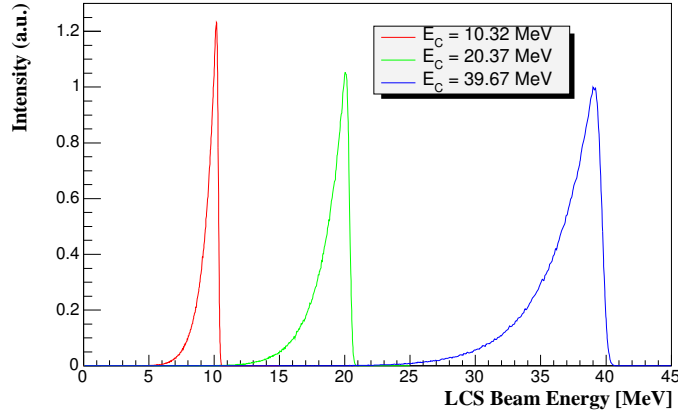
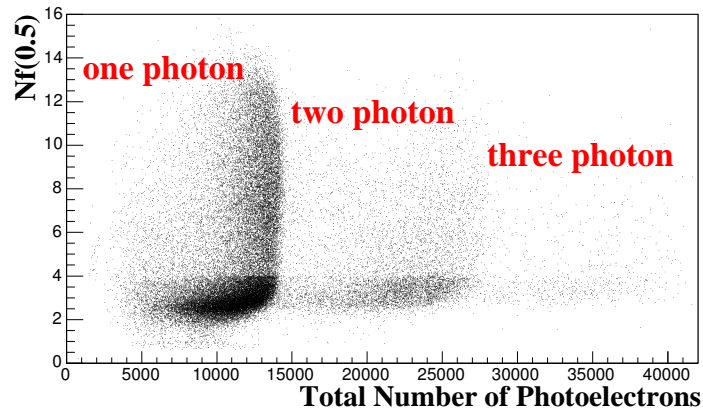


Figure 5.28: LCS beam spectra in this test.

Figure 5.29: Pile-up events in high beam current ($E_C=10$ MeV).

5.7.2 Fitting Function

The response function was a Gaussian with lower tail as follows:

$$f(E) = \begin{cases} A \exp\left(\frac{t}{\sigma_u^2} \left\{ \frac{t}{2} - (E - \mu) \right\}\right), & E \leq \mu + t, \\ A \exp\left(\frac{(E - \mu)^2}{-2\sigma_u^2}\right), & E > \mu + t, \end{cases} \quad (5.14)$$

where σ_u is the sigma in the upper part of the response function, E is the beam energy, μ is the peak of the response function, and t is the transition parameter which represents the degree of the lower tail. For this function FWHM is written as:

$$\text{FWHM} = \sigma_u \sqrt{\ln 4} + \frac{\sigma_u^2}{t} \ln 2 + \frac{t}{2}. \quad (5.15)$$

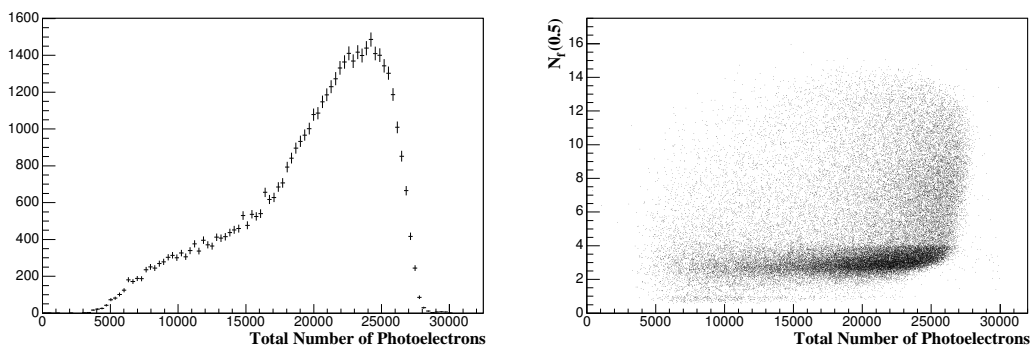
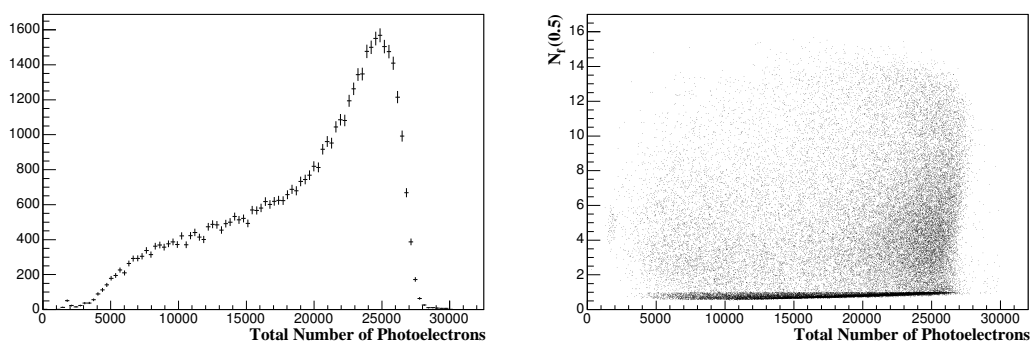
(a) $E_C=40$ MeV, impinged at P0(b) $E_C=40$ MeV, impinged at P9

Figure 5.30: Measured energy spectrum for LCS beam.

5.7.3 Fitting Procedure

Energy resolution was evaluated using Q_{sum} after QE correction, where Q_{sum} means a sum of N_{pe} over all the 228 PMTs written as:

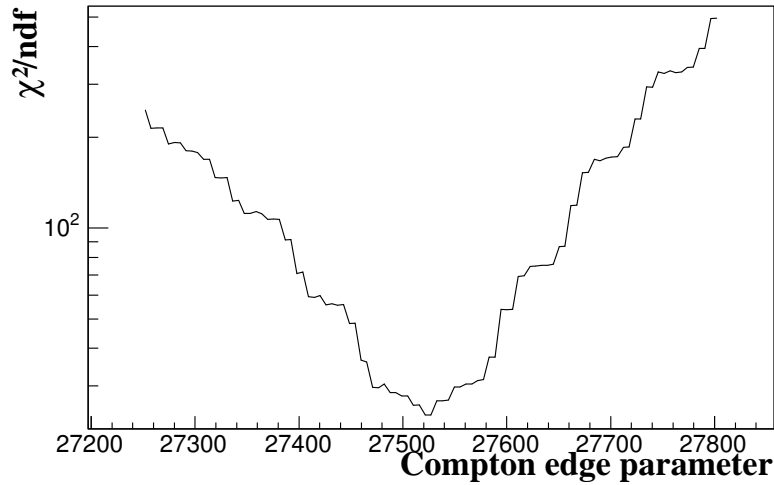
$$Q_{\text{sum}} = \sum_{i=1}^{228} q'_i, \quad (5.16)$$

where q'_i is the same as Eq. 5.12.

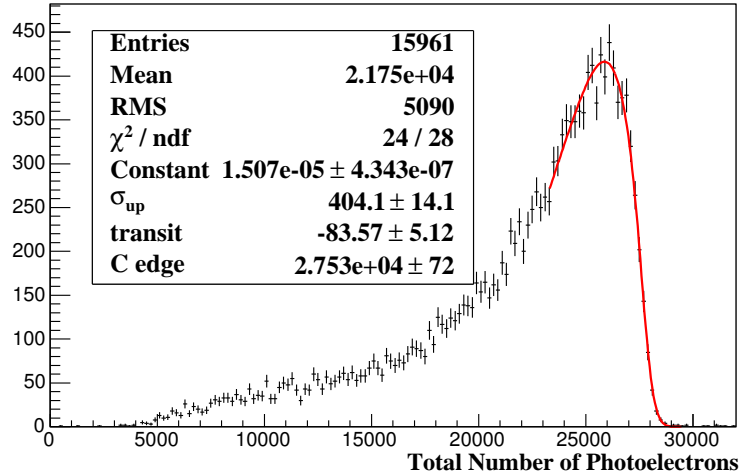
Parameters in the fitting with the convolution are normalization factor (A), upper part of sigma (σ_u), transition (t), and Compton edge parameter. The edge parameter is N_{pe} corresponding to the Compton edge in terms of MeV.

This fitting needed special care because the edge parameter tended to be ‘strong’ in the fitting procedure. That is, the other parameters strongly depends on the edge parameter. The first step was to define the proper initial value of the edge parameter. For a start, some fittings were done in order to roughly obtain a fitting result. However it was possible that this result fell into a local minimum. As shown Fig. 5.31(a), the edge parameter was scanned over the upper tail, fixed the other parameters. From this plot, the Compton edge parameter such that chi-square was minimum was set to the initial value. The next step was to define the fitting range. Since no pile-up events were seen in the spectrum as shown in Fig. 5.30, the upper limit of the fitting range was set to the bottom of the upper tail. On the other hand, the lower limit had to be defined with chi-square as well as the

Compton edge parameter. In this analysis, it was important to fit the Compton edge to evaluate σ_u while it was not necessary to fit the full lower tail. The N_{pe} where χ^2/ndf became the minimum was selected as the lower limit. Because the lower limit could over the peak of the fitting curve, it was set to $-5\sigma_u$ from the peak at least. Fig. 5.31(b) is an example of the fitting when the depth parameter $N_f(0.5)$ is over 4.0.



(a)

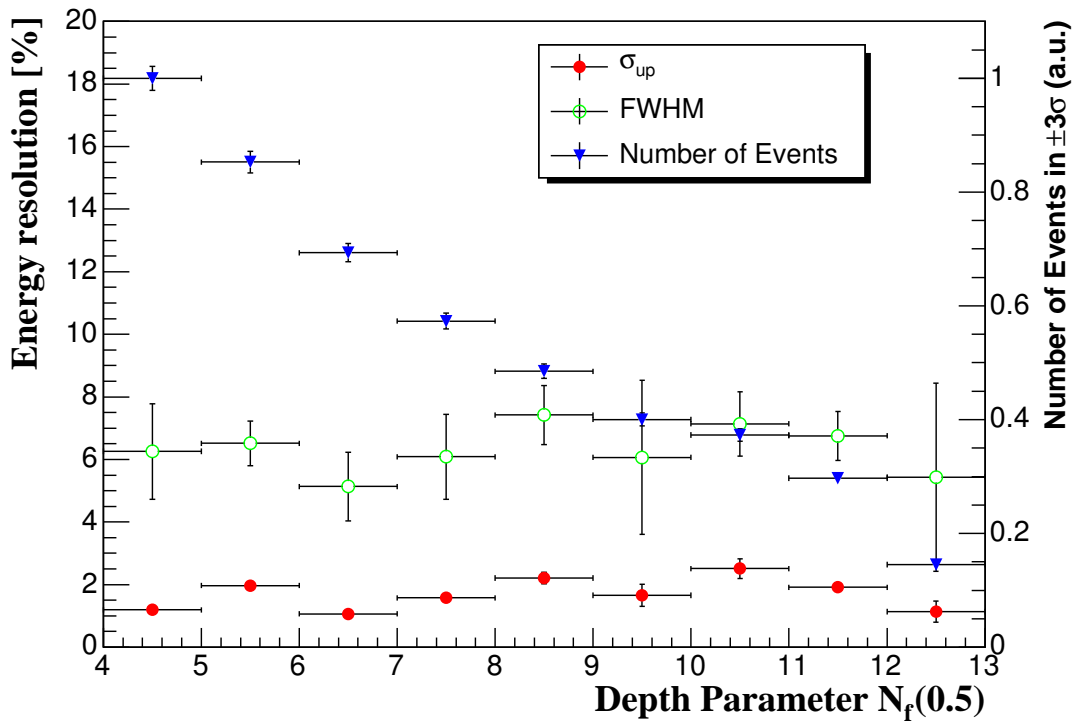


(b)

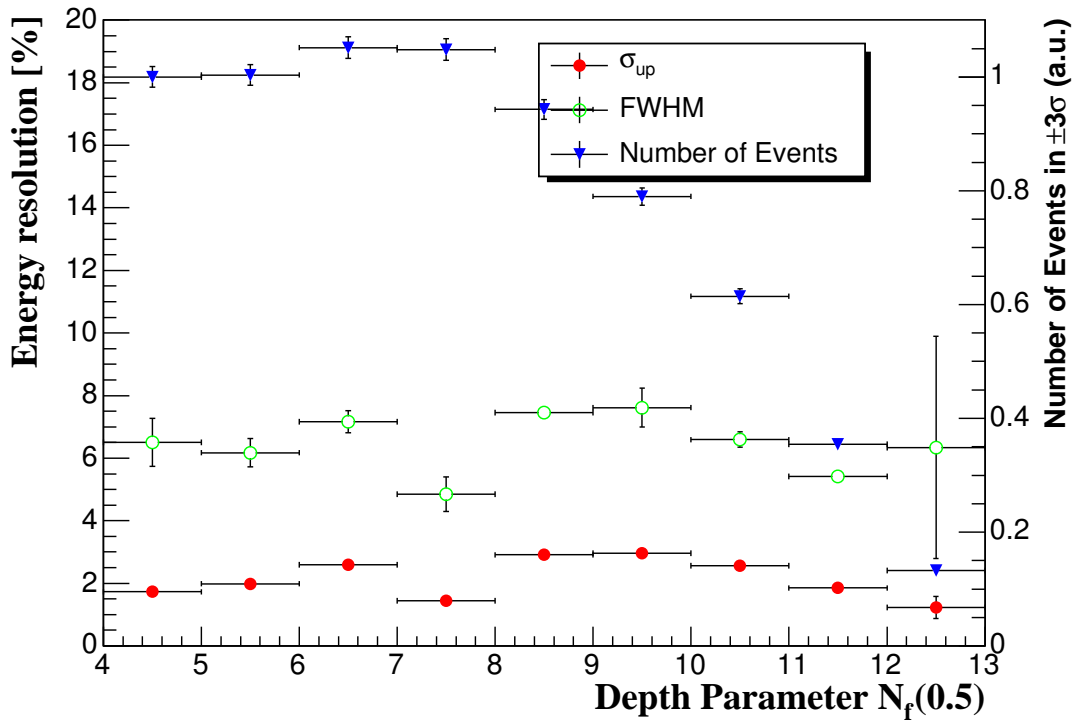
Figure 5.31: (a)The relation between χ^2/ndf as a function of the lower limit of the fitting range. (b)An example of the fitting.

5.7.4 Depth Dependence

As done in the estimate of position resolution, $N_f(0.5)$ was used to investigate the depth dependence of energy resolution. The all results are shown in Fig. 5.32 for 10-MeV Compton edge, Fig. 5.33 for 20 MeV, and Fig. 5.34 for 40 MeV.

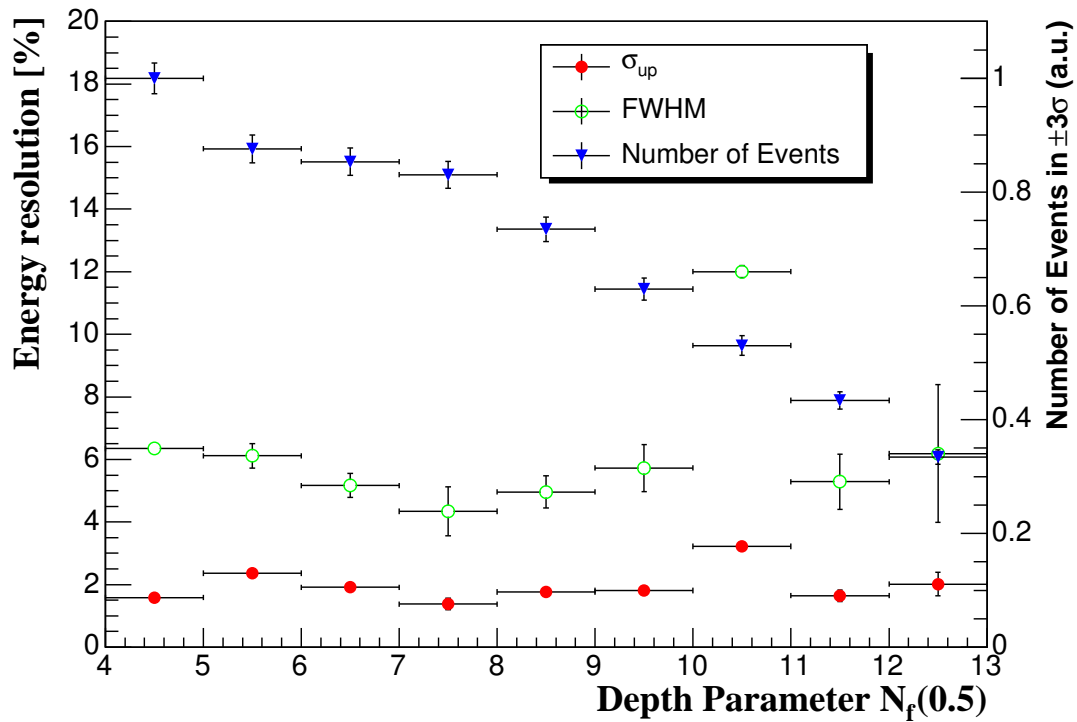


(a) 10 MeV, at P0.

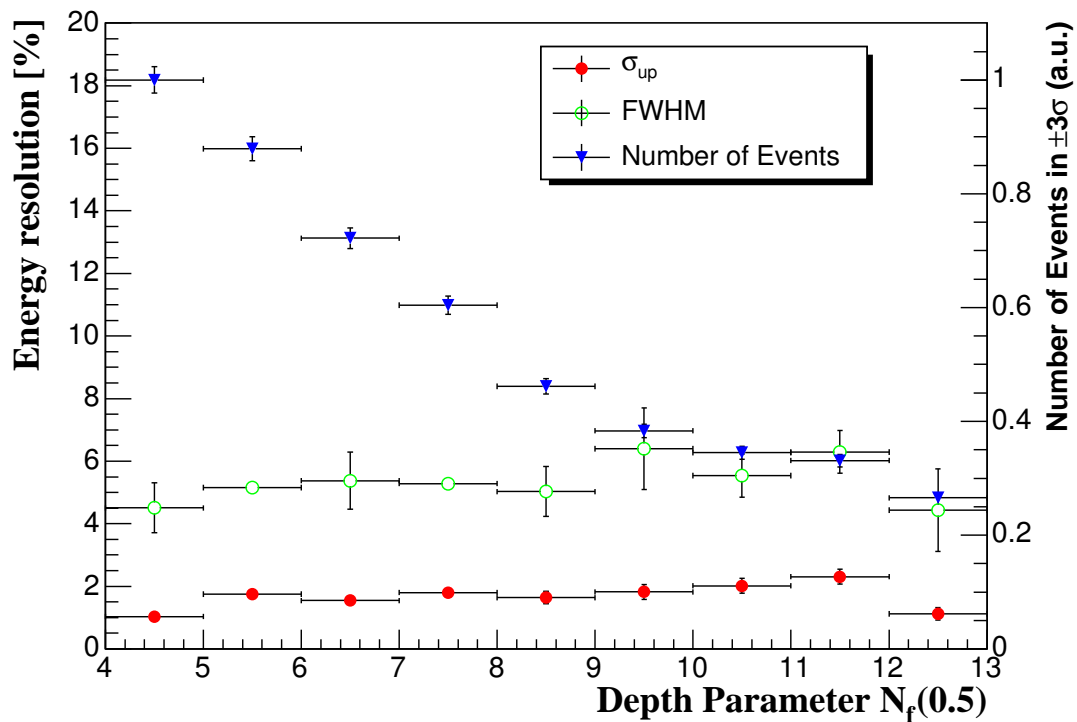


(b) 10 MeV, at P9.

Figure 5.32: Energy resolution as a function of $N_f(0.5)$ for $E_C = 10$ MeV, impinged at (a) P0 and (b) P9.

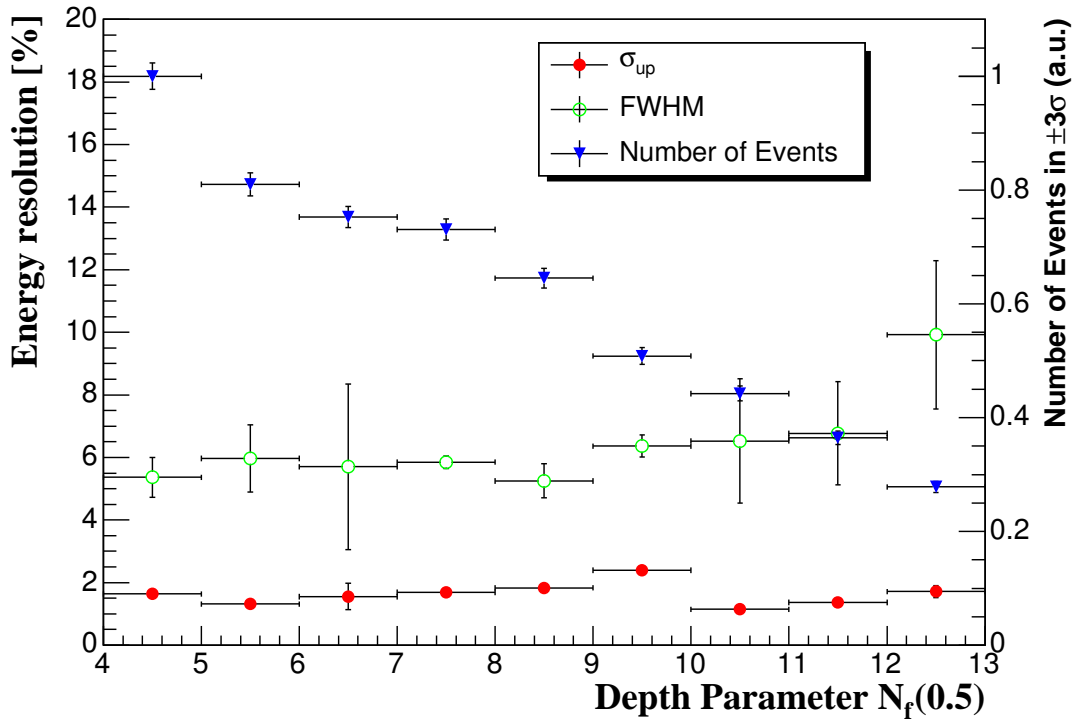


(a) 20 MeV, at P0.

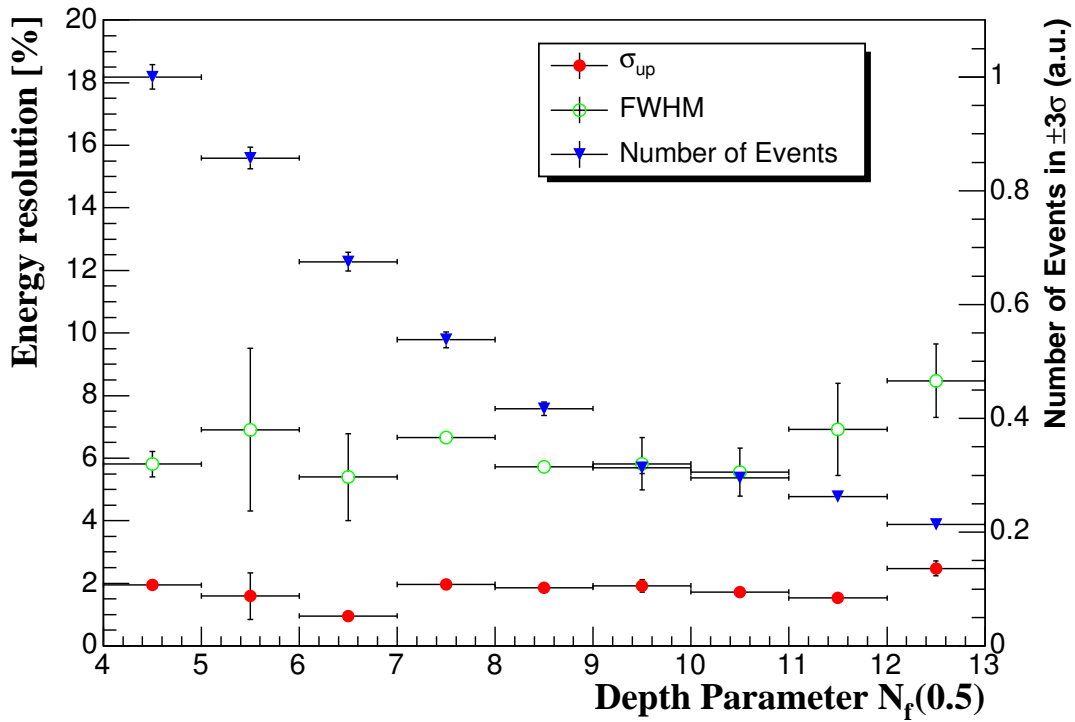


(b) 20 MeV, at P9.

Figure 5.33: Energy resolution as a function of $N_f(0.5)$ for $E_C = 20$ MeV, impinged at (a) P0 and (b) P9.



(a) 40 MeV, at P0.



(b) 40 MeV, at P9.

Figure 5.34: Energy resolution as a function of $N_f(0.5)$ for $E_C = 40$ MeV, impinged at (a) P0 and (b) P9.

5.7.5 Energy Dependence

The energy resolution is expected to be improved according to increase in N_{pe} . In order to verify the statistical energy dependence, the resolution for 10 MeV, 20 MeV, and 40 MeV were evaluated with an event selection such that $N_f(0.5) \geq 4.0$. The result is summarized in Tab. 5.9(a). We also evaluated the energy dependence in MC simulation as shown in Tab. 5.10(b). There are some differences between the results from measured data and MC simulation. In the later subsection, we will discuss the discrepancy.

Table 5.9: Energy resolution measured in LCS beam test. Unit is %.

Position\Energy	10 MeV	20 MeV	40 MeV
P0	3.15 ± 0.04	2.12 ± 0.06	1.47 ± 0.05
P9	3.06 ± 0.07	2.07 ± 0.01	1.47 ± 0.06

Table 5.10: Energy resolution in MC simulation. Unit is %.

Position\Energy	10 MeV	20 MeV	40 MeV
P0	2.25 ± 0.04	1.60 ± 0.06	1.20 ± 0.04
P9	2.03 ± 0.03	1.43 ± 0.10	1.09 ± 0.05

5.7.6 Intrinsic Resolution

The obtained resolution σ_E includes some factors to be worsened. The intrinsic resolution was written as:

$$\sigma_{intr}^2 = \sigma_E^2 - (\sigma_{noise}^2 + \sigma_{beam}^2 + \sigma_{col}^2), \quad (5.17)$$

where σ_{intr} , σ_{noise} , σ_{beam} , and σ_{col} are intrinsic energy resolution, error sources from pedestal noise, spread of LCS beam energy, and the radius of the collimator, respectively.

Electronics Noise

The influence of the pedestal noise on the energy resolution was evaluated with MC simulation as seen in Tab. 5.11.

Table 5.11: Deterioration of energy resolution by electronics noise. Unit is %.

Position \ Energy	10 MeV	20 MeV	40 MeV
P0	0.2	0.0	0.0
P9	0.1	0.0	0.0

LCS beam

The fluctuation of the Compton edge energy is 1%. However the fluctuation was already included the LCS spectrum to be convoluted. Therefore it may not be taken into account.

The horizontal size of electron bunch in TERAS is known to be from 1.55 mm to 2.2 mm. Fig. 5.35 shows the LCS beam spectra obtained by changing the bunch size. The fitting was performed with these spectra again. However the differences were not seen.

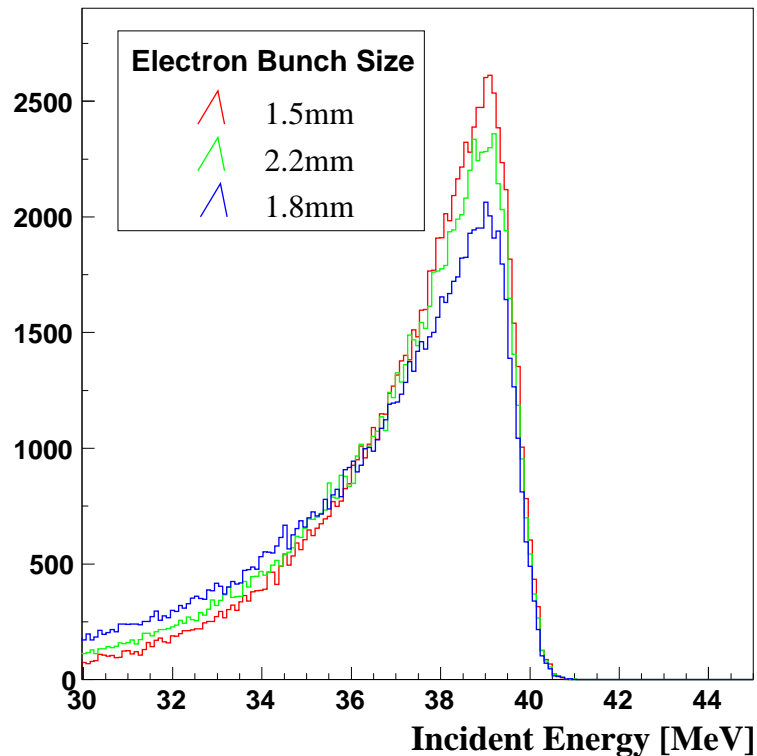


Figure 5.35: LCS beam spectra with various horizontal electron bunch size in TERAS.

Radius of Collimator

The radius of the collimator does not affect the shape of the Compton edge. Hence the resolution does not include the effect of collimator radius.

From above evaluations, contribution from the electronics noise was the most dominant for the energy resolution. The other sources σ_{beam} and σ_{col} were negligible. Because the similar noise is expected in the final detector, σ_{noise} should be taken into account to evaluate the performance for 52.8-MeV γ rays.

5.7.7 Systematic Error

Displacement of the second collimator and the spread of the LCS beam and indefiniteness of parameters in the MC simulation are considered to be systematic errors in the obtained energy resolution.

Collimator Displacement

The displacement of the second collimator can affect the energy resolution. Fig. 5.36 shows the LCS beam spectra for the collimator displacement ranging from 0 mm to 4 mm along x direction. By comparison with the measured spectrum in Fig. 5.30, it is guessed that the displacement should be 2.5 mm at most.

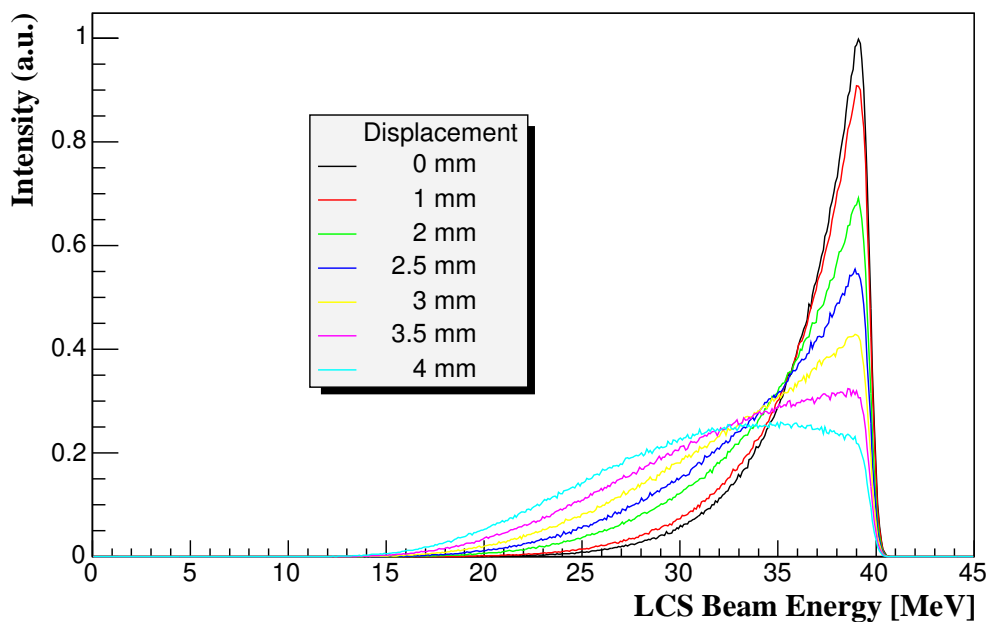


Figure 5.36: LCS beam spectra for collimator displacement of 0 mm to 4 mm. Compton edge energy is 40 MeV.

Assuming the true incident position was shifted by ± 2.5 mm at most, the LCS spectrum was regenerated by the simulation to fit with the convolution again. The result is shown in Tab. 5.12.

In this beam test, whenever the energy of LCS beam was changed, the second collimator was rearranged. Therefore it is not possible that the collimator was shifted in every run. If the collimator was shifted, the Compton edge of the incident beam tended to be smeared as shown in Fig. 5.36 and the resolution might be better.

Table 5.12: Difference in energy resolution between collimator displacement of 0 mm and one of 2.5 mm. Unit is %.

Position \ Energy	10 MeV	20 MeV	40 MeV
P0	-0.2	-0.1	-0.1
P9	-0.1	-0.2	-0.2

Parameters in MC simulation

Effects by the miscalculation of QEs was evaluated with MC simulation in the same way as position resolution. The differences are shown in Tab. 5.13.

Table 5.13: Deterioration of the energy resolution by changing parameters in QE estimate. Unit is %.

Parameter	default value	range or value	Incident energy & position					
			10 MeV		20 MeV		40 MeV	
			P0	P9	P0	P9	P0	P9
n_{Xe}	1.62	1.56 to 1.72	0.1	0.0	0.0	0.0	0.1	0.0
λ_{sca}	45 cm	40 cm to 50 cm	0.1	0.1	0.1	0.1	0.0	0.0
λ_{abs}	90 cm	3 m	0.2	0.2	0.1	0.1	0.1	0.1
Reflection	0%	10%	0.2	0.2	0.2	0.2	0.1	0.2

From above evaluations, the combined errors are obtained as shown in Tab. 5.14.

Table 5.14: Combined systematic errors for energy resolution. Unit is %.

Position \ Energy	10 MeV	20 MeV	40 MeV
P0	+0.3 -0.4	+0.2 -0.3	± 0.2
P9	± 0.3	+0.2 -0.3	+0.2 -0.3

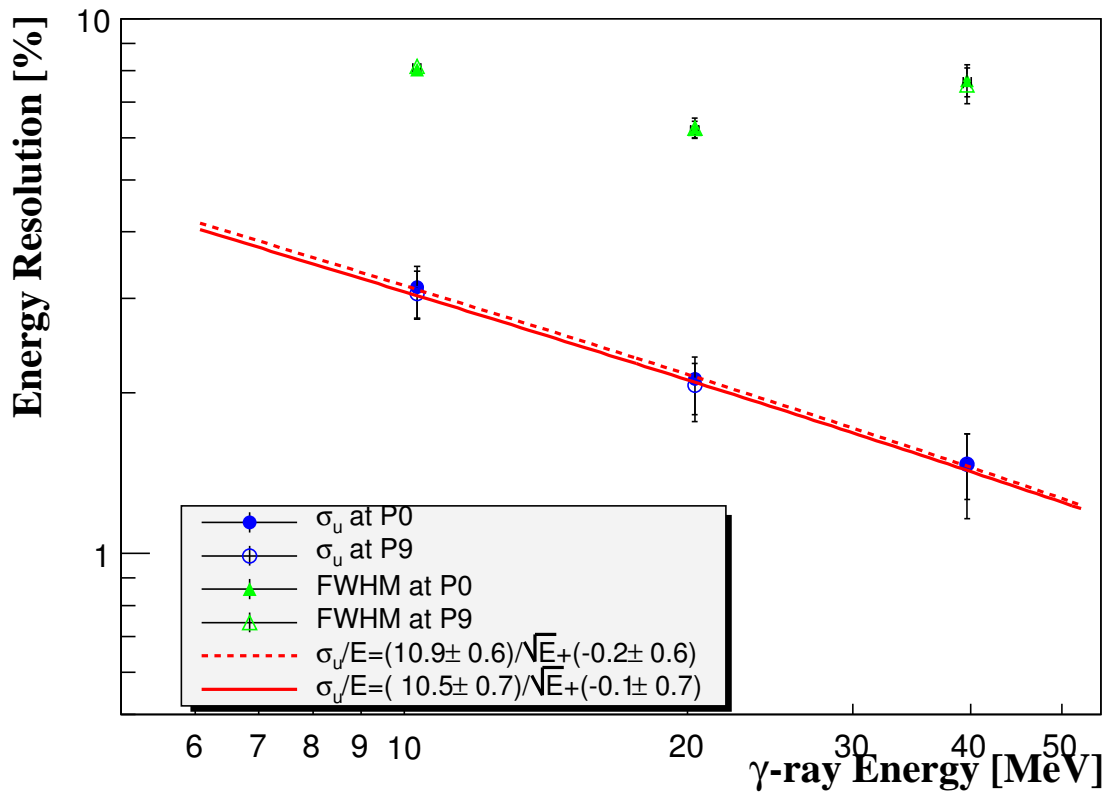
5.7.8 Energy Resolution

Taking systematic errors into account, we obtained the energy resolution as a function of γ -ray energy as follows:

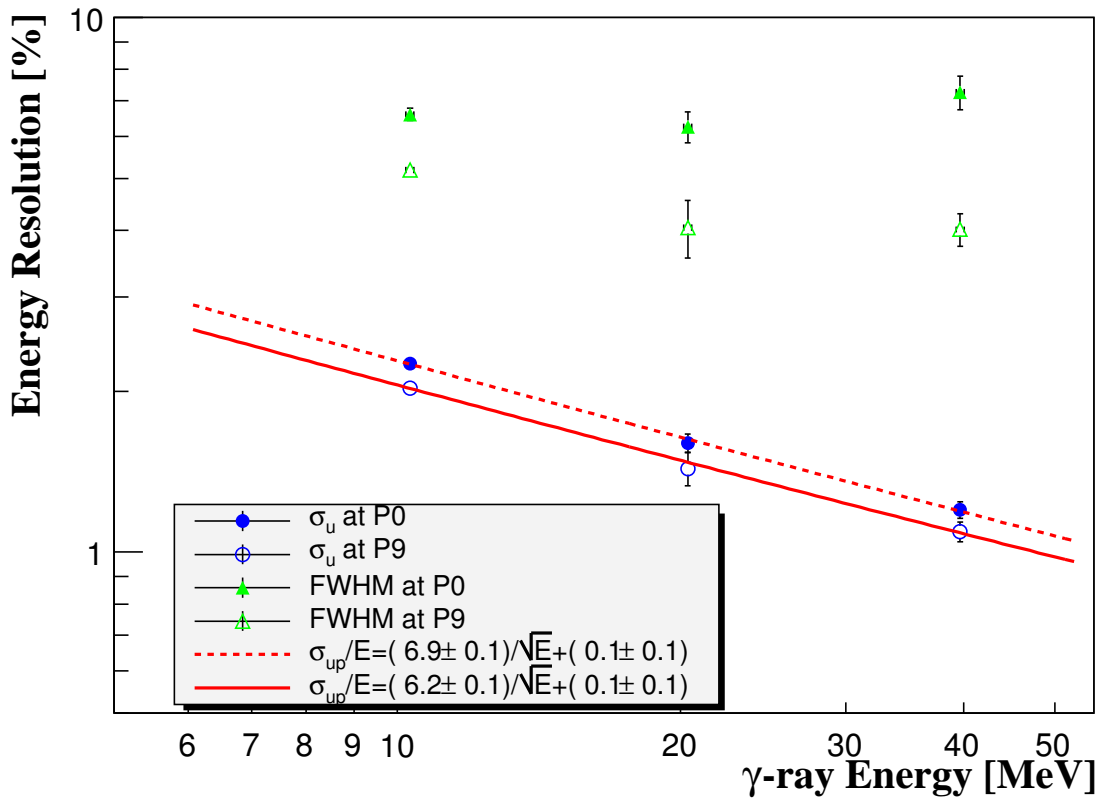
$$\text{P0 : } \frac{\sigma}{E} = \frac{(10.9 \pm 0.6)}{\sqrt{E}} + (-0.2 \pm 0.6) \quad (\%), \quad (5.18)$$

$$\text{P9 : } \frac{\sigma}{E} = \frac{(10.5 \pm 0.7)}{\sqrt{E}} + (-0.1 \pm 0.7) \quad (\%). \quad (5.19)$$

Fig. 5.37 shows the energy resolutions obtained in this section. For 52.8-MeV gamma rays, the energy resolution is expected to be 1.30% at P0 and 1.35% at P9, that is, 3.1% at P0 and 3.2% at P9 in FWHM. Those expected resolutions would be adequate when the MEG experiment was performed with the 100-liter prototype. The performance expected by the final detector will be discussed in the next chapter.



(a) measured data



(b) MC simulation

Figure 5.37: The energy resolution σ_u as a function of γ -ray energy.

5.7.9 Energy linearity

In order to verify the linearity of the detector response for γ rays from 10 MeV to 40 MeV, we plotted the relation between the Compton edge parameters obtained in the previous subsection and Compton edge energy estimated from ring and laser parameters. As shown in Fig. 5.38, the LXe detector has a good linearity. This is very strong point for γ -ray detector, and it serves energy calibration with a high precision.

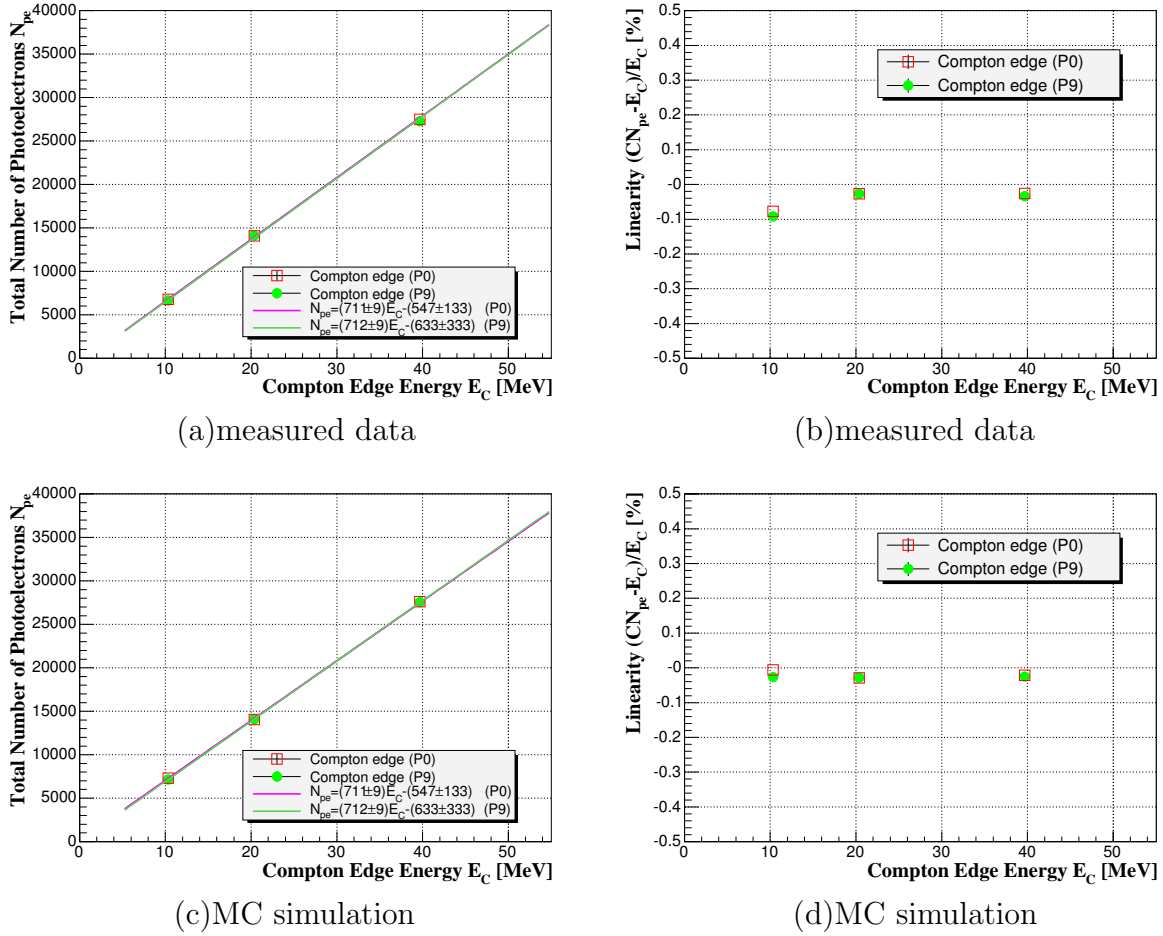


Figure 5.38: (a)(c) Incident LCS beam energy vs measured energy in N_{pe} . (b)(d) Energy linearity for data. C is a conversion factor from N_{pe} to MeV obtained from the fitting result of (a).

Chapter 6

Expected Performance

6.1 Expected Resolution

In this chapter we evaluate the performance of the final detector based on our analysis in Chap. 5. Before that, it is necessary to understand the difference between the 100-liter prototype and the final detector. The most different point in both detectors is the size and shape. Therefore the performance of the 100-liter prototype obtained in the LCS beam test cannot be extrapolated straightforward to the final detector. We have to take the difference into account. The criterion to connect with each other is considered to be an absorption length.

We will explain the relation between absorption length and energy resolution, join both detectors together, and then evaluate the performance of the final detector.

6.1.1 Effect of Absorption Length

In this section we discuss the impact of the absorption length on the performance of the LXe detector by estimating the energy resolution of the 100-liter prototype for 52.8 MeV γ rays that are expected from the $\mu^+ \rightarrow e^+ \gamma$ decays.

Simulations show that the determination of the incident positions of the γ rays is only slightly affected by absorption and Rayleigh scattering. On the contrary the energy resolution is heavily dependent on the absorption mainly because of fluctuations in light collection efficiency. For a short absorption length the total amount of light collected by the PMTs changes according with the event-by-event shower fluctuations. In the following we concentrate on energy measurement of γ rays.

For negligible absorption (i.e. $\lambda_{\text{abs}} \gg$ the detector size) the γ ray energy may be simply evaluated by the total sum of the photons collected by all the PMTs, possibly weighted by the local density of the PMTs. For a finite absorption length, however, a better method of summing the PMT outputs is necessary.

The γ ray energy E may be calculated as a linear sum of the PMT outputs q_i with arbitrary coefficients c_i :

$$E = c + \sum_i c_i q_i. \quad (6.1)$$

To optimize the coefficients we may use simulated events with the γ ray energy of E_t and minimize

$$\chi^2 = \langle (E - E_t)^2 \rangle, \quad (6.2)$$

where $\langle A \rangle$ is the average of A over the simulated events. The minimization is straightforward and yields the following result:

$$c_i = \mathbf{M}^{-1} (\langle E_t q_i \rangle - \langle E_t \rangle \langle q_i \rangle), \quad (6.3)$$

$$c = \langle E_t \rangle - \left\langle \sum_j c_j q_j \right\rangle. \quad (6.4)$$

Here \mathbf{M} is just the covariance matrix of q_i for the simulated events,

$$\mathbf{M}_{kl} \simeq \frac{N}{N-1} \langle (q_k - \langle q_k \rangle)(q_l - \langle q_l \rangle) \rangle. \quad (6.5)$$

This method is called “linear fit” and its validity is based on the principal component analysis [93].

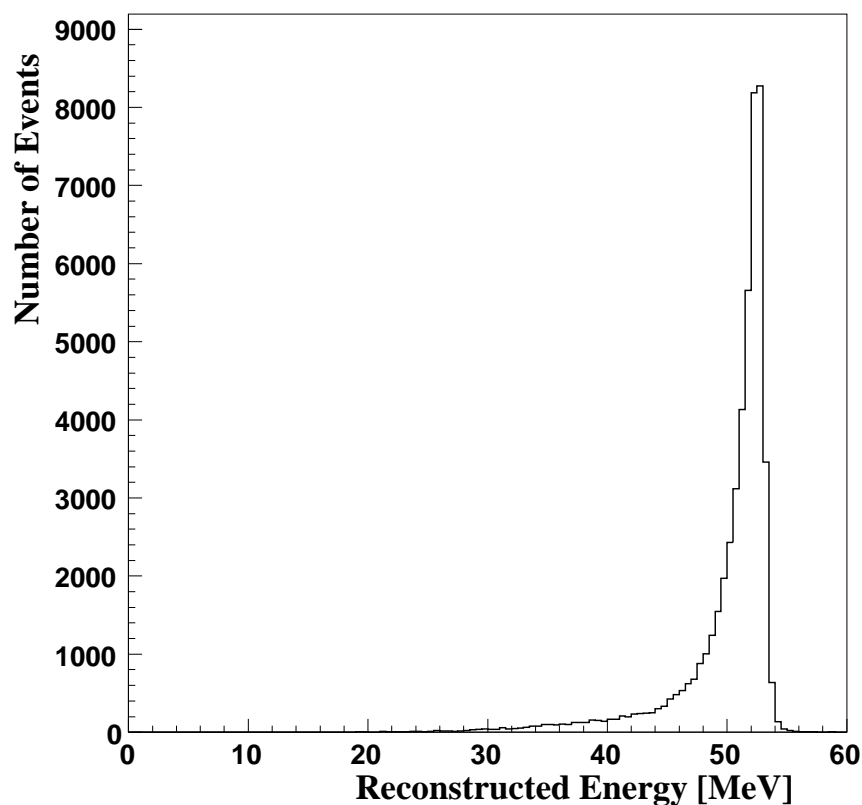


Figure 6.1: A reconstructed energy spectrum for 52.8-MeV γ rays by the linear fit.

Using the linear fit, a reconstructed energy spectrum for 52.8 MeV monochromatic γ rays that uniformly irradiate the center of the detector face is shown in Fig. 6.1. The spectrum has an asymmetric shape. The lower tail is caused by interactions of the γ rays in the materials before the LXe and by a leakage of shower components (mostly low energy γ rays). We emphasize again that the most important for the $\mu^+ \rightarrow e^+ \gamma$ experiment is the resolution at the upper edge (σ_u) to reject background events, while the lower tail concerns the detection efficiency. The spectrum was fitted to Eq. 5.14.

The obtained resolutions in FWHM and σ_u for 52.8 MeV γ rays are plotted in Fig. 6.2 as a function of the absorption lengths assumed in the simulation. The resolutions for two

incident positions P0 and P9 described in the inset of Fig. 6.2 are similar, indicating a small position dependence. The resolutions are also stable by changing $\lambda_{\text{Ray}} = 30 - 50$ cm and for $n = 1.57 - 1.72$ for LXe. Note that in the simulation refraction, reflection and absorption of the scintillation light at the PMT quartz windows are taken into account.

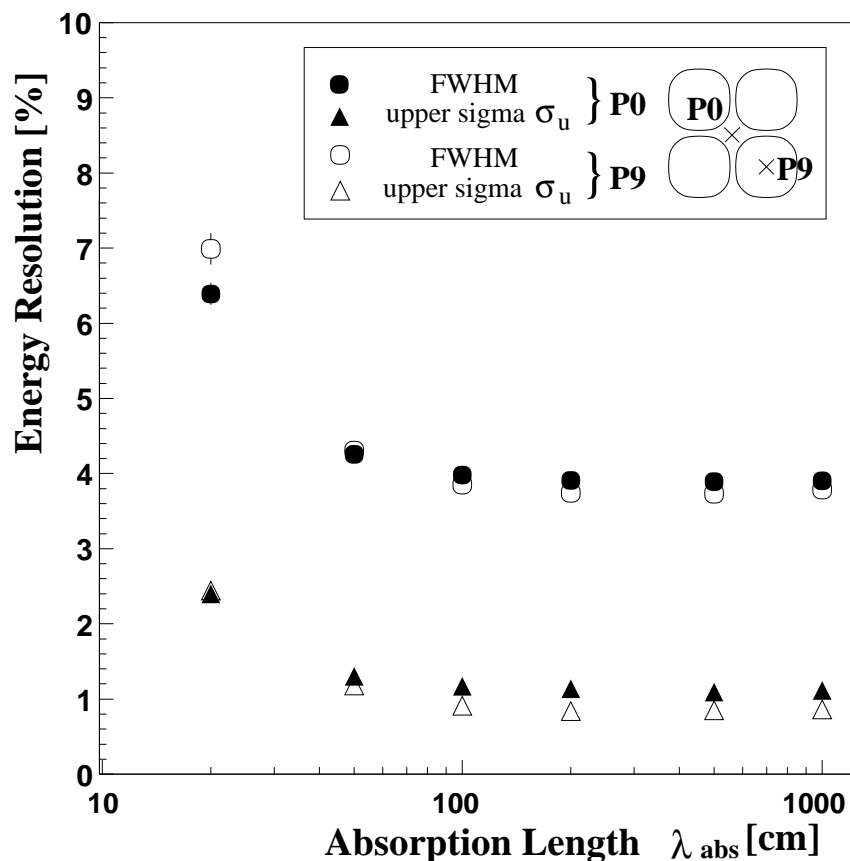


Figure 6.2: The expected energy resolutions for 52.8 MeV γ rays as a function of the absorption length. Resolutions at two incident positions, P0 and P9.

With the achieved absorption length of $\lambda_{\text{abs}} > 100$ cm an energy resolution of 4% FWHM and $\sigma_u/E \sim 1.2\%$, averaged over the detector acceptance, is expected from the MC simulation. The detection efficiency, if selected within $\pm 4\%$ around the energy peak, increases as λ_{abs} and for $\lambda_{\text{abs}} > 50$ cm it saturates at approximately 60%.

6.1.2 Energy Resolution

In order to evaluate the energy resolution for the final detector by using the energy resolution obtained in the LCS beam test, we have to take the absorption length and the detector shape into account.

Absorption Length

Fig. 6.3 shows the relation between the energy resolution and absorption length estimated with MC simulation for the final detector. Since the absorption length in the 100-liter prototype was 1 m at least, the energy resolution in the final detector is expected to be 5.0% in FWHM. Taking the lower tail in the energy spectrum into account, it is reasonable that FWHM corresponds to about four times the upper sigma when the absorption length is not so short as the depth of the detector. Furthermore we have to consider the deterioration of the resolution by pedestal noise, PMT stability, and so on. Even if the degree of the deterioration in the 100-liter prototype is scaled to the final detector, the deterioration is negligible as mentioned in Sec. 5.7. Consequently it is appropriate that the intrinsic energy resolution in the final detector is 5% (FWHM).

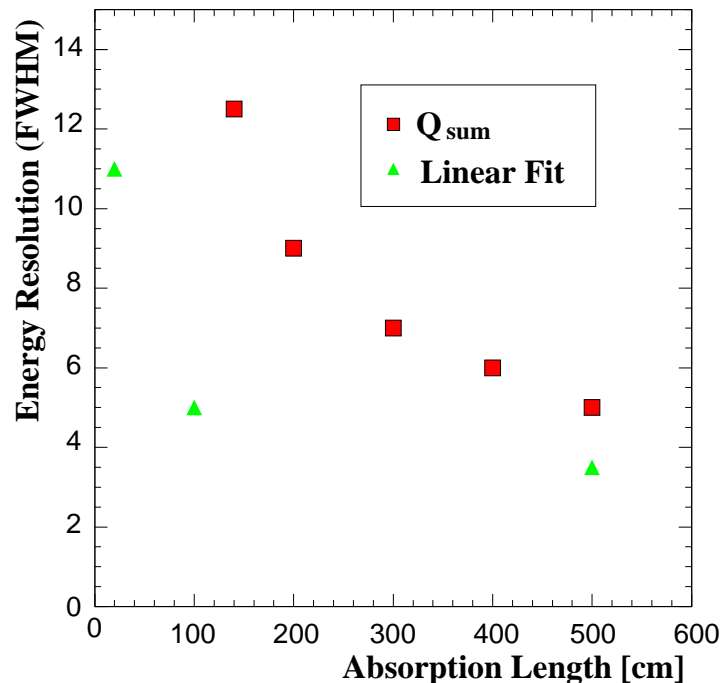


Figure 6.3: The energy resolution vs. absorption length in the final detector by MC simulation.

Curved Shape and Mask Analysis

The final detector has a different shape, a curved shape, from the 100-liter prototype. Especially the PMTs on the front face are arranged in a convex shape. Because of this it might not be appropriate to extend the obtained detector performance to estimate the final detector one. For studying this effect without relying on MC simulation but only using real data other kinds of analysis have been performed by masking several PMTs in the 100-liter prototype at the stage of data analysis by hand.

For simulating the convex shape, an analysis was done by using only 4×4 PMTs on the front face and all PMTs on the other faces. Calibration and fitting procedures are

same as standard analysis. The result shows that the energy resolution does not change significantly.

The curved shape effect was simulated by masking all PMTs on lateral face(s) similarly. It was found that the observed number of photoelectrons decreases naturally and that the energy resolution deteriorates accordingly up to 3% in sigma. However it is not statistical but seems to be position dependent on the first conversion point, indicating that we can restore the resolution by applying certain intelligent algorithm. Note that this is really an extreme case and in the final detector those light discarded in this analysis can be detected by some PMTs as far as the absorption length is long enough.

If the lateral faces are removed from the 100-liter prototype, it can be a simple simulation for the final detector. Actually the depth of the effective volume in both detectors is about 50 cm. Therefore the 100-liter prototype such that the bottom and top face was masked is considered the final detector. The estimate of energy resolution with masked faces is what we call “mask analysis”.

By fitting the data such that $E_C = 10 \text{ MeV} - 40 \text{ MeV}$ and impinging position is P0 and P9, we estimated the energy resolution for the final detector. The fitting procedure is the same as done in Sec. 5.7. The result is shown in Fig. 6.4 and Tab. 6.1. From this result, the energy resolution for 52.8 MeV is estimated to be 2.2% in σ_u at both P0 and P9.

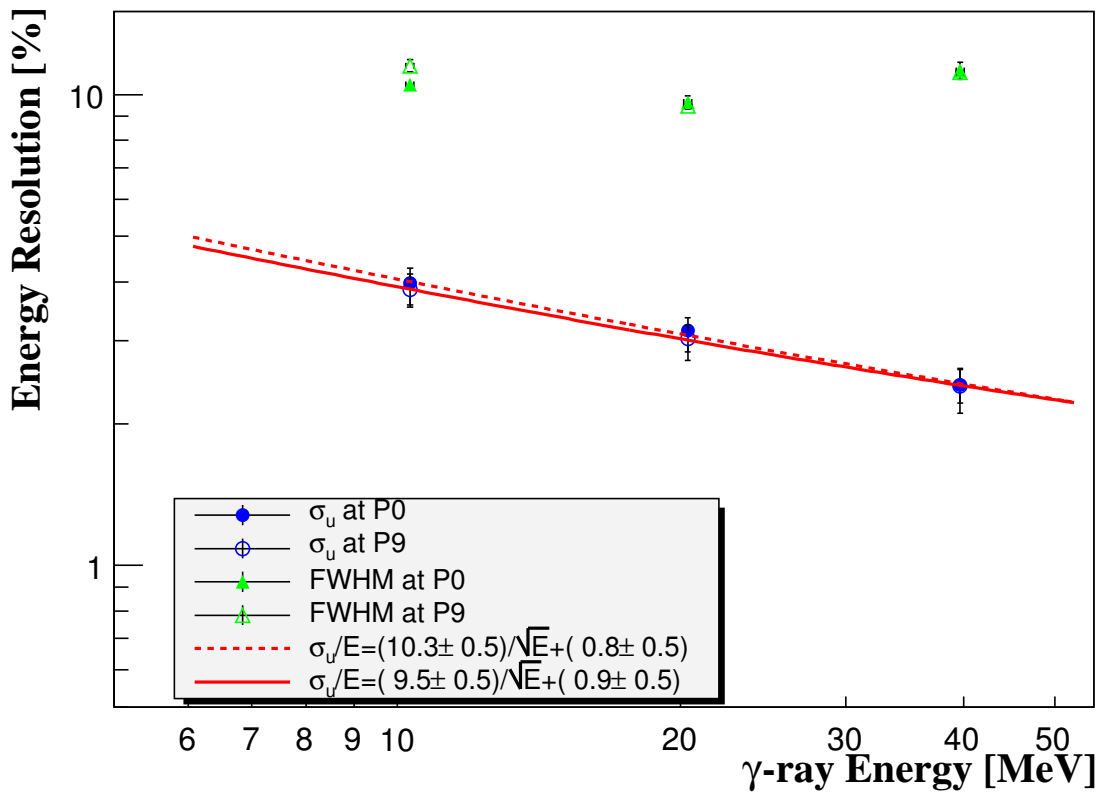


Figure 6.4: Energy resolution by mask analysis.

The frontage of the final detector is 2-PMT(= 12.4 cm) longer than one of the 100-liter

Table 6.1: Energy resolution by mask analysis. Error bars include only statistical errors. Unit is %.

Position\Energy	10 MeV	20 MeV	40 MeV
P0	3.98 ± 0.05	3.15 ± 0.06	2.42 ± 0.05
P9	3.85 ± 0.08	3.03 ± 0.06	2.41 ± 0.01

prototype. In order to study the influence of the number of PMTs on the front face on the energy resolution, we used only 4×4 PMTs as to the front face. The obtained energy resolution was 1.9% in σ_u .

Thus the performance of the final detector is comparable to one of the 100-liter prototype and we can employ the result of the 100-liter prototype to evaluate the performance of the final detector. The energy resolution in the final detector is expected to be 2.2% in sigma, that is, 5.2% in FWHM.

6.1.3 Position Resolution

In the method with local weighted mean, the position reconstruction is performed with several PMTs (typically 4~10 PMTs). The position reconstruction for the final detector is in a similar situation. Therefore the position resolution is not different between the 100-liter prototype and the final detector. The position resolution in the final detector is expected to be 9.9 mm to 11.0 mm for narrow components and 25.9 mm to 45.8 mm for broad components in FWHM, which is conservatively from the worse result for 40-MeV γ rays impinged at P0 and P9.

6.1.4 Timing Resolution

The timing resolution in the 100-liter prototype for 52.8 MeV γ rays was already estimated to be 76 psec in sigma by a beam test with low energy electron beam [94]. Since it is only measured value, we employ 76 psec as the timing resolution to evaluate the performance of the final detector.

6.1.5 Efficiency

In the MEG experiment the COBRA magnet exists in front of the LXe detector and photons have to traverse its wall. In order to simulate this situation, data was taken with several kinds of material located in front of the 100-liter prototype, just behind the 2nd collimator. Five kinds of material were placed to study the effect systematically. They were 5mm, 10mm, 15mm thick aluminum, 15mm thick aluminum with 4mm thick steel, and 5mm thick lead. The corresponding radiation lengths were $0.053X_0$, $0.11X_0$, $0.16X_0$, $0.398X_0$, and $0.89X_0$ respectively. As indicated by MC simulation study, the resolution does not deteriorate but only efficiency is lost because of additional material. Actually analysis was applied on these data and this point has been confirmed. Note that the COBRA magnet thickness is $0.197X_0$ and material used in the 100-liter prototype for honeycomb window and PMT holders and so on is close to those of the final detector.

Fig. 6.5 shows the selection efficiency in the 100-liter prototype. It is found that the selection efficiency is 44.6% for incidence at P0, 43.3% for incidence at P9, and 40.1% for all over front face. Furthermore the efficiency becomes 30% with an energy selection within $\pm 4\%$ around the energy peak by the linear fit.

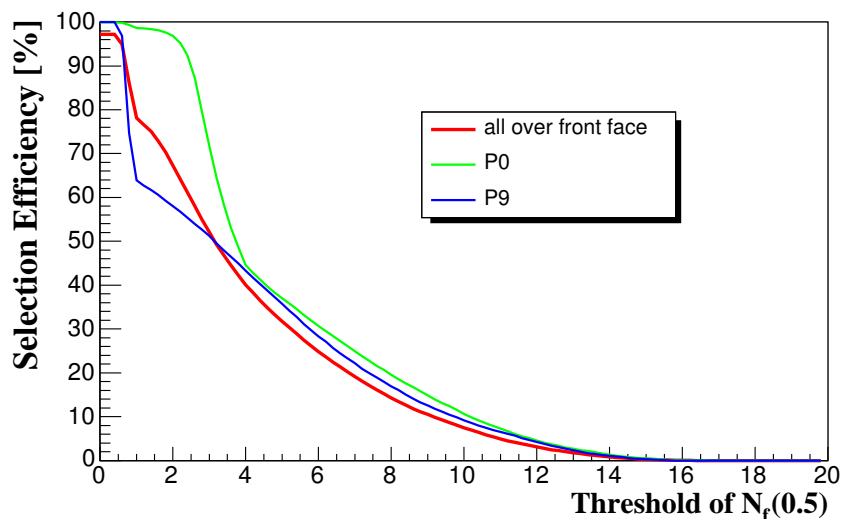


Figure 6.5: Selection efficiency as a function of $N_f(0.5)$.

6.2 Backgrounds and Sensitivity

The following estimation is based on the assumption and calculation in [1, 2].

First we estimated the single event sensitivity. The detector acceptance defined by the positron spectrometer and the LXe detector is $0.08 < |\cos \theta| < 0.35$ and $-60^\circ < \phi < 60^\circ$, amounting to $\Omega/4\pi = 0.09$. We assume a detection efficiency for the photon (ε_γ) of 30%. For the positron we assume $\varepsilon_e \sim 90\%$. The single event sensitivity is defined as the $\mu \rightarrow e\gamma$ branching ratio for which the number of expected decays is equal to one. Assuming a muon stop rate of $N_\mu = 5.8 \times 10^7/\text{s}$, which is conducted in Subsec. 6.2.3, and a total running time of the experiment $T = 5.2 \times 10^7$ s (2 years). The single event sensitivity for MEG experiment is calculated as

$$B(\mu^+ \rightarrow e^+\gamma) = \frac{1}{N_\mu \cdot T \cdot (\Omega/4\pi)} \times \frac{1}{\varepsilon_e \cdot \varepsilon_\gamma \cdot \varepsilon_{sel}} \quad (6.6)$$

$$= 1.8 \times 10^{-14}, \quad (6.7)$$

where ε_{sel} is the efficiency of the event selection. Selection cuts covering 70% of the signal (1.4 FWHM for Gaussian distributions) are considered to be applied on the reconstructed positron energy, on the e^+/γ relative angle and timing.

This sensitivity can be converted to 90% confidence level upper limits, in case of no signal observed, by using the background rate estimates given in the following subsection. In MEG experiment two major backgrounds are taken into account:

- (1) prompt background from radiative muon decays ($\mu^+ \rightarrow e^+ \nu_e \bar{\nu}_\mu \gamma$),
- (2) accidental background ($\mu \rightarrow e \nu_e \bar{\nu}_\mu + \text{random } \gamma$).

In order to evaluate the number of background events, the detector performances were assumed as seen in Tab. 6.2.

Table 6.2: Expected detector performances. Every values are in FWHM.

LXe detector		
Resolution	unit	Value
Energy	%	5.2
Timing	psec	179
Position(x)	mm	9.9 ~ 11.0 (narrow component)
		25.9 ~ 45.8 (broad component)
Positron Spectrometer		
Resolution	unit	Value
Energy	%	0.8
Timing	psec	100
Position	mrad	10.5
Muon Beam		
Resolution	unit	Value
Muon decay position	mm	2.1

6.2.1 Prompt Background

The prompt background was calculated using the formula given in [95,96]. By numerical integration over the selection cuts (1.4 FWHM for each selection variable) we find a background of 3.1×10^{-15} events per muon decay. As described in the following subsections, this rate is smaller than the accidental background rate. In this estimation the prompt background is not considered.

6.2.2 Accidental Background

For simplicity, the normalized e^+ and photon energies, which are defined by $x = 2E_e/m_\mu$ and $y = 2E_\gamma/m_\mu$, will be used, where m_μ is a muon mass. Further, it is assumed that δA and ΔA are taken to be a half width and a full width of the signal box for the observable A respectively.

The effective branching ratio of the accidental background (B_{acc}) can be derived. First of all, a number of the accidental background events (N_{acc}) are given by

$$N_{acc} = (N_\mu \cdot f_e^0 \cdot \frac{\Omega}{4\pi} \cdot \varepsilon_e) \cdot (N_\mu \cdot f_\gamma^0 \cdot \frac{\Omega}{4\pi} \cdot \varepsilon_\gamma) \times (\frac{\delta\omega}{\Omega}) \cdot (2\delta t) \cdot T \cdot f_{P_\mu}, \quad (6.8)$$

where δt is a timing coincidence resolution. f_e^0 and f_γ^0 are the fractions of the spectrum within the signal box of the e^+ s in the Michel muon decay and photons in the radiative muon decay respectively. They include their branching ratios. f_{P_μ} is a background suppression factor when a muon is polarized [97]. $f_{P_\mu}=1$ is considered from now on. The effective branching ratio for accidental background can be obtained by dividing Eq.(6.8) by the product of a total number of muons and the detector acceptance given by

$$B_{acc} = \frac{N_{acc}}{N_\mu \cdot T \cdot (\Omega/4\pi) \cdot \varepsilon_e \cdot \varepsilon_\gamma}. \quad (6.9)$$

For unpolarized muons, B_{acc} becomes

$$B_{acc} = N_\mu \cdot f_e^0 \cdot f_\gamma^0 \cdot (\frac{\delta\omega}{4\pi}) \cdot (2\delta t) \quad (6.10)$$

Estimation of f_e^0

f_e^0 is obtained for a given δx by integrating the Michel muon spectrum (N_{michel}) from $1 - \delta x$ to 1.

$$\begin{aligned} f_e &= \int_{1-\delta x}^1 dx N_{michel} \frac{d(\cos \theta_e)}{2} \\ &= \int_{1-\delta x}^1 dx \left[2x^2 \left((3 - 2x) + 2x^2(2x - 1)P_\mu \cos \theta \right) \right] \frac{d(\cos \theta_e)}{2} \\ &\approx 2(\delta x) \end{aligned} \quad (6.11)$$

Estimation of f_γ^0

To estimate f_γ^0 , the radiative muon decay ($\mu^+ \rightarrow e^+ \nu_e \bar{\nu}_\mu \gamma$) is considered as a source of 52.8 MeV photon. The differential decay width is integrated over the e^+ energy and the angle between e^+ and photon ($\theta_{e\gamma}$). After the integration of e^+ energy and $\theta_{e\gamma}$, the differential branching ratio for $y \sim 1$ and any value of x is given by [97]

$$dB_{acc}(\mu^+ \rightarrow e^+ \nu \bar{\nu} \gamma) \approx J(y) \cdot (1 + P_\mu \cos \theta_\gamma) dy d \cos \theta_\gamma \quad (6.12)$$

where $J(y)$ is given by

$$J(y) = \frac{\alpha}{2\pi} (1 - y) \left[\ln \frac{(1 - y)}{r} - \frac{17}{6} \right] \quad (6.13)$$

The rate can be estimated by integrating the spectrum over the width of the signal region. The partial branching ratio (denoted by f_γ) integrated over the signal region ($1 - \delta y \leq y \leq 1$) can be given from Eq.(6.12) by

$$\begin{aligned} f_\gamma &= \int_{1-\delta y}^1 dy \frac{dB(\mu^+ \rightarrow e^+ \nu \bar{\nu} \gamma)}{dy} \\ &\approx \left(\frac{\alpha}{2\pi} \right) (\delta y)^2 \left[\ln(\delta y) + 7.33 \right] (1 + P_\mu \cos \theta_\gamma) \frac{d(\cos \theta_\gamma)}{2} \end{aligned} \quad (6.14)$$

From Eq.(6.14), it is shown that f_γ is roughly proportional to $(\delta y)^2$. Now, f_γ^0 that does not include the angular dependence is given by

$$\begin{aligned} f_\gamma^0 &= \left(\frac{\alpha}{2\pi}\right)(\delta y)^2 [\ln(\delta y) + 7.33] \\ &= 1.16 \times 10^{-3}(\delta y)^2 [\ln(\delta y) + 7.33] \end{aligned} \quad (6.15)$$

Estimation of $\delta\omega$

Given the angular resolution $\delta\theta_{e\gamma}$, the back-to-back resolution ($\delta\omega$) is presented by

$$\delta\omega = \frac{\pi(\delta\theta_{e\gamma})^2}{4\pi} = \frac{(\delta\theta_{e\gamma})^2}{4}. \quad (6.16)$$

Net expression of accidental background

From the above, the effective branching ratio of accidental background is given by

$$B_{acc} = R_\pi \cdot (2\delta x) \cdot \left[\frac{\alpha}{2\pi}(\delta y)^2(\ln(\delta y) + 7.33)\right] \times \left(\frac{\delta\theta^2}{4}\right) \cdot (2\delta t), \quad (6.17)$$

$$\propto \delta E_e \cdot \delta t_{e\gamma} \cdot (\delta E_\gamma)^2 \cdot (\delta\theta_{e\gamma})^2, \quad (6.18)$$

where only radiative muon decays are considered as a source of photons. The detail estimation of the accidental background including contributions from annihilations in flight and photon pile-ups by using the present apparatus will be given later.

Inclusive Photon Yield

The inclusive photon yield per muon decay $g_\gamma(y)$ ($y \equiv 2E_\gamma/m_\mu$) was evaluated in [2] by taking into account the following sources of photons:

- photons from radiative muon decays;
- photons from annihilation-in-flight;
- photons from positron interactions with surrounding materials;
- neutron induced background.

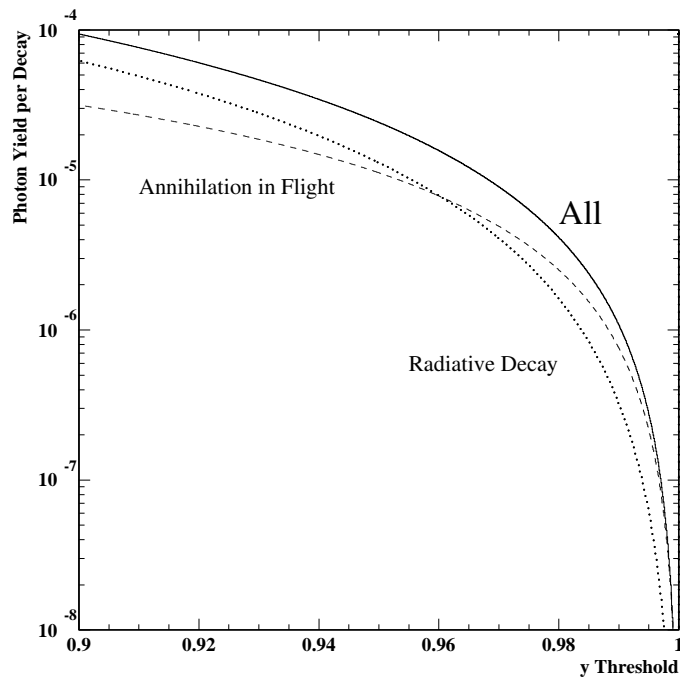
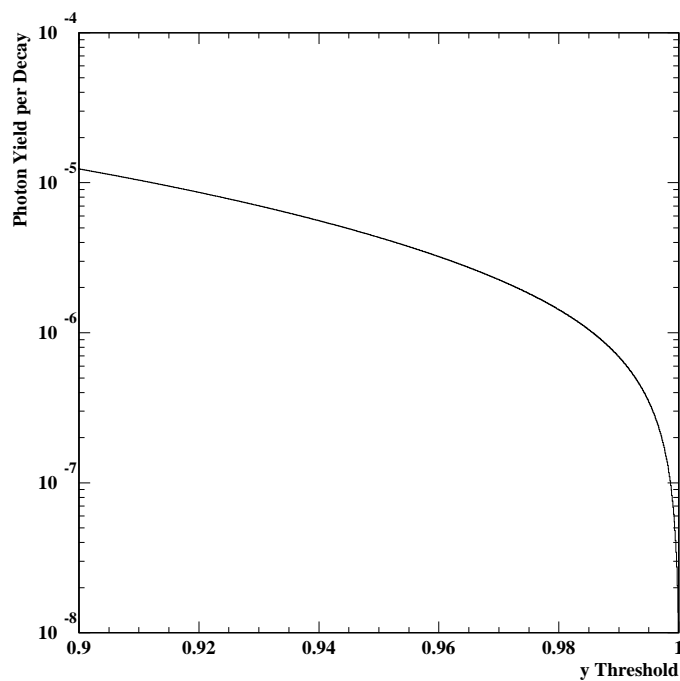
The integrated yield $f_\gamma(y) = \int_y^1 dy' g_\gamma(y')$ is plotted in Fig. 6.6. The rate of two photon pile-up can be written as:

$$g_{\gamma\gamma}(y) = \int_0^y dy' g_\gamma(y') g_\gamma(y - y') \eta(y', y - y'), \quad (6.19)$$

where $\eta(y_1, y_2)$ is the pile-up rejection factor for two photons with energy fractions y_1 and y_2 , and $0 < y < 2$. It depends on $\Delta\Omega_{\gamma\gamma}$ and $\Delta t_{\gamma\gamma}$ which define the two-photon separation power in solid angle and in time respectively, and are dependent on the energies of the photons. They are evaluated by MC simulations [2].

The pile-up spectrum $g_{\gamma\gamma}(y)$ is then integrated from $(1 - \delta y)$ to $(1 + \delta y)$, $f_{\gamma\gamma}(y) = \int_{1-\delta y}^{1+\delta y} dy' g_{\gamma\gamma}(y')$, where $y \equiv 1 - \delta y$. The resulting integrated pile-up photon rate $f_{\gamma\gamma}(y)$ is shown in Fig. 6.7.

The rate of accidental coincidences of Michel positrons with random photons given by $f_\gamma(y) + f_{\gamma\gamma}(y)$ is obtained by numerical integration over the selection cuts.

Figure 6.6: Integrated photon yield per muon decay $f_\gamma(y)$.Figure 6.7: Integrated pile-up photon yield per muon decay $f_{\gamma\gamma}(y)$.

6.2.3 90% C.L. Sensitivity

To simplify the calculation of B_{acc} , the accidental background rate estimated in [2] was scaled by using Eq. 6.18 and $B_{acc} \propto N_{\mu}^2$. The muon stop rate should be optimized since lower beam intensity reduces the accidental background rate. We obtain the relation between the muon stop rate and 90% confidence level upper limit as shown in Fig. 6.8. We find an accidental background of 8.9×10^{-14} events per muon decay with a stopping muon rate of 5.8×10^7 /s. However it is expected that 4.9 accidental background events are found with a 90% C.L. sensitivity of 1.2×10^{-13} .

Practically the number of expected backgrounds should be set to 0.5. Then an accidental background of 2.6×10^{-14} events per muon decay with a stopping muon rate of 2.1×10^7 /s is obtained. The 90% confidence level upper limit becomes 1.5×10^{-13} . Since this evaluation is based on the conservative values and some improvements in LXe detector are expected in the MEG experiment as described in later sections, the sensitivity will achieve an order of 10^{-13} .

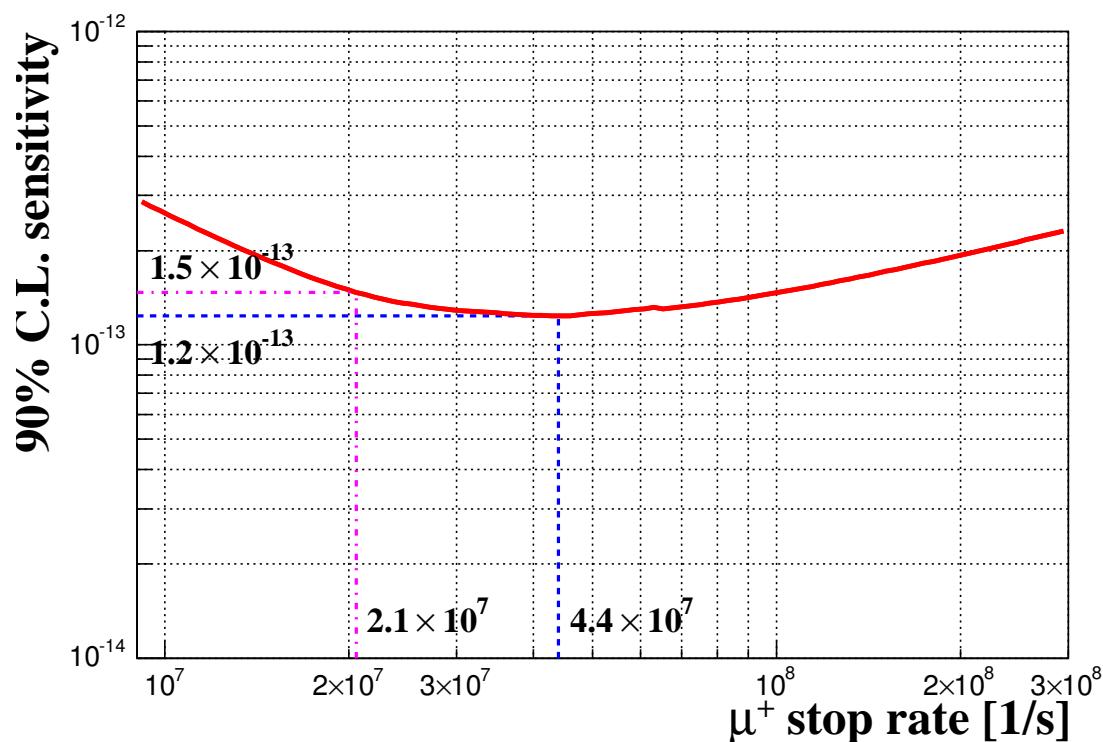


Figure 6.8: The relation between the muon stop rate and the 90% C.L. sensitivity.

6.3 Decay Angular Measurement

If the $\mu \rightarrow e\gamma$ events could be discovered, the MEG experiment would shift to the next stage. The angular distribution of $\mu^+ \rightarrow e^+\gamma$ with respect to the muon-polarization direction would give information to discriminate among various models, because different theoretical models predict a different helicity of e^+ in $\mu^+ \rightarrow e^+\gamma$ [95]. For polarized

muons, the angular distribution of positron from $\mu^+ \rightarrow e^+\gamma$ decay with respect to the direction of μ^+ spin direction is expressed by

$$\frac{dN(\mu^+ \rightarrow e^+\gamma)}{d\cos\theta_e} \propto Br(\mu^+ \rightarrow e^+\gamma) \times (1 + AP_\mu \cos\theta_e) \quad (6.20)$$

where N is the number of observed $\mu^+ \rightarrow e^+\gamma$ events, Br is the branching ratio of $\mu^+ \rightarrow e^+\gamma$, P_μ is the muon-spin polarization, θ_e is the angle between the muon spin and the positron, and A is asymmetric parameter as follows

$$A = \frac{|A_L|^2 - |A_R|^2}{|A_L|^2 + |A_R|^2}, \quad (6.21)$$

A_R and A_L are coupling constants.

There are three SUSY models to be discriminated by measuring the angular distribution: The SU(5) SUSY-GUT model predicts $A = +1$, yielding a $(1 + P_\mu \cos\theta_e)$ distribution. The SO(10) SUSY-GUT model predicts $A \approx 0$, yielding an almost uniform angular distribution. Minimal Supersymmetric extension of the Standard Model (MSSM) with ν_R model predicts $A = -1$, yielding $(1 - P_\mu \cos\theta_e)$ distribution. Hence it is possible that these models are clearly discriminated if the signals are observed.

The backgrounds for this measurement are the same as the $\mu \rightarrow e\gamma$ decay search. The prompt background obeys $(1 + P_\mu \cos\theta_e)$ distribution and the accidental background obeys $(1 + P_\mu^2 \cos^2\theta_e)$ distribution.

Here assuming that the $Br(\mu^+ \rightarrow e^+\gamma)$ is 10^{-12} and A is $+1$, muon decay events were generated to count the number of backgrounds and $\mu^+ \rightarrow e^+\gamma$ signals. The detector configurations and performances were set to the same values as those in Sec. 6.2. The polarization P_μ was set to 97% as a realistic value although it could be 100% in principle. The muon stop rate was set to a higher rate than the simple $\mu \rightarrow e\gamma$ search, 3×10^8 , because this measurement requires as many of statistics as possible.

There are two free parameter in this analysis: Asymmetry parameter ranging -1 to $+1$ and $\log_{10} Br$ ranging -13 to -11 . The parameter space of A vs. $\log_{10} Br$ was divided into 200×200 bins. In each bin, $|\cos\theta_e| < 0.35$ was divided into 4 bins to count the number of backgrounds and signals observed there. For each 200×200 bin, χ^2 for Poisson-distributed data [98] was calculated.

$$\chi^2 = \sum_{i=1}^4 \left[2(N_i^{obs} - N_i^{exp}) + N_i^{obs} \ln \left(\frac{N_i^{obs}}{N_i^{exp}} \right) \right], \quad (6.22)$$

where N^{obs} and N^{exp} are the observed and theoretical contents of the i -th bin.

Fig. 6.9 shows the 68%, 90%, and 95% C.L. sensitive region. It is found that $A = -1, 0, +1$ are distinguishable for $Br(\mu^+ \rightarrow e^+\gamma) > 10^{-12}$ with muon stop rate of 5.8×10^7 for 2 years. This measurement requires a large quantity of muon decay events. For that purpose, raising the muon stop rate brings a significant result. Alternatively a spin rotator might be introduced to enable us to select $\theta_e \pm 1$ according to the expected theoretical model, although it requires re-arrangement of the beam line.

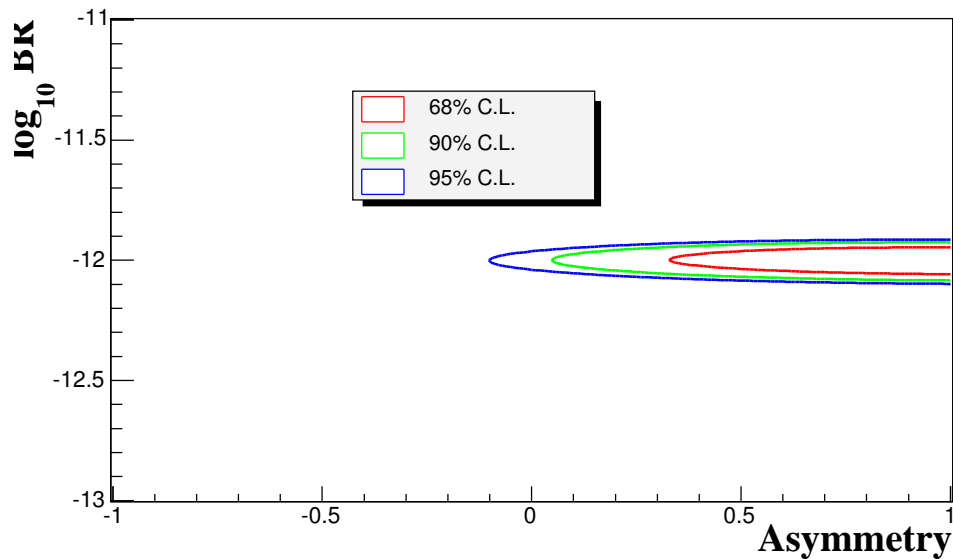


Figure 6.9: The sensitive region for the decay angular measurement with an assumption of SU(5) SUSY-GUT and $\text{Br}(\mu^+ \rightarrow e^+ \gamma) > 10^{-12}$.

6.4 Prospects for Further Improvements of Performance

In this section we discuss prospects for further improvements of the performance of the LXe detector.

6.4.1 New PMT

The PMTs (R6041Q) used in the 100-liter prototype have the low QE and the distribution of the values of QEs is rather broad as shown in Fig. 5.12.

In the R6041Q Rb-Cs-Sb is used as a photo-cathode material, but the cathode sensitivity of this material is not so high for Xe scintillation (178 nm). A Mn layer used between the photo-cathode and the quartz window to keep the surface conductivity of the photo-cathode at low temperature may possibly absorb some part of the scintillation photons before reaching photo-cathode layer. This might also be responsible for the low QE of the R6041Q. Moreover, it is not so easy to control the thickness of the Rb-Cs-Sb and the Mn layers due to technical difficulties in the evaporation procedure of these materials. This possibly cause the broad distribution of the QEs.

Recently new type of PMT (R9288) has been developed to overcome these problems in the R6041Q (Fig. 6.10). More standard bi-alkali, K-Cs-Sb is used as photo-cathode in this model. K-Cs-Sb has a higher cathode sensitivity and it is easier to control the thickness in the evaporation procedure as compared with Rb-Cs-Sb. Al strip pattern is coated on the quartz window to keep the surface conductivity at low temperature instead of a Mn layer. The strip pattern is designed to fit with the support structure of the dynodes to minimize the influence of the photon absorption in the Al strips.

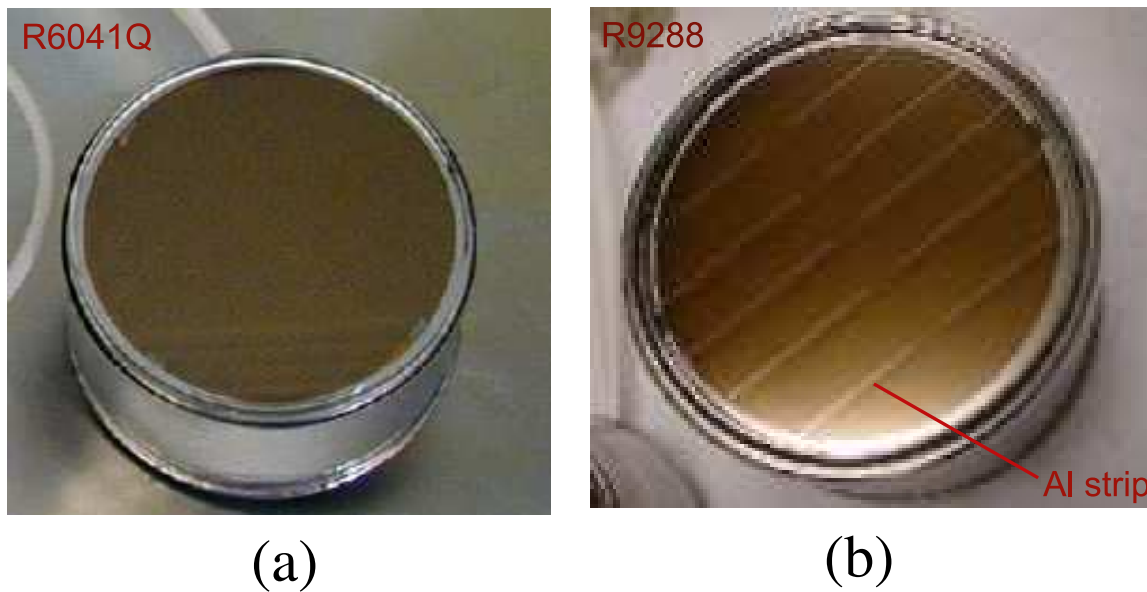


Figure 6.10: Two types of PMTs: (a) R6041Q with Rb-Cs-Sb and Mn layers and (b) new type (R9288) with K-Cs-Sb and Al strips.

The QEs of the R9288 have been recently measured. The preliminary results show that their QEs are 3 – 4 times higher compared with the QEs of the R6041Q. We can expect better energy resolution by using the R9288 in the LXe detector because the resolution is thought to be predominantly governed by the statistics of the number of photoelectrons.

6.4.2 Waveform Analysis

Capability of rejecting the pile-up background is quite essential for the γ -ray detector in the MEG experiment. The distribution of the PMT outputs enables us to reject the pile-up of accidental γ rays that are well separated spatially. Even pile-ups that are not separated spatially can be rejected by analyzing the waveforms of the PMT outputs. In the 100-liter prototype, ADCs and TDCs were used to read the PMT outputs, while in the final detector all the PMTs will be read with high-speed waveform digitizers. A fast analog sampling chip based on a switched capacitor architecture is being developed at PSI: The Domino Ring Sampling chip [99] for this experiment. The sampling speed is variable between 0.5 GHz and 2.5 GHz. It will be implemented not only for the readout of the LXe detector but also for the readout of the drift chamber system and the timing counters.

The principle of the operation of the DRS is illustrated in Fig. 6.11. The sampling frequency in the GHz range is generated with a series of inverters. A sampling signal propagates through these inverters freely (domino principle). Additional AND gates allow to stop the domino wave in any cell by an external trigger signal. The domino wave runs continuously in a circular fashion. Once a signal is stored, it is read out by a shift register at a clock speed of 40MHz and digitized externally by a flash ADC.

The prototype has been recently tested in the 100-liter prototype. The waveforms of the PMT signals from about 50-MeV γ rays were successfully taken at a sampling speed of 2.5 GHz. The typical waveform is shown in Fig. 6.12. The performance of the pile-up

rejection is being investigated with these data.

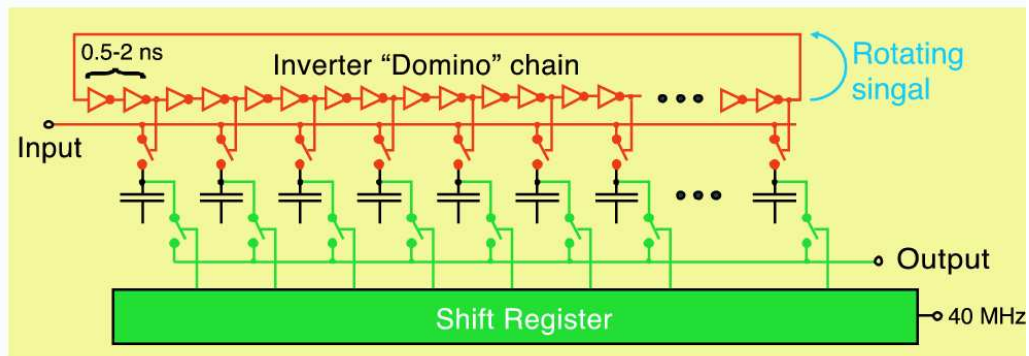


Figure 6.11: The principle of the operation of the DRS chip.

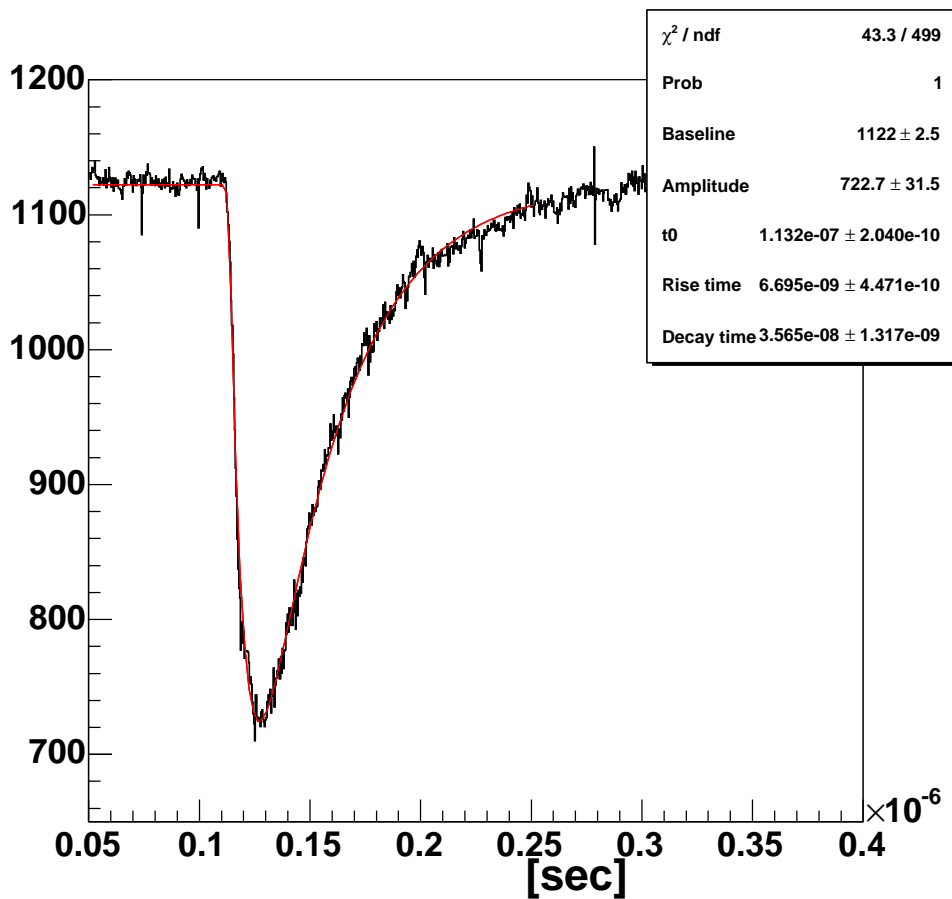


Figure 6.12: Typical waveform of PMT signal from about 50-MeV γ rays taken with the prototype of the DRS. A red curve is the best fit with two exponential function to the waveform data.

6.5 Calibration Method

In principle, calibration of the PMTs in the final detector will be done by using the same method employed in the prototype detector study. The gain will be periodically monitored and adjusted by using LEDs during the experiment. Individual PMTs will be tested before installation by measuring their gain and QE in a test vessel. To measure the resolution for a single photoelectron is essential to calibrate gain with precision. A relative estimate of the QE under the influence of the magnetic field is as important the gain adjustment. It is planned to use α sources on wires in LXe for monitoring and measuring QE.

For absolute energy calibration, 55-MeV and 83-MeV γ rays from $\pi^0 \rightarrow \gamma\gamma$ decays will be employed. Fig. 6.13 shows the schematic drawing of the calibration procedure. The γ -ray energy and the opening angle between two γ -rays have a correlation by the decay kinematics. If we require the opening angle is more than 175° , the energy spread of γ -rays is 0.3 MeV (FWHM), which is smaller than the energy resolution of LXe detector. In order to select the opening angle, γ -ray counter on the opposite of the LXe detector is required. NaI array counters are supposed to be used as the anti-counters. The anti-counters can face the target direction by moving to the upper and lower sides and tilting. If the π^- rate is 1×10^7 , the trigger rate is estimated to be $10\gamma/s$ in the region of $2\text{PMT} \times 2\text{PMTs}$ (about 150cm^2) on the incident face of the LXe detector. Assuming the number of PMTs on the incident face is 216, the calibration process takes one day if 30,000 events are required for each region.

It is also planned to perform absolute position calibration by using the meshed collimator equipped inside the magnetic wall. For absolute timing calibration the radiative muon decays will be used. At the early stage of the MEG experiment, absolute calibration with beam should take some more weeks.

As mentioned in Sec 5.1, a beam test for the 100-liter prototype was performed in πE1 area at PSI in 2004. In the LCS beam test the detector performance was evaluated for γ rays up to 40 MeV, whereas the CEX beam test employs monochromatic γ rays of 55 MeV, 83 MeV, 128 MeV to enable the performance evaluation for higher energy γ rays. One of the principal purposes in the CEX beam test was to estimate timing resolution. In the LCS beam test it was difficult to tag scattering electrons because there was little place to be set the tagging counter.

In this test, we replaced most of R6041Q with R9288s. It is expected that the increase of total number of photoelectrons improves the performance. Moreover some channels were prepared for waveform analysis with DRS chip as shown in Fig. 6.12.

We are now analyzing data taken in the CEX beam test and the result will be reported in 2005.

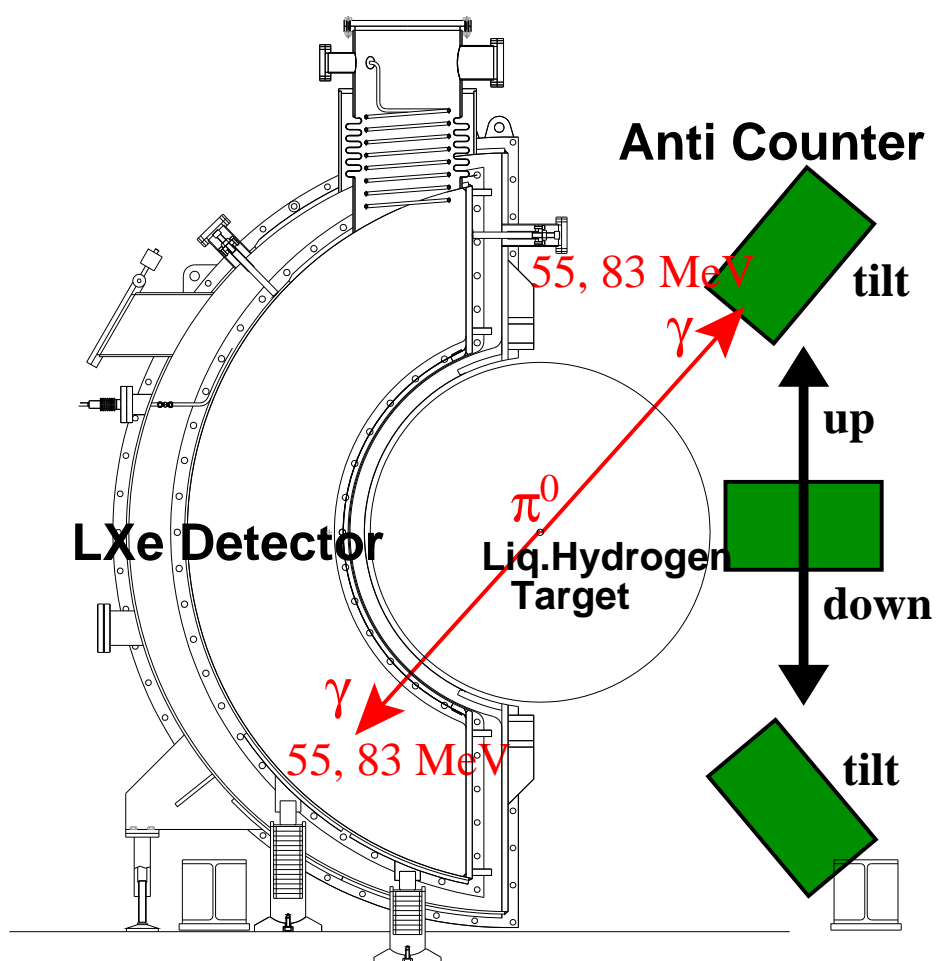


Figure 6.13: Schematic view of calibration with CEX beam.

Chapter 7

Conclusion

The 1000-liter liquid xenon scintillation detector is a key to the MEG experiment aiming at verifying theories beyond the SM like SUSY-GUT through searching for a lepton flavor violation signal, $\mu \rightarrow e\gamma$ decay. Since such a large detector has never been built before, we constructed a 100-liter prototype of the LXe detector to establish a stable operation and to evaluate the practical performance for 52.8-MeV γ rays.

One of the strong points of LXe as a scintillator medium is high light yield. However the contaminant in xenon such as water and oxygen causes the deterioration of the detector performance. By introducing a purification system for liquid xenon, an absorption length longer than 100 cm at 90% C.L. has been achieved. Thanks to the purification system LXe is kept pure enough to maintain the high performance of the LXe detector at any time. Moreover we established the stable operation of the LXe cryostat and the calibration method. The stability of the LXe detector was assured by such a stable system.

In order to evaluate the performance of the LXe detector for γ rays of tens of MeV, we carried out a beam test by using LCS beam at AIST in April, 2003. For 10-MeV to 40-MeV γ rays, the energy resolution was estimated to be 3.2% to 1.5%, and the position resolution of about 9.9 mm–11 mm (FWHM) was obtained.

Based on the result from the LCS beam test, we estimated the performance for the 1000-liter LXe detector. It is expected that the energy resolution is 5.2% (FWHM) and the position resolution is the same as one for 40 MeV. The results from the various tests with the 100-liter prototype and systematic studies with MC simulation show that a 90% C.L. sensitivity in the MEG experiment reaches 1.5×10^{-13} to enable the new search for $\mu \rightarrow e\gamma$ decay.

Appendix A

10-liter prototype of Liquid Xenon Scintillation Detector

In 1998 the first prototype of LXe scintillation detector was constructed [100]. It has an active volume of 2.34 liter surrounded by 32 PMTs. Those PMTs and their holder were immersed in about 10-liter LXe as shown in Fig. A.1.

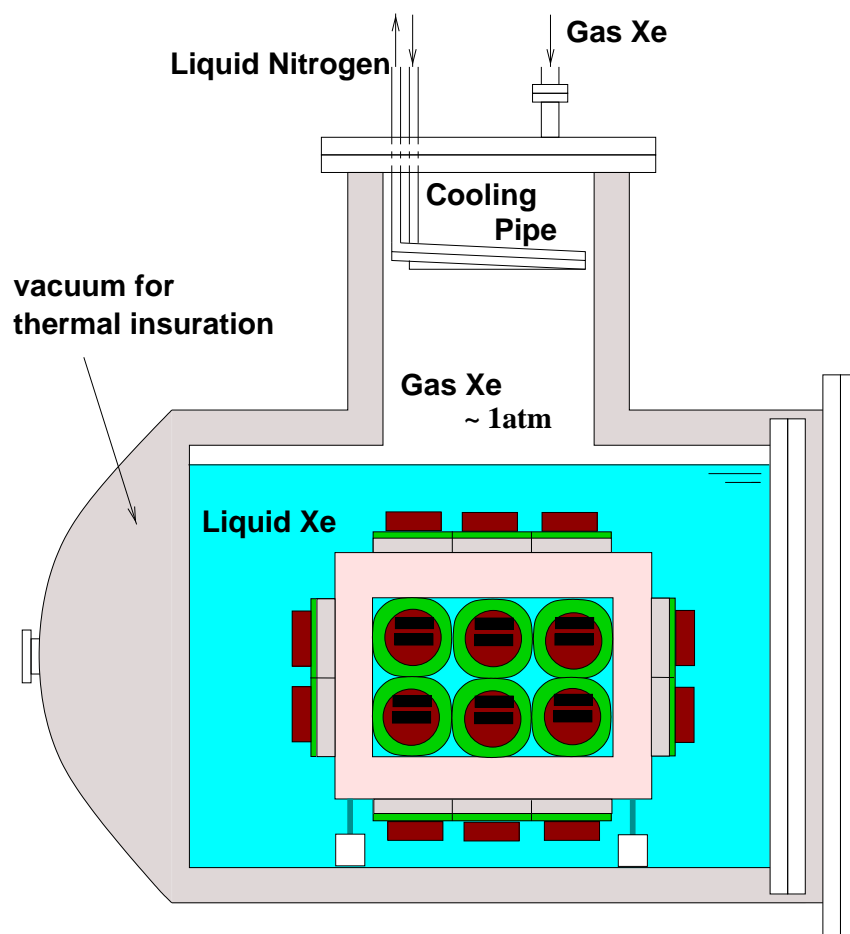


Figure A.1: Cross-sectional view of 10-liter prototype of LXe scintillation detector and its vessel.

The features of the 10-liter LXe detector were as follows:

- Photomultipliers immersed in LXe to catch LXe scintillation photons directly.
- LXe operation by using LN₂ .
- LEDs for adjusting PMT gains.
- α source (²⁴¹Am) for monitoring the stability of PMTs and adjusting relative PMT gains.
- γ -ray sources for performance evaluation.
- Less out-gassing material, such as Teflon, Aluminum, and SUS.
- Double-layer vessel for thermal isolation.

It was very first time for us to treat the LXe detector. One of the purposes was to establish the stable and secure operation of LXe. Those days it was already known well that the purity of LXe at ppb level was essential for high light yield. We payed attention to sufficient evacuation of vessels before liquefaction of xenon. It took 20 days to bake and evacuate the vessel. The refrigerator was not used, cooling pipe of LN₂ was adopted. It was controlled according to the inner pressure with an electromagnetic valve. The running time amounted to 1000 hours. No serious trouble happened over a series of the tests. Everything worked stable and well. The PMT output was stable within 0.5%. This was also an evidence of the stable operation.

The other purpose in the test with 10-liter LXe detector was to examine the response for γ rays because we had never seen any signals in LXe detectors. Tests began with low energy sources. We selected γ -ray sources from 320 keV to 1.836 MeV. The results are shown in Fig. A.3, A.2, and A.4. In the case of low energy γ rays, Compton scattering is dominant and electron shower cannot occur. Therefore it is nonsense to extrapolate these results to higher energy like 52.8 MeV straightforward. However this test was great significance in the history of R&D on the LXe detector.

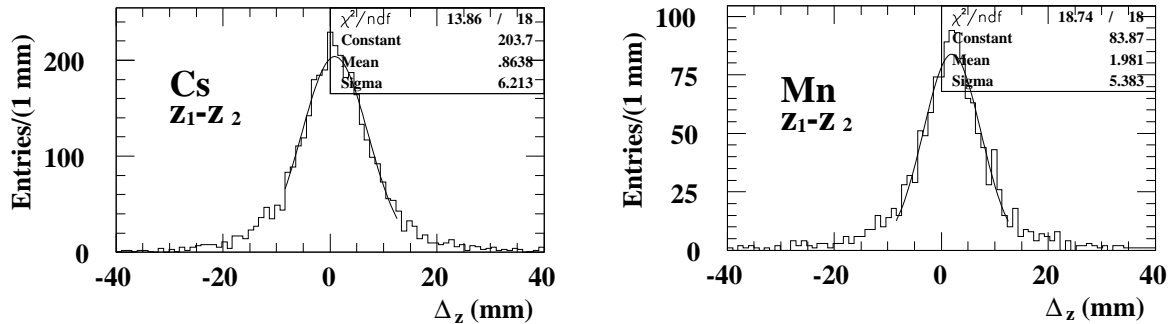


Figure A.2: The position resolution with the 10-liter prototype detector.

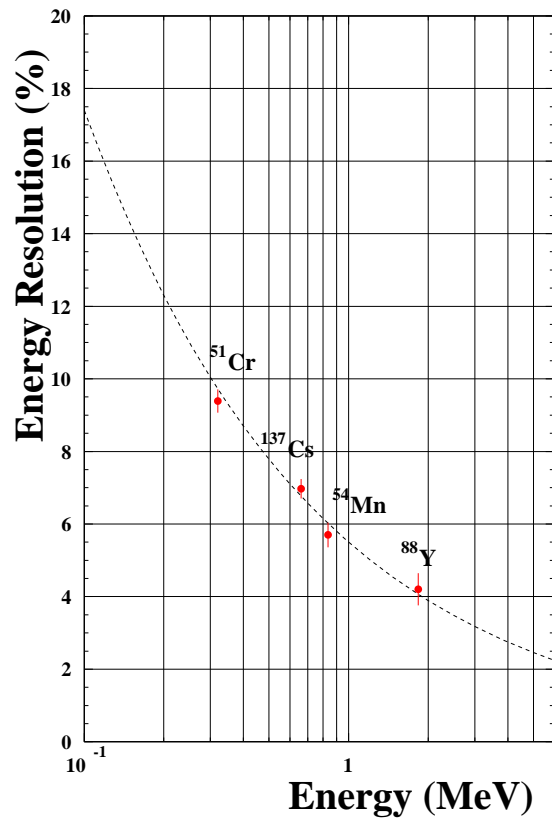


Figure A.3: The energy resolution with 10-liter prototype detector. If these results are extrapolated to 52.8 MeV, the expected energy resolution is less than 2%.

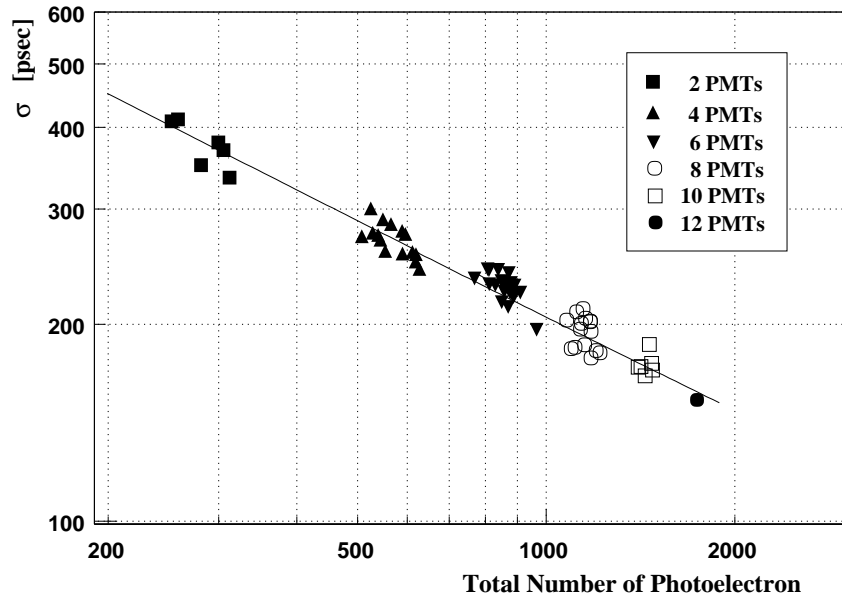


Figure A.4: The timing resolution with the 10-liter prototype detector. The resolution is expected to be about 50 psec for over 20,000 photoelectrons.

Bibliography

- [1] S. Korenchenko *et al.*, “Letter of Intent for an experiment at PSI”, R-98-05.0 (1998), available at <http://meg.web.psi.ch/docs/loi/loi.ps>
- [2] T. Mori *et al.*, “Search for $\mu \rightarrow e\gamma$ down to 10^{-14} branching ratio”, Research Proposal to PSI, May 1999.
- [3] A. Baldini *et al.*, “The MEG experiment: search for the $\mu^+ \rightarrow e^+\gamma$ decay at PSI”, Research Proposal to INFN, Sep. 2002.
- [4] G.W. Bennet *et al.*, Phys. Rev. Lett. **89** (2002), hep-ex/0208001v2 (2002).
- [5] J. Hisano and K. Tobe, Phys. Lett. **B510** (2001) 1997.
- [6] L.J. Hall and Y. Nomura, hep-ph/0205067 (2002).
- [7] L.J. Hall, V.A. Kostelechy and S. Raby, Nucl. Phys. **B267** (1986) 415.
- [8] R. Barbieri and L.J. Hall, Phys. Lett. **B338** (1994) 212;
R. Barbieri, L.J. Hall, and A. Strumia, Nucl. Phys. **B445** (1995) 219.
- [9] J. Hisano *et al.*, Phys. Lett. **B391** (1997) 341;
Erratum, Phys. Lett. **B391** (1997) 357.
- [10] The ALEPH, DELPHI, L3 and OPAL Collaborations, and the LEP Higgs Working Group, LHWG Note/2001-04, hep-ex/0107030, July 2001.
- [11] Super-Kamiokande Collaboration, Y. Fukuda *et al.*, Phys. Rev. Lett. **81** (1998) 1562;
Super-Kamiokande Collaboration, Y. Fukuda *et al.*, Phys. Lett. **B433** (1998) 9;
Super-Kamiokande Collaboration, Y. Fukuda *et al.*, Phys. Lett. **B436** (1998) 33;
Super-Kamiokande Collaboration, Y. Fukuda *et al.*, Phys. Rev. Lett. **82** (1999) 2644;
Super-Kamiokande Collaboration, S. Fukuda *et al.*, Phys. Rev. Lett. **85** (2000) 3999.
- [12] MACRO Collaboration, Phys. Lett. **B434** (1998) 451.
- [13] Soudan Collaboration, Phys. Lett. **B391** (1997) 491.
- [14] Super-Kamiokande Collaboration, Y. Fukuda *et al.*, Phys. Rev. Lett. **81** (1998) 1158;
Super-Kamiokande Collaboration, S. Fukuda *et al.*, Phys. Rev. Lett. **86** (2001) 5651;
Super-Kamiokande Collaboration, S. Fukuda *et al.*, Phys. Rev. Lett. **86** (2001) 5656.
- [15] SNO Collaboration, Q. R. Ahmad *et al.*, Phys. Rev. Lett. **87** (2001) 071301;
SNO Collaboration, Q. R. Ahmad *et al.*, Phys. Rev. Lett. **89** (2002) 011301;
SNO Collaboration, Q. R. Ahmad *et al.*, Phys. Rev. Lett. **89** (2002) 011302.

- [16] R. Davis Jr., D.S. Harmer, and K.C. Hoffman, Phys. Rev. Lett. **20** (1968) 1205; B. Cleveland *et al.*, Ap. J. **496** (1998) 505.
- [17] Gallex Collaboration, Phys. Lett. **B285** (1992) 376; Gallex Collaboration, Phys. Lett. **B357** (1995) 237; Gallex Collaboration, Phys. Lett. **B388** (1996) 384; Gallex Collaboration, Phys. Lett. **B447** (1999) 127.
- [18] SAGE Collaboration, Phys. Rev. Lett. **83** (1999) 4686.
- [19] GNO Collaboration, Phys. Lett. **B490** (2000) 16.
- [20] Kamiokande Collaboration, K.S. Hirata *et al.*, Phys. Rev. Lett. **63** (1989) 16; Kamiokande Collaboration, K.S. Hirata *et al.*, Phys. Rev. Lett. **65** (1990) 1297.
- [21] J. Hisano, T. Moroi, K. Tobe, M. Yamaguchi and T. Yanagida, Phys. Lett. **B357** (1995) 579.
- [22] J. Hisano, D. Nomura, Y. Okada, Y. Shimizu, M. Tanaka, Phys. Rev. **D58** (1998) 116010.
- [23] J. Hisano and D. Nomura, Phys. Rev. **D59** (1999) 116005 and references therein.
- [24] A. van der Schaaf *et al.*, Nucl. Phys. A **340** (1980) 249.
- [25] H.P. Povel *et al.*, Phys. Lett. B **72** (1977) 183.
- [26] P. Depommier *et al.*, Phys. Rev. Lett. **39** (1977) 1113.
- [27] W.W. Kinnison *et al.*, Phys. Rev. D **25** (1982) 2846.
- [28] J.D. Bowman *et al.*, Phys. Rev. Lett. **42** (1979) 556.
- [29] R.D. Bolton *et al.*, Phys. Rev. D **38** (1988) 2077.
- [30] M.L. Brooks *et al.*, Phys. Rev. Lett. **83**(1999) 1521.
- [31] MECO Collaboration, W. Molzon *et al.*, BNL AGS proposal **P940** (1997); the updated information are available at <http://meco.ps.uci.edu/>.
- [32] R.M. Djilkibaev and V.M. Lobashev, Sov. J. Nucl. Phys. **49**(2), (1989) 384; "MELC Experiment to Search for the $\mu^- A \rightarrow e^- A$ Process," V.S. Abadjev *et al.*, INR preprint 786/92, November 1992.
- [33] Letters of Intent for PRISM and PRIME are available at <http://www-ps.kek.jp/jhf-np/L0Ilist/L0Ilist.html>.
- [34] A. Badertscher, D. Renker and L. Simons, PSI internal report (1989); PSI Users' Guide, Accelerator Facilities.
- [35] PSI-Scientific Report 2002, 2003/Volume I.
- [36] MEG technical note TN015, June 2002. (<http://meg.psi.ch/docs/index.html>).

- [37] W. Ootani *et al.*, IEEE in Transactions on Applied Superconductivity. **14** (2004) 568-571.
- [38] A. Yamamoto *et al.*, Nucl. Phys. **B78** (1999) 565.
- [39] A. Yamamoto, Y. Makida *et al.*, IEEE Trans. Applied Superconductivity **12**, 438 (2002).
- [40] BELLE Collaboration, BELLE Progress Report, KEK Report 97-1, April 1997; BELLE Collaboration, BELLE Technical Design Report, KEK Report 95-1, April 1995.
- [41] BaBar Collaboration, Technical Design Report, March 1995.
- [42] O. Nitoh *et al.* , Jpn. J. Appl. Phys. **33** (1994) 5929.
- [43] M.I. Lopes and V.Chepel, D. Lide ed., “Handbook of Chemistry & Physics”, 76th edition (1995), Chemical Rubber.
- [44] A.C. Sinnock and B.L. Smith, Phys. Rev. **181** (1969) 1297.
- [45] F. Sauli ed., “Instrumentation in High Energy Physics”, Advanced Series on Directions in High Energy Physics Vol.9, World Scientific, 1992.
- [46] Particle Data Book.
- [47] C. W. Fabjan and F. Gianotti, “Calorimetry of particle physics”, Rev. Mod. Phys. **75** (2003) 1243
- [48] J. Jortner *et al.*, J. Chem. Phys. **42**(1965) 4250.
- [49] N. Schwenter, E.-E. Koch and J. Jortner, “Electronic Excitations in Condensed Rare Gases”, Springer-Verlag, Berlin 1985.
- [50] L. M. Barkov *et al.*, Nucl. Instr. and Meth **A379** (1996) 482.
- [51] V. N. Solovov, V. Chepel *et al.*, Nucl. Instr. and Meth. **A516** (2004) 462.
- [52] S. Nakamura: private communication.
- [53] G.M. Seidel, R.E. Lanou, W. Yao, Nucl. Instr. and Meth **A489** (2002) 189.
- [54] T. Doke *et al.*, Jpn. J. Appl. Phys. **41**(2002) 1538.
- [55] T. Doke, Portugal Phys. **12**(1981) 9.
- [56] A. Braem *et al.*, Nucl. Instr. and Meth. **A320**(1992) 228.
- [57] V. Y. Chepel *et al.*, Nucl. Instr. and Meth. **A349**(1994) 500.
- [58] N. Ishida *et al.*, Nucl. Instr. and Meth. **A384**(1997) 380.
- [59] G. M. Seidel *et al.*, Nucl. Instr. and Meth. **A489**(2002) 189.

- [60] T. Doke *et al.*, Nucl. Instr. and Meth. **A420**(1999) 62.
- [61] T. Haruyama *et al.*, KEK Preprint 2002-102, Sep 2002.
- [62] GM pulse tube refrigerator, Aisin Seiki Co., Ltd., 2-1 Kariya, Asahi, Aichi 448-8650, Japan.
- [63] ATLAS Liquid Argon Calorimeter Technical Design Report, CERN/LHCC/96-41, ATLAS TDR2, December 15, 1996;
D. Axen *et al.*, ATL-LARG-2003-007.
- [64] The tolerance against the magnetic field was measured by the Hamamatsu Photonics.
- [65] T. Haruyama *et al.*, KEK preprint 2002-102.
- [66] Data acquisition system, MIDAS, <http://midas.psi.ch/>
- [67] LabVIEW, <http://www.ni.com/>
- [68] MONO TORR PS15 Series, SAES Pure Gas, Inc. 4175 Santa Fe Road San Luis Obispo, California, 93401 USA.
- [69] Oxisorb, Messer Griesheim GmbH, Dusseldorf, Germany.
- [70] GEANT, Detector Description Simulation Tool, CERN Program Library.
- [71] K. Watanabe *et al.*, J. Opt. Soc. Am. **43** (1953) 753.
- [72] K. Watanabe *et al.*, J. Chem. Phys. **21** (1953) 1026.
- [73] V.N. Solovov, V. Chepel, M.I. Lopes and A. Hitachi, Nucl. Instr. and Meth. **A516** (2004) 462.
- [74] U. Hohm, Molecular Physics **81** (1994) 157.
- [75] A. C. Sinnock, J. Phys. C: Sol. St. Phys. **13** (1980) 2375.
- [76] A. Bideau-Mehu *et al.*, J. Quant. Spectrosc. Radiat. Transfer **25** (1981) 395.
- [77] A. Baldini *et al.*, arXiv:physics/041072v1 15 Jan 2004.
- [78] Landau, Lifshitz. Electrodynamics of continuous media, Pergamon Press.
- [79] U. Hohm, K. Kerl, Molecular Physics, **69** (1990) 803.
- [80] Y. Yoshino *et al.* "Absorption cross section measurement of water vapor in the wavelength region 120 to 188 nm" Chem. Phys. **211** (1996) 387.
Tabulated data available at
http://cfa-www.harvard.edu/amdata/ampdata/VUV_H20/
- [81] The tabulated data 'GG_02x.txt' are taken from
<http://uvisun.msfc.nasa.gov/GG/GG34-ECHAR/oldhome.html>

- [82] Prisma QMS200, Pfeiffer Vacuum Technology AG, Berliner Str. 43 35614 Asslar, Germany.
- [83] M. Miyajima *et al.*, Nucl. Instr. and Meth. **B63** (1992) 297.
- [84] F. R. Arutyunian and V. A. Tumanian, Phys. Lett. **4**(1963) 176.
- [85] LED driver C529, CAEN S.p.A., Via Vetraria 11 55049 Viareggio (LU), Italy.
- [86] Mono-Color Lamps/ ϕ 4 Series E1L49-3B1A-02, Toyoda Gosei Co., Ltd., Aichi, Japan 452-8564.
- [87] S. Tokár *et al.*, ATL-TILECAL-99-005.
- [88] E.H. Bellamy *et al.*, Nucl. Instr. and Meth. **A339** (1994) 468.
- [89] P. Hanlet *et al.*, Nucl. Instr. and Meth. **A521** (2004) 343.
- [90] E. Morikawa *et al.*, J. Chem. Phys. **91** (1989) 1469.
- [91] J. Jortner *et al.*, J. Chem. Phys. **42** (1965) 4250.
- [92] Roger H. French, Harald Müllejans, and David J. Jones, J. Am. Ceram. Soc. **81** (1998) 2549.
- [93] S. Belforte *et al.*, SVT Technical Design Report, CDF note 3108 (1994); CERN EP report 81-12/Rev.
- [94] T. Mitsuhashi, Master thesis of Univ. of Tokyo (2003), unpublished in Japanese.
- [95] Y. Kuno and Y. Okada, Phys. Rev. Lett. **77** (1996) 434.
- [96] C. Fronsdal and H. Überall, Phys. Rev. **113** (1959) 654;
S. G. Eckstein and R. H. Pratt, Ann. of Phys. **8** (1959) 297.
- [97] Y. Kuno, A. Maki, and Y. Okada, Phys. Rev. **D55** (1997) 2517.
- [98] S. Baker and R. Cousins, Nucl. Instr. and Meth. **221** (1983) 437.
- [99] N. Ishida *et al.*, Nucl. Instr. and Meth. **A518** (2004) 470.
- [100] T. Miyazawa, Master thesis of Univ. of Tokyo (1999), unpublished in Japanese.